ORNL/TM-10631

ornl

OAK RIDGE NATIONAL LABORATORY

MARTIN MARIETTA

The Oak Ridge National Laboratory Strategic Defense Initiative Shield Optimization Program

T. A. Gabriel
J. M. Barnes
B. L. Bishop
J. D. Drischler
J. O. Johnson
R. A. Lillie
R. T. Santoro
M. S. Smith

OPERATED BY
MARTIN MARIETTA ENERGY SYSTEMS, INC.
FOR THE UNITED STATES
DEPARTMENT OF ENERGY

Printed in the United States of America. Available from
National Technical Information Service
U.S. Department of Commerce
5285 Port Royal Road, Springfield, Virginia 22161
NTIS price codes—Printed Copy: A07; Microfiche A01

ORNL/TM-10631

Engineering Physics and Mathematics Division

THE OAK RIDGE NATIONAL LABORATORY STRATEGIC DEFENSE INITIATIVE SHIELD OPTIMIZATION PROGRAM

T. A. Gabriel, J. M. Barnes,* B. L. Bishop,* J. D. Drischler
J. O. Johnson, R. A. Lillie, R. T. Santoro, M. S. Smith

*Computing and Telecommunications Division

DATE PUBLISHED — April 1988

Prepared by
Oak Ridge National Laboratory
Oak Ridge, Tennessee 37831
operated by
MARTIN MARIETTA ENERGY SYSTEMS, INC.
for the
U.S. DEPARTMENT OF ENERGY
under Contract No. DE-AC05-84OR21400

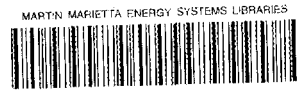

PREFACE

The research reported here was performed for the Air Force Weapons Laboratory (AFWL) in support of the Strategic Defense Initiative Survivability Program.

The natural and man-made radiation environments of space are envisioned to pose significant potential threats to space deployed SDI systems. The data reported here are the results of an initial scoping study to parameterize the radiation induced damage to silicon based electronic components carried on a satellite and to estimate the required additional shielding to reduce the damage to these components to "acceptable" limits. The calculations performed in this study were carried out using a highly idealized representation of a spacecraft, so the results obtained are to be treated as conservative, at best.

Subsequent studies will be made to more rationally isolate the significant radiation induced damage thresholds, particularly for the Van Allen belt proton radiation and nuclear weapon X-rays. These calculations will be made using three-dimensional radiation transport method using a representative weapon platform architecture. While very significant damage will occur as the result of interdiction by neutral particle beams, this type of weapon does not represent an immediate threat to SDI systems.

CONTENTS

LIST OF FIGURES

LIST OF TABLES

ABSTRACT

Scoping studies have been completed to estimate the radiation induced damage in silicon based electronic components carried on a satellite. The analyses were completed for natural (Van Allen belt protons and electrons, solar flares, and galactic cosmic rays) and man-made (nuclear and directed neutral particle beam weapons) radiation expected to be encountered by an SDI satellite or weapon platform. The Van Allen belt protons, depending on altitude and orbital inclination, were found to be the most stressing natural radiation threat. Nuclear weapon radiation, depending upon the weapon yield and distance of the detonation from the satellite, and neutral particle beam radiation were found to terminally destroy electronic components. Calculations were also made to estimate the amount of local shielding required to extend mission performance. These shields were optimized for minimum weight for specified damage thresholds. All of the calculations were carried out assuming the presence of a thin primary shield tailored specifically for survivability against an incident low mass kinetic energy weapon projectile and which affords minimal protection against energetic radiation.

1. INTRODUCTION

Electronic equipment, especially modern integrated circuits, when exposed to various radiation environments, both natural and man-made, will undergo an alteration of the electrical properties of the active components. These changes can result in degradation of circuit performance or circuit failure. Also, in a pulsed radiation environment, radiation induced photocurrents can lead to transient circuit upsets.[1]

The purpose of this paper is threefold and deals with the mitigation of the above mentioned radiation damage. The first purpose is to scope the radiation environments that a spacecraft will be subjected to such that potential levels of radiation damage can be obtained. These radiation environments include Van Allen belt protons and electrons; galactic and solar flare protons; neutrons, gamma rays, and X-rays from fission and fusion weapons; and directed hydrogen particle beams.* The damage from these radiation environments will be determined in silicon inside a lightly shielded spacecraft. The second purpose is to consider various secondary shields that can be placed around the silicon to reduce the dose the silicon receives. This "hardening" or shielding of the electronic equipment cannot possibly reduce to zero the amount of damage that can be received due to weight restrictions but will allow for extended lifetimes of the equipment. Since spacecraft designers are concerned about weight, this will be the third consideration in this paper: for a given damage reduction and shielding materials, what is the minimum weight and shielding configuration that can be devised.

Damage levels are characterized by several parameters depending on the radiation considered. The parameters which are considered in this work include total energy deposition, ionization energy deposition, and displacement energy deposition (Rads(Si) or Rads(Si)/sec); particle fluxes and fluences ($cm^{-2} \cdot sec^{-1}$ or cm^{-2}); and equivalent 1 MeV neutron fluence.

Presented in Section 2 of this report are the programs, source spectra, data bases, and geometries used in these calculations; in Section 3, the discussion of the calculated results; and in Section 4, a summary.

---

* All particle beams must be neutrally charged to prevent deflection by the magnetic field of the earth. When mentioned in this report, proton beams will be understood to mean hydrogen beams.

2. METHOD OF CALCULATION

2.1. GEOMETRY OF SPACECRAFT

The geometry of the spacecraft used in the present calculations is given in Figure 1. The entire system is spherically symmetric. The outer hull of the craft is the kinetic energy weapon (KEW) shield which was developed as part of this overall program. It is composed of a thin Al outer layer (thickness = 0.16 cm) surrounding porous carbon (thickness = 10.16 cm, ρ = 0.10 gm/cm^3) and a stainless steel 316 (thickness = 0.23 cm) inner liner. The inner radius of the spacecraft out to the stainless steel liner is 1.00m. Located at the center of the spacecraft is a silicon sphere of radius 2.0 cm. External to the silicon is the radiation shield. In some of the calculations, this shielding material is lead followed by lithium hydride or borated polyethylene. In other calculations, the secondary shielding material is composed of either borated polyethylene, aluminum, iron, lead, or void. The composition of all of the materials used in the calculations are summarized in Table 1. For these scoping studies no material is located between the silicon and/or radiation shielding materials and the inner stainless steel liner.

2.2. CODES

2.2.1. CALOR

CALOR[2] is a combination of code systems allowing for a complete treatment of hadronic and electromagnetic collisions and particle transport.

The calculations performed with the CALOR code system follow approximately the procedures used in previous calculations.[3,4] A flow diagram of the codes in CALOR is given in Figure 2. The three-dimensional, multimedia, High-Energy nucleon-meson Transport Code HETC[5] was used to obtain a detailed description of the nucleon-meson cascade produced in the spacecraft by various radiation fields considered in this report. HETC is an analog code and operates with combinational geometry so very detailed geometries can be modeled. This Monte Carlo code takes into account the slowing down of charged particles via the continuous slowing-down approximation, the decay of charged pions and muons, inelastic nucleon-nucleus and charged-pion-nucleus (excluding hydrogen) collisions through the use of the intermediate-energy intranuclear-cascade-evaporation (MECC) model (E < 3 GeV)

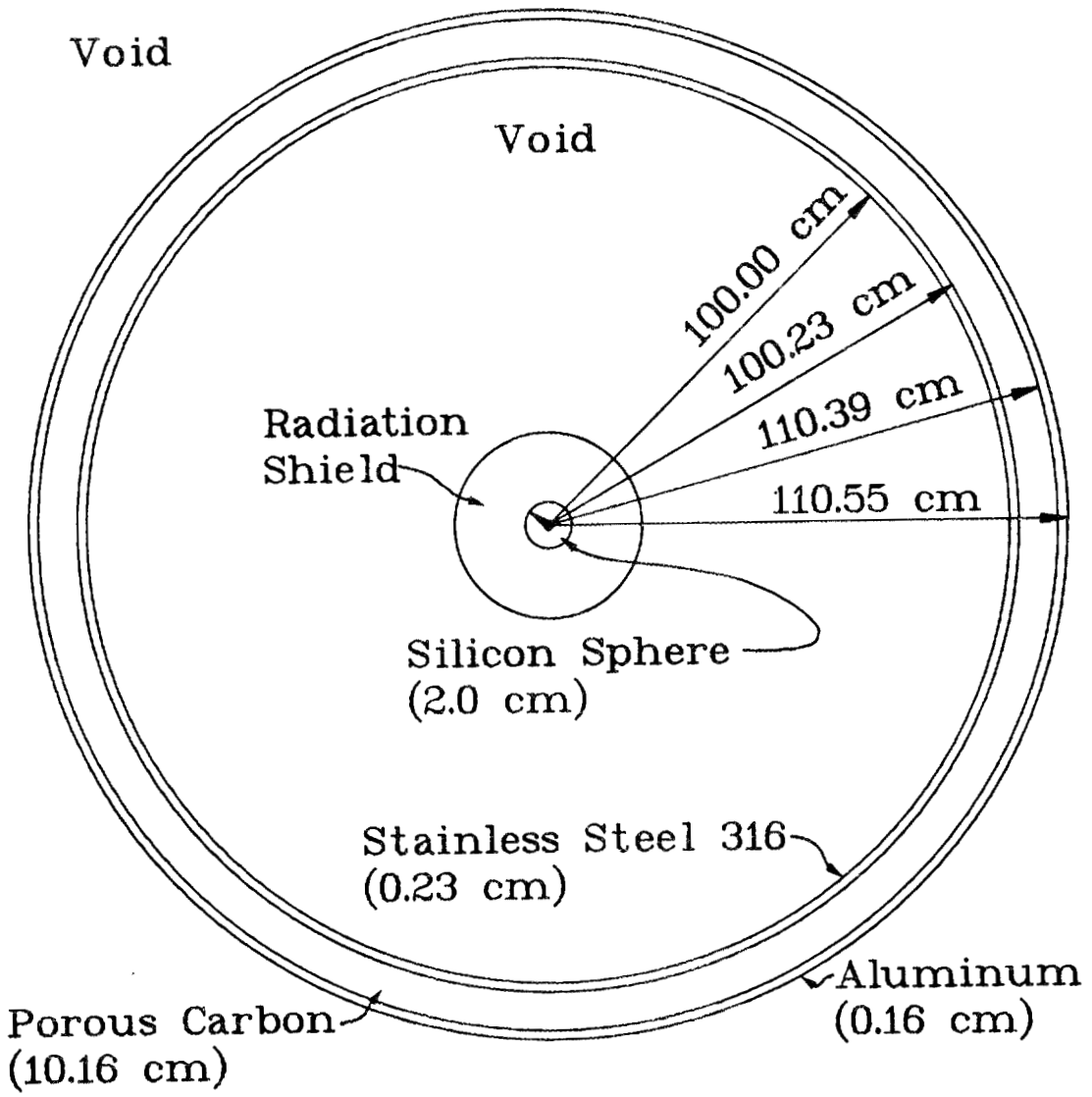

Figure 1. The spacecraft model used in the calculations (see text concerning the composition of the radiation shield).

Table 1

Materials Used in the Transport Calculations

Material	Density(g/cm^3)	Weight%	Atomic Weight	Atom Density $(barn\text{-}cm)^{-1}$
Silicon	2.35	100% Si	28.09	5.039-2[a]
Aluminum	2.70	100% Al	26.98	6.028-2
Porous Carbon	0.10	100% C	12.00	5.019-3
Stainless Steel 316	7.95	17.0% Cr	52.00	1.566-2
		1.7% Mn	54.94	1.482-3
		2.5% Mo	95.94	1.248-3
		12.0% Ni	58.70	9.789-3
		1.0% Si	28.09	1.705-3
		65.8% Fe	55.85	5.641-2
Iron	7.86	100% Fe	55.85	8.476-2
Lead	11.35	100% Pb	207.2	3.299-2
Lithium Hydride	0.80	87.3% Li	6.94	6.060-2
		12.7% H	1.01	6.060-2
Borated Polyethylene	1.00	10.0% B	10.81	5.580-3
		12.4% H	1.01	7.505-2
		77.6% C	12.01	3.885-2

[a]Read as 5.039×10^{-2}.

and scaling model (E > 3 GeV), and inelastic nucleon-hydrogen and charged-pion-hydrogen collisions via the isobar model (E < 3 GeV) and phenomenological fits to experimental data (E > 3 GeV). Also accounted for are elastic neutron-nucleus collisions (E < 100 MeV), and elastic nucleon and charged-pion collisions with hydrogen.

The intranuclear-cascade-evaporation model as implemented by Bertini is the heart of the HETC code.[6] This model has been used for a variety of calculations and has been shown to agree quite well with many experimental results. Even when agreement is poor, the results produced by this model can lead the user to make generally correct design decisions. The underlying assumption of this model is that particle-nucleus interaction can be treated as a series of two-body collisions within the nucleus and that the location of these collisions and resulting particles from the collisions are governed by experimental and/or theoretical particle-particle total and differential cross-section data. The types of particle collisions included in the calculations are elastic, inelastic, and charge exchange. This model incorporates the diffuseness of the nuclear edge, the Fermi motion of the bound nucleons, the exclusion principle, and a local potential for nucleons and pions. The density of the neutrons and protons within the nucleus (which is used with the total particle-particle cross section to determine interaction locations) are determined from the experimental data of Hofstadter.[6] Nuclear potentials are determined from these density profiles by using a zero-temperature Fermi distribution. The total well depth is then defined as the Fermi energy plus 7 MeV. Following the cascade part of the interaction, there is excitation energy left in the nucleus. This energy is treated by using an evaporation model which allows for the emission of protons, neutrons, deuterons, tritons, helium-3, and alphas. Fission induced by high-energy particles is accounted for during this phase of the calculation by allowing it to compete with evaporation. Whether or not a detailed fission model is included has very little effect on the total number of secondary neutrons produced.

For some calculations, HETC was modified so that only unattenuated primary protons are considered. For minimal shielding only, the primary protons will dominate the silicon damage. However, as the shielding increases, secondary particles produced in proton-nucleus collisions will become more important and the full transport and collision capability of CALOR must be used.

The source distribution for the electromagnetic cascade calculation is provided by HETC, and consists of photons from neutral pion decay, electrons and positrons from muon decay, de-excitation gamma rays from inelastic nuclear collisions, and fission gamma rays. Since the discrete decay energies of the de-excitation gammas are not provided by HETC and only the total energy is known, individual gamma energies are obtained by uniformly sampling from the available energy until it is completely depleted. The transport of the electrons, positrons, and gammas from the reactions described above and Van Allen belt electrons, X-rays, etc., are carried out using the EGS system.[7]

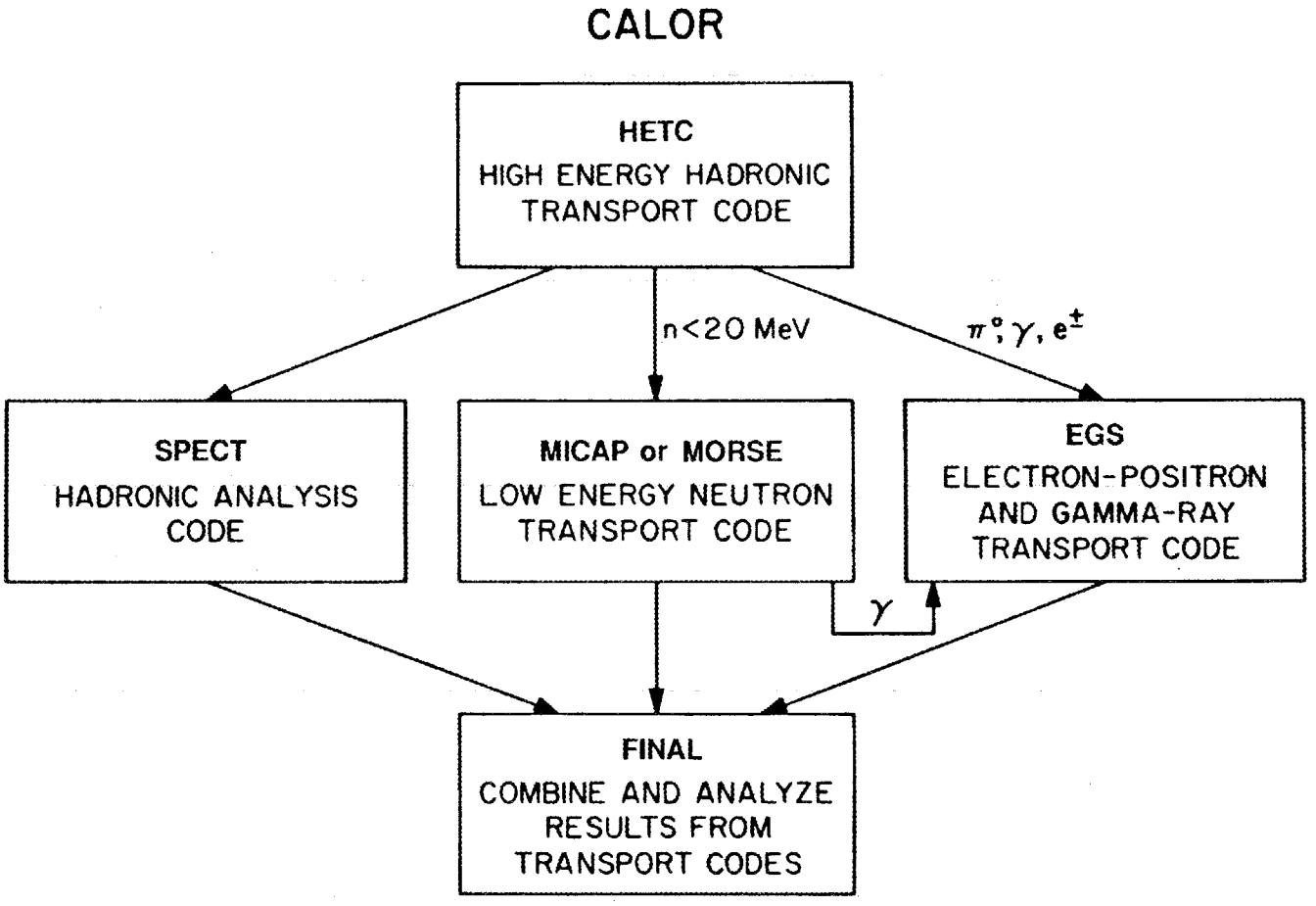

Figure 2. Flow diagram of the CALOR computer system.

As with HETC, EGS is a three-dimensional multimedia transport code that can operate with the combinatorial geometry package. EGS is an analog Monte Carlo code and takes into account all important physical processes including the photoelectric effect, positron annihilation, bremsstrahlung, pair production, compton scattering, and energy loss and directional changes associated with electron and positron ionization excitation collisions with other electrons and nuclei. The program PEGS[7] is used to generate the necessary total and differential cross-section data.

The EGS/PEGS code that is currently in use at ORNL is version 3. This version is being replaced by version 4. Some sample problems have been calculated using the new version. However, the modifications that were incorporated into version 3 (combinatorial geometry, coupling to the HETC code, coupling to the MORSE code, etc.) have now been completed. Even though the new code version is not expected to change the calculated results drastically as indicated by several initial calculations, there are new features associated with this code which will be advantageous for future calculations, for example, path length stretching, leading particle biasing, etc.

Neutrons which are produced by hadron/nucleus collisions with energies below 20 MeV during the HETC transport calculations are transported using the MORSE Monte Carlo transport code with combinatorial geometry.[8] The neutron and gamma ray cross sections, both total and differential and gamma ray production, used by MORSE were obtained from ENDF/B-V.[9] Gamma rays (including those from capture, fission, etc.) produced during this phase of the calculations can be transported by MORSE or are stored for transport by the EGS code. The MORSE code was developed for reactor application and can treat nonfissioning and fissioning systems in detail.

In contrast to HETC and EGS, MORSE is not an analog code. Particle weighting, splitting, etc., is used throughout the transport. When a collision occurs, detailed information concerning the recoil nucleus, type of nucleus struck, etc., is not available. In some applications, these details are needed and just recently, a code, MICAP,[10] has become available and has been used for some of the calculations.

MICAP is a multimedia three-dimensional point cross section, analog Monte Carlo transport code with combinatorial geometry. The code treats low energy neutron and ion transport. Cross sections, as with MORSE, are obtained from ENDF/B-V. When a neutron collision occurs, MICAP determines the type of nucleus and the particular type of reaction $(n,n\prime),(n,2n)$, etc). The energy of the secondary products are determined whenever possible from ENDF/B-V data. If this information is not available, evaporation models and energy and momentum conservation are used to determine the required information. MICAP can be easily used to determine the effect of various damage models since the primary knock-on atom (PKA) spectra can be determined directly from MICAP. Gamma rays produced during neutron/nucleus collisions are transported in EGS. The energy

distribution and multiplicity of these gamma rays are obtained from ENDF/B-V data.

2.2.2. ANISN and ASOP

ANISN[11] solves the one-dimensional multimedia Boltzmann transport equation for neutrons or gamma rays in slab, sphere, or cylindrical geometry using the discrete ordinates method. The source may be fixed, fission, or a subcritical combination of the two. Criticality search may be performed on any one of several parameters.

ANISN was designed to solve deep-penetration problems in which angle-dependent spectra are calculated in detail. ANISN also includes a technique for handling general anisotropic scattering, pointwise convergence criteria, and alternate step function difference equations that effectively remove the oscillating flux distributions sometimes found in discrete ordinates solutions.

The computer code, ASOP,[12] has been used to determine the optimum relative thickness of a multilayered radiation shield for the sensitive silicon in the spacecraft. ASOP is a one-dimensional shield optimization program based on the one-dimensional discrete ordinates code ANISN. ASOP was written to design a shield with a minimum weight for a given dose constraint.

Fortunately, a plane wave source (indicative of a distant weapon detonation) incident on a spherical spacecraft is equivalent to an isotropic flux condition on the surface of the spacecraft. This allows for plane wave optimization of the shield using the isotropic flux boundary condition in the ASOP calculations.

2.3. CROSS SECTION LIBRARIES AND RESPONSE FUNCTIONS

DLC31[13] is a cross-section library that was developed for the Defense Nuclear Agency. A list of the 35 nuclides ranging from H to Pu are included in this cross-section library.

The cross sections were processed into a coupled 37-21 neutron-gamma energy group structure, with gamma-ray production included for each element. The energy structure, shown in Table 2, is quite biased at high energies for both the neutron and the gamma-ray groups owing to the importance of high-energy particles for the calculation of radiation damage in electronics. In addition, the neutron energy groups are tailored to allow for the major peaks and valleys in the total neutron cross sections of nitrogen, oxygen, silicon, and iron, and the gamma-ray groups are tailored to allow accurate calculation of pair production, annihilation photon transport, hydrogen capture, and backscatter photon transport. There is also sufficient low photon energy structure to allow for rapidly changing cross sections and response functions. These cross-section data were processed with the AMPX[9]

Table 2

Neutron and Gamma-Ray Energy Boundaries
for the 37-21 Coupled Neutron-Gamma Library

	Neutron Group (eV)		Gamma Group (eV)	
Group No.	Energy	Lethargy	Energy	Eff. Avg.
1	1.96+7*	-0.675	1.40+7	1.20+7
2	1.69+7	-0.525	1.00+7	9.00+6
3	1.49+7	-0.400	8.00+6	7.50+6
4	1.42+7	-0.350	7.00+6	6.50+6
5	1.38+7	-0.325	6.00+6	5.50+6
6	1.28+7	-0.250	5.00+6	4.50+6
7	1.22+7	-0.200	4.00+6	3.50+6
8	1.11+7	-0.100	3.00+6	2.75+6
9	1.00+7	0.000	2.50+6	2.25+6
10	9.05+6	0.100	2.00+6	1.75+6
11	8.19+6	0.200	1.50+6	1.25+6
12	7.41+6	0.300	1.00+6	8.50+5
13	6.38+6	0.450	7.00+5	5.75+5
14	4.97+6	0.700	4.50+5	3.75+5
15	4.72+6	0.750	3.00+5	2.25+5
16	4.07+6	0.900	1.50+5	1.25+5
17	3.01+6	1.200	1.00+5	8.50+4
18	2.39+6	1.433	7.00+4	5.75+4
19	2.31+6	1.467	4.50+4	3.75+4
20	1.83+6	1.700	3.00+4	2.50+4
21	1.11+6	2.200	2.00+4	1.50+4
22	5.50+5	2.900	1.00+4	
23	1.58+5	4.150		
24	1.11+5	4.500		
25	5.25+4	5.250		
26	2.48+4	6.000		
27	2.19+4	6.125		
28	1.03+4	6.875		
29	3.35+3	8.000		
30	1.23+3	9.000		
31	5.83+2	9.750		
32	1.01+2	11.500		
33	2.90+1	12.750		
34	1.07+1	13.750		
35	3.06+0	15.000		
36	1.13+0	16.000		
37	4.14−1	17.000		
	1.00−5	27.631		

*Read as 1.96×10^7.

code, using a 1/E weighting spectrum for all neutron groups except the thermal group, for which a 300°K Maxwellian weighting spectrum was used.

During the course of this work, two new cross-section libraries[14] have become available. These libraries were collapsed from the VITAMIN-E data base[15] using the VITAMIN-E weighting function for the neutron groups and "1/E" for the photon groups. The group boundaries of one of the libraries is the same as the DLC31 library. The other library has 46 neutron and 23 gamma groups. To look for deviation in the DLC31 cross-section set, some calculations were carried out using the new (36n, 21γ) library. The new libraries do not currently have updated response functions. Therefore, the response functions from the DLC31 library were utilized for these updated calculations. Plans are currently underway to convert to the new (46n, 23γ) library as soon as updated damage response functions become available.

Radiation effects can result from ionization and from nuclear displacements.[16,17,18] The total dose deposited in a material can be written as

$$D_{\text{total}} = D_{\text{ionization}} + D_{\text{displacements}}.$$

The ionization problem that occurs is due to the radiation-induced charging of the thin oxide regions (nonconducting regions), which generates additional space-charge fields at the silicon surface. These additional induced fields result in voltage offsets or shifts in turn-on voltages of the devices, which lead to circuit degradation or device failure. These radiation-induced chargings are also responsible for single event upsets and circuit lockup. This damage generally can be of a short term nature and depends strongly on the rate at which the ionization dose is applied.

Any particle with sufficient energy can cause lattice displacement damage. Neutrons and charged particles (electrons, protons, alpha particles, heavy cosmic ray ions) are the primary contributors to displacement damage. Since neutrons do not interact directly with the electrons in the target material, they lose energy only through nuclear interactions. For this reason, displacement processes are much more important for neutrons than for charged particles. For the charged particles, ionization energy loss produces most of the energy loss, but coulomb scattering from the nucleus can lead to displacement energy loss also. Neutrons can produce many primary knock-on atoms which in turn can produce additional displacements.

The energy loss associated with nuclear processes; i.e., displacements, can be calculated using the Lindhard, Schoff, and Schiott (LSS) theory.[19] Since modern electronic devices rely heavily on pure crystalline structure in silicon for current flow, displacements produce increased resistance, and other property changes of the material which can result in a fast or slow degradation of performance.

The neutron and gamma ray response functions which determine ionization, displacement, and total dose levels in silicon are presented in Tables 3, 4, and 5. These data are taken from references 13, 16, and 17. The data as originally given by Rogers et al. and Gabriel et al., are in 22 and 105 neutron group structures,

Table 3

Neutron Ionization and Displacement Kermas for Silicon
from V. C. Rogers, et al, T. A. Gabriel, and DLC31
Rads(Si)/(neutron/cm^2)

	Ionization		Displacement		
Energy Range (eV)	Rogers[a]	DLC31	Rogers[a]	Gabriel[a]	DLC31
1.96+7[b] - 1.69+7	1.500−09	9.195−10	5.400−11	6.265−11	7.135−11
1.69+7 - 1.49+7	1.476−09	9.195−10	5.391−11	6.216−11	7.135−11
1.49+7 - 1.42+7	1.030−09	9.195−10	5.220−11	6.134−11	7.135−11
1.42+7 - 1.38+7	1.030−09	9.195−10	5.220−11	6.134−11	7.129−11
1.38+7 - 1.28+7	1.030−09	9.195−10	5.220−11	6.110−11	7.029−11
1.28+7 - 1.22+7	1.030−09	1.011−09	5.220−11	6.099−11	6.898−11
1.22+7 - 1.11+7	9.400−10	1.079−09	4.950−11	5.927−11	6.741−11
1.11+7 - 1.00+7	9.400−10	1.149−09	4.950−11	5.685−11	6.541−11
1.00+7 - 9.05+6	7.370−10	1.159−09	4.600−11	5.548−11	6.344−11
9.05+6 - 8.19+6	7.370−10	1.120−09	4.600−11	5.548−11	6.156−11
8.19+6 - 7.41+6	4.299−10	1.033−09	4.333−11	5.610−11	5.839−11
7.41+6 - 6.38+6	4.260−10	7.686−10	4.330−11	5.200−11	5.197−11
6.38+6 - 4.97+6	1.647−10	3.028−10	4.660−11	5.127−11	4.875−11
4.97+6 - 4.72+6	1.066−10	1.021−10	4.418−11	5.421−11	5.868−11
4.72+6 - 4.07+6	1.010−10	8.518−11	4.390−11	4.985−11	4.778−11
4.07+6 - 3.01+6	6.550−11	6.050−11	3.281−11	4.056−11	3.802−11
3.01+6 - 2.39+6	7.425−11	5.227−11	4.303−11	4.204−11	4.213−11
2.39+6 - 2.31+6	6.455−11	4.781−11	4.115−11	3.641−11	4.275−11
2.31+6 - 1.83+6	6.157−11	4.195−11	4.061−11	4.212−11	3.930−11
1.83+6 - 1.11+6	3.279−11	2.937−11	2.360−11	3.215−11	2.743−11
1.11+6 - 5.50+5	2.490−11	1.946−11	2.330−11	2.840−11	2.840−11
5.50+5 - 1.58+5	1.380−11	1.277−11	1.570−11	1.981−11	2.030−11
1.58+5 - 1.11+5	1.354−11	5.518−13	1.541−11	1.379−12	2.004−12
1.11+5 - 5.24+4	7.180−13	8.886−13	1.250−12	1.999−12	2.525−12
5.24+4 - 2.48+4	7.180−13	4.219−13	1.250−12	9.628−13	2.170−12
2.48+4 - 2.19+4	7.180−13	2.800−13	1.250−12	5.903−13	2.141−12
2.19+4 - 1.03+4	7.180−13	1.980−13	1.250−12	4.760−13	2.141−12
1.03+4 - 3.35+3	7.180−13	4.103−15	1.250−12	2.598−13	2.141−12
3.35+3 - 1.23+3	3.860−14	0.0	1.016−13	9.434−14	2.141−12
1.23+3 - 5.83+2	2.271−14	0.0	7.461−14	3.619−14	2.141−12
5.83+2 - 1.01+2	3.345−15	0.0	1.428−14	1.045−14	2.141−12
1.01+2 - 2.90+1	9.720−16	0.0	3.890−15	1.233−15	2.141−12
2.90+1 - 1.07+1	1.020−15	0.0	2.890−15	1.703−15	2.141−12
1.07+1 - 3.06+0	1.549−15	0.0	3.737−15	3.667−15	2.141−12
3.06+0 - 1.13+0	2.764−15	0.0	6.299−15	6.562−15	2.141−12
1.13+0 - 4.14−1	4.593−15	0.0	1.040−14	1.082−14	2.141−12
4.14−1 - 1.00−5	1.200−14	0.0	2.699−14	4.446−14	2.141−12

[a]Revised group structure.
[b]Read as $1.96 \times 10^{+7}$.

Table 4

Total Neutron Kermas for Silicon
Rads(Si)/(neutron/cm^2)

Energy Range (eV)	Rogers[a]	DLC31
1.96+7−1.69+7[b]	1.554−09	1.911−09
1.69+7−1.49+7	1.530−09	1.780−09
1.49+7−1.42+7	1.082−09	1.682−09
1.42+7−1.38+7	1.082−09	1.623−09
1.38+7−1.28+7	1.082−09	1.514−09
1.28+7−1.22+7	1.082−09	1.386−09
1.22+7−1.11+7	9.895−10	1.237−09
1.11+7−1.00+7	9.895−10	1.053−09
1.00+7−9.05+6	1.197−09	8.790−10
9.05+6−8.19+6	1.197−09	7.965−10
8.19+6−7.41+6	4.732−10	7.815−10
7.41+6−6.38+6	4.693−10	4.709−10
6.38+6−4.97+6	2.113−10	2.139−10
4.97+6−4.72+6	1.508−10	1.827−10
4.72+6−4.07+6	1.449−10	1.419−10
4.07+6−3.01+6	9.831−11	1.058−10
3.01+6−2.39+6	1.173−10	1.001−10
2.39+6−2.31+6	1.057−10	8.301−11
2.31+6−1.83+6	1.022−10	9.481−11
1.83+6−1.11+6	5.639−11	6.534−11
1.11+6−5.50+5	4.820−11	4.980−11
5.50+5−1.58+5	2.950−11	3.152−11
1.58+5−1.11+5	2.895−11	1.790−12
1.11+5−5.24+4	1.968−12	2.803−12
5.24+4−2.48+4	1.968−12	1.233−12
2.48+4−2.19+4	1.968−12	7.909−13
2.19+4−1.03+4	1.968−12	5.893−13
1.03+4−3.35+3	1.968−12	2.981−13
3.35+3−1.23+3	1.402−13	1.050−13
1.23+3−5.83+2	9.732−14	4.330−14
5.83+2−1.01+2	1.763−14	1.442−14
1.01+2−2.90+1	4.862−15	4.591−15
2.90+1−1.07+1	3.910−15	3.937−15
1.07+1−3.06+0	5.286−15	5.683−15
3.06+0−1.13+0	9.063−15	9.403−15
1.13+0−4.14+1	1.499−14	1.539−14
4.14−1−1.00−5	3.899−14	6.322−14

[a]Revised group structure.
[b]Read as 1.69×10^7

Table 5

Total and Ionization Gamma Kermas for Silicon

Energy Range (MeV)	Total[a] Rads(Si)/(neutron/cm^2)	Ionization[a] Rads(Si)/(neutron/cm^2)
14.0 −10.0	3.627−09[b]	3.849−09
10.0 − 8.0	2.687−09	2.944−09
8.0 − 7.0	2.231−09	2.485−09
7.0 − 6.0	1.950−09	2.175−09
6.0 − 5.0	1.686−09	1.862−09
5.0 − 4.0	1.423−09	1.545−09
4.0 − 3.0	1.159−09	1.222−09
3.0 − 2.5	9.615−10	9.803−09
2.5 − 2.0	8.281−10	8.284−09
2.0 − 1.5	6.885−10	6.718−10
1.5 − 1.0	5.341−10	5.074−10
1.0 − 0.7	3.900−10	3.681−10
0.7 − 0.45	2.734−10	2.657−10
0.45 − 0.30	1.788−10	1.841−10
0.30 − 0.15	1.059−10	1.120−10
0.15 − 0.10	6.995−11	7.454−10
0.10 − 0.07	7.866−11	8.359−10
0.07 − 0.045	1.395−10	1.447−10
0.045− 0.030	3.476−10	3.211−10
0.030− 0.020	8.288−10	7.388−10
0.020− 0.010	2.652−09	2.260−09

[a]The total and ionization Kermas for Gamma-rays should be approximately the same. DLC31 gives slightly different values for these.
[b]Read as 3.627×10^{-9}.

respectively. By using flat energy weighting, the original group structures were expanded or compressed into the 37 neutron group structure given in Table 2. The DLC31 displacement data in Table 3 was normalized to 1 MeV equivalent neutrons, but has been renormalized to the Gabriel data such that the two data sets agree in the 0.55 to 1.11 MeV energy group. There are some striking differences between the data sets, so some calculations were carried out using all response functions to determine their relative integral differences. The DLC31 data for ionization and displacement in Table 3 does not sum to the total in Table 4 because the data in Table 3 are from different evaluations. A plotted comparison of some of these data are given in Figures 3, 4, 5, and 6.

The displacement per atom (DPA) cross sections which are related to the displacement part of the energy deposition functions for electrons, positrons, and X-rays have been obtained from references 20 and 21. Due to the small contributions from positrons and due to the similarity in the positron and electron cross sections, positron cross sections were assumed to be equal to the electron cross sections. Gamma rays produce atom displacements via the production of electrons (Compton scattering and pair production) and positrons (pair production). Therefore, the calculated DPAs from gamma rays should equal the calculated DPAs from electrons and positrons in these calculations. The cross sections used are given in Table 6.

The proton displacement cross sections are given in Figure 7.[22] Conversion of these DPA cross sections and the others back to displacement dose levels can be done approximately by multiplying by $2E_d$ where E_d is the effective displacement threshold.

Device failure or degradation is generally given in terms of total silicon dose, rads(Si); neutron fluence or fast neutron fluence ($E_{\text{neutron}} \geq 0.1$ MeV); equivalent 1 MeV neutrons, i.e. $\int_0^T \int_{E_{\text{low}}}^{E_{\max}} \phi(E,t)D(E)dEdt / \int_0^T \int_{E_{\text{low}}}^{E_{\max}} \phi(E,t)dEdt$, where $\phi(E,t)$ is the time dependent flux and $D(E)$ is a response function, for example, the displacement neutron kerma; etc. Generally, as shown in Figure 8, it is given in terms of rad dose or fluence.[22] Also, as can be seen in this figure, different devices respond differently to various levels of radiation. For design purposes, damage levels lower than failure levels must be considered.

2.4. RADIATION SOURCES

2.4.1. Nuclear Detonations and Directed Neutral Particle Beams

Neutron and gamma ray source spectra from modern nuclear weapons are generally classified. To obtain realistic spectra, a literature search was initiated and several unclassified neutron and gamma-ray source spectra were obtained. These data are presented in Figures 9-12, (references 23, 24, 25, and 26). It is quite apparent from these data that a variety of neutron and gamma-ray spectra are possible. Due to this variety, it was decided for a preliminary scoping study

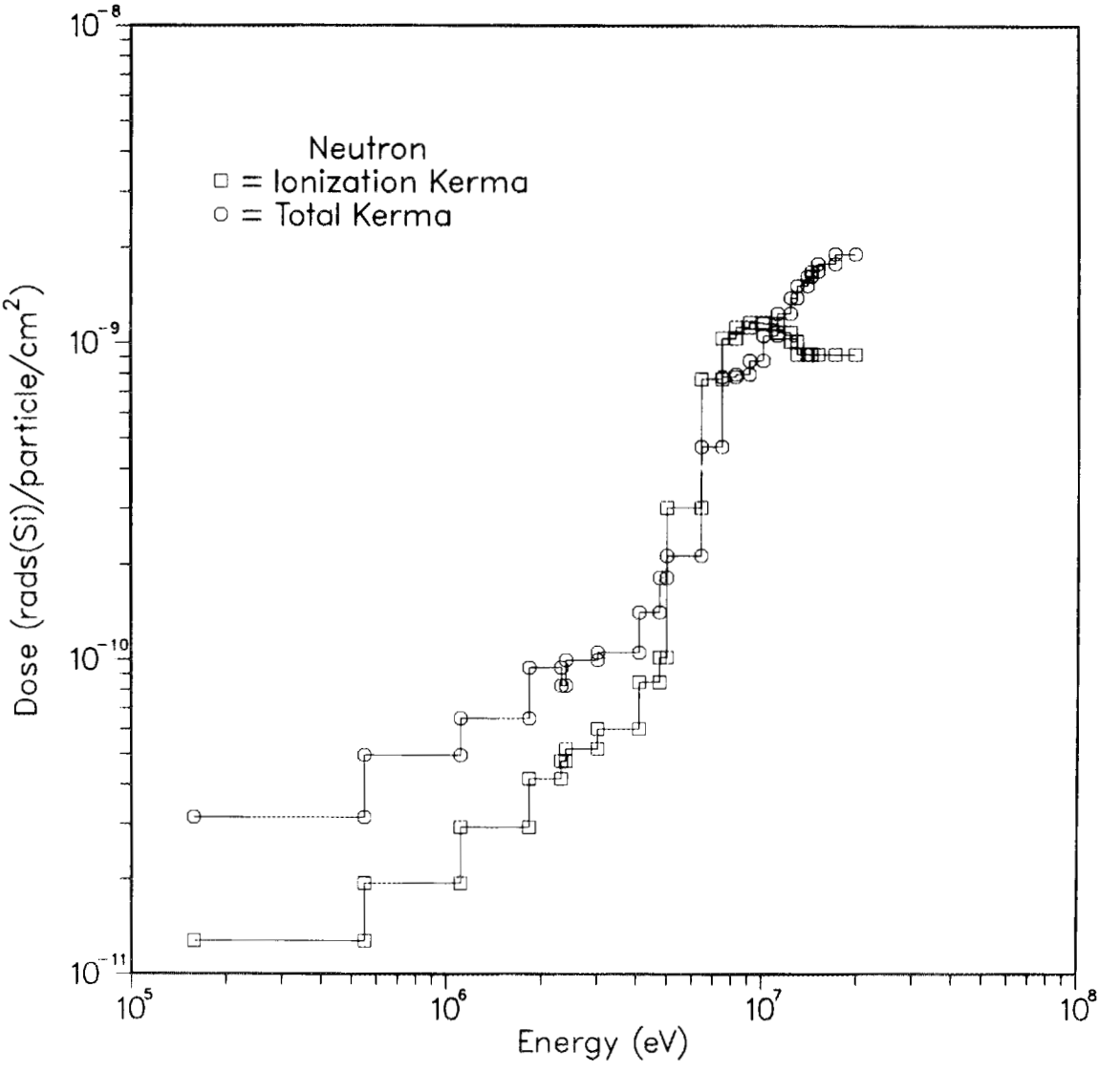

Figure 3. Response functions from DLC31 for neutron ionization and total kerma in silicon.

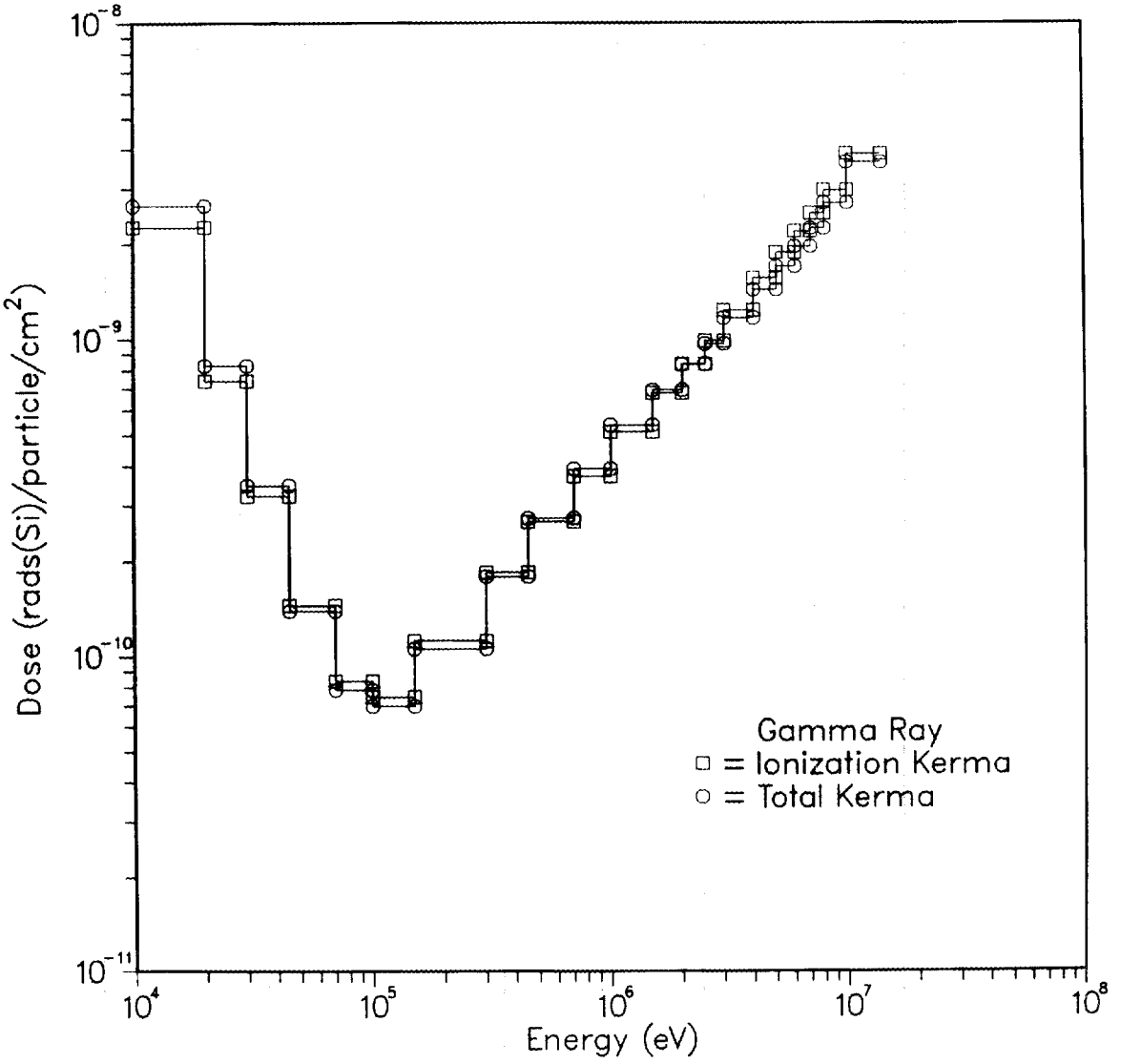

Figure 4. Response functions from DLC31 for gamma ray ionization and total kerma in silicon.

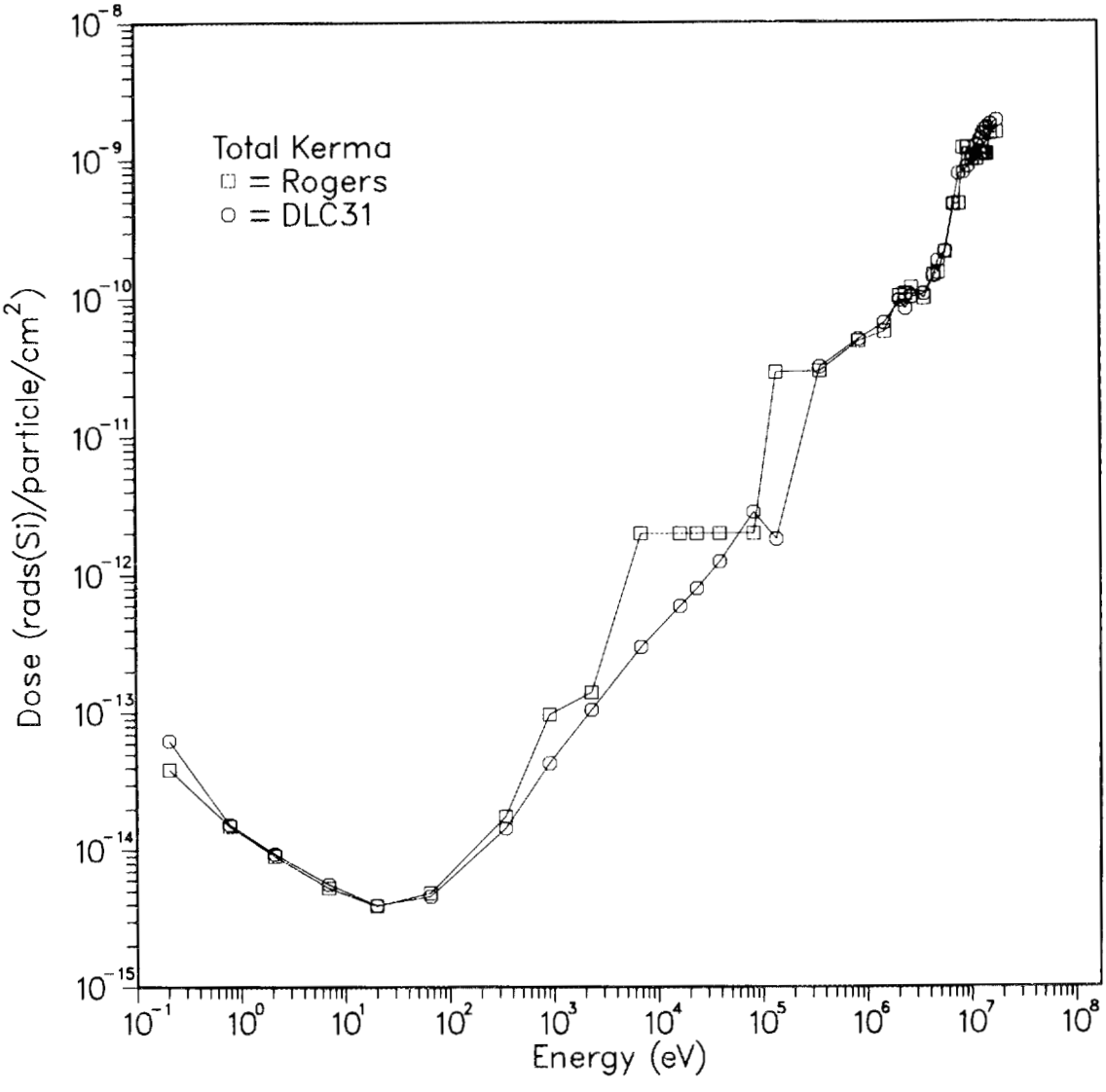

Figure 5. A comparison of neutron total kermas: DLC31 and Rogers, et al.

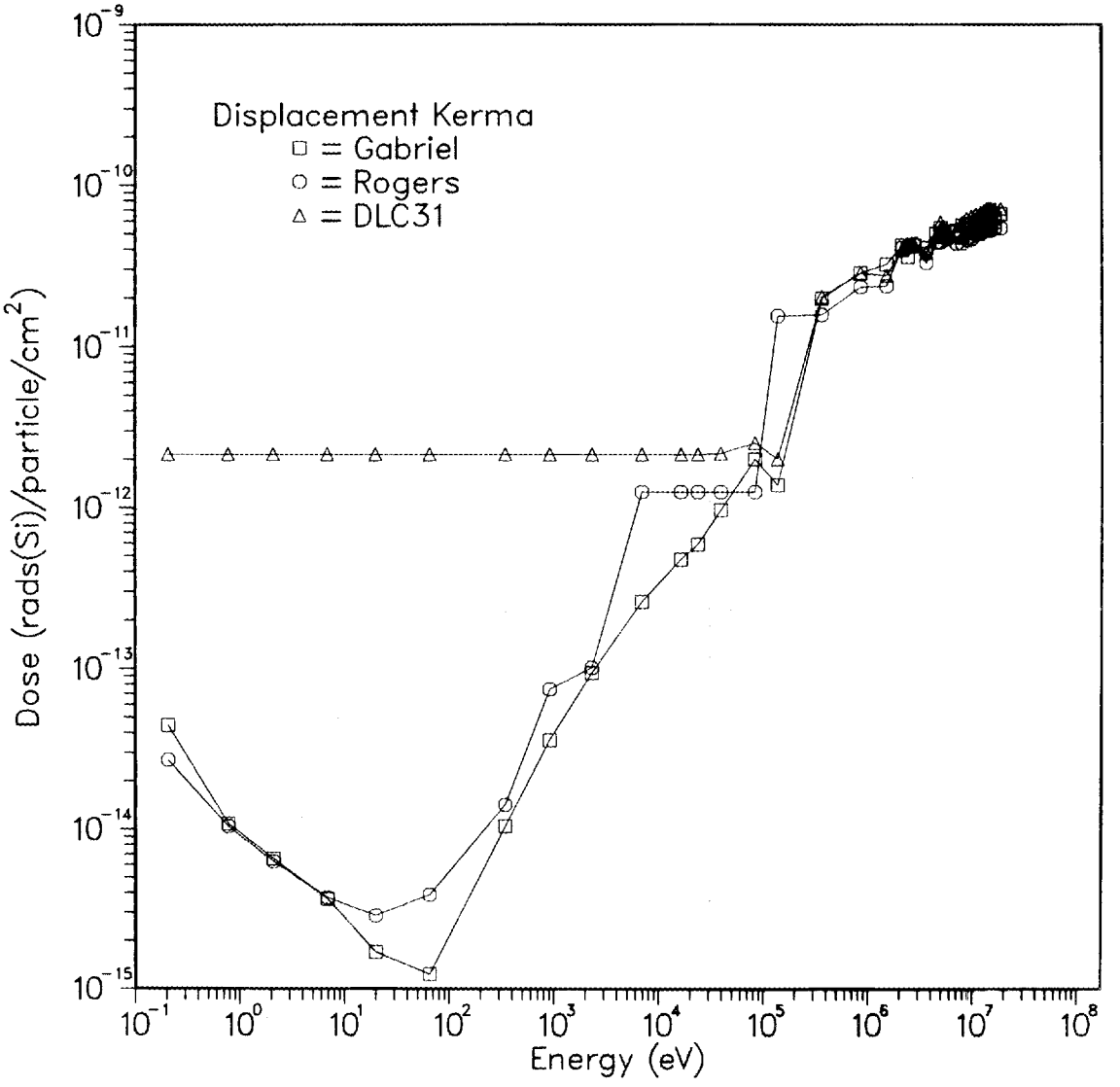

Figure 6. A comparison of neutron displacement kermas: DLC31, Rogers et al., and Gabriel et al.

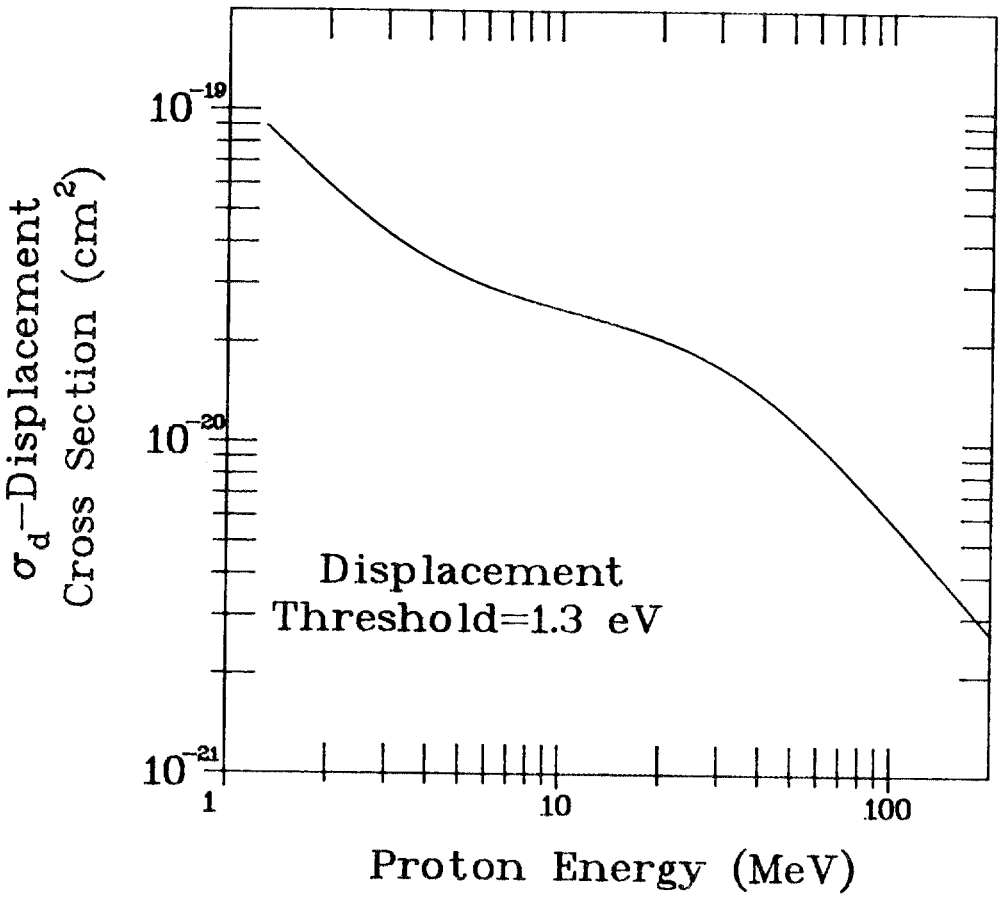

Figure 7. Displacement cross sections for silicon (including primary and secondary displacements) versus proton energy.

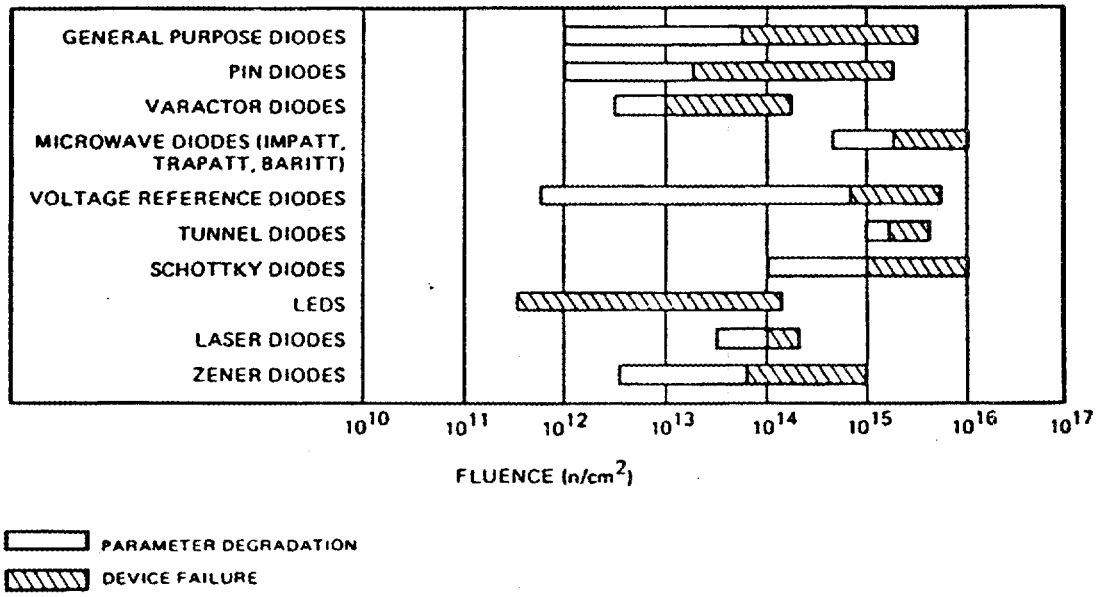

Figure 8a. Device degradation versus fluence for several diode types.

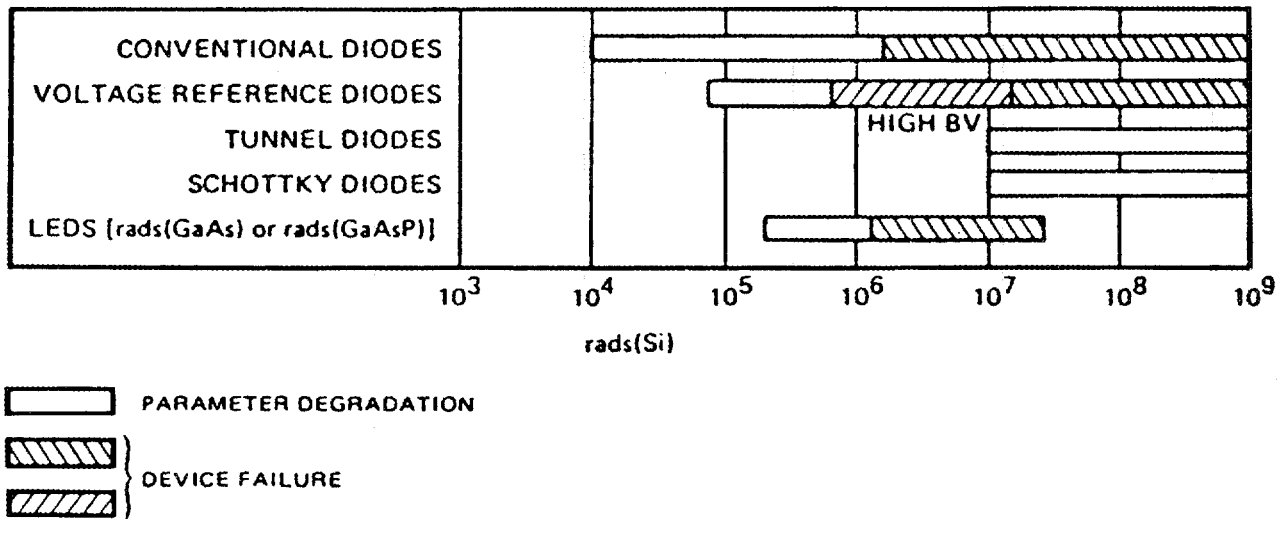

Figure 8b. Device degradation versus ionizing dose for several diode types.

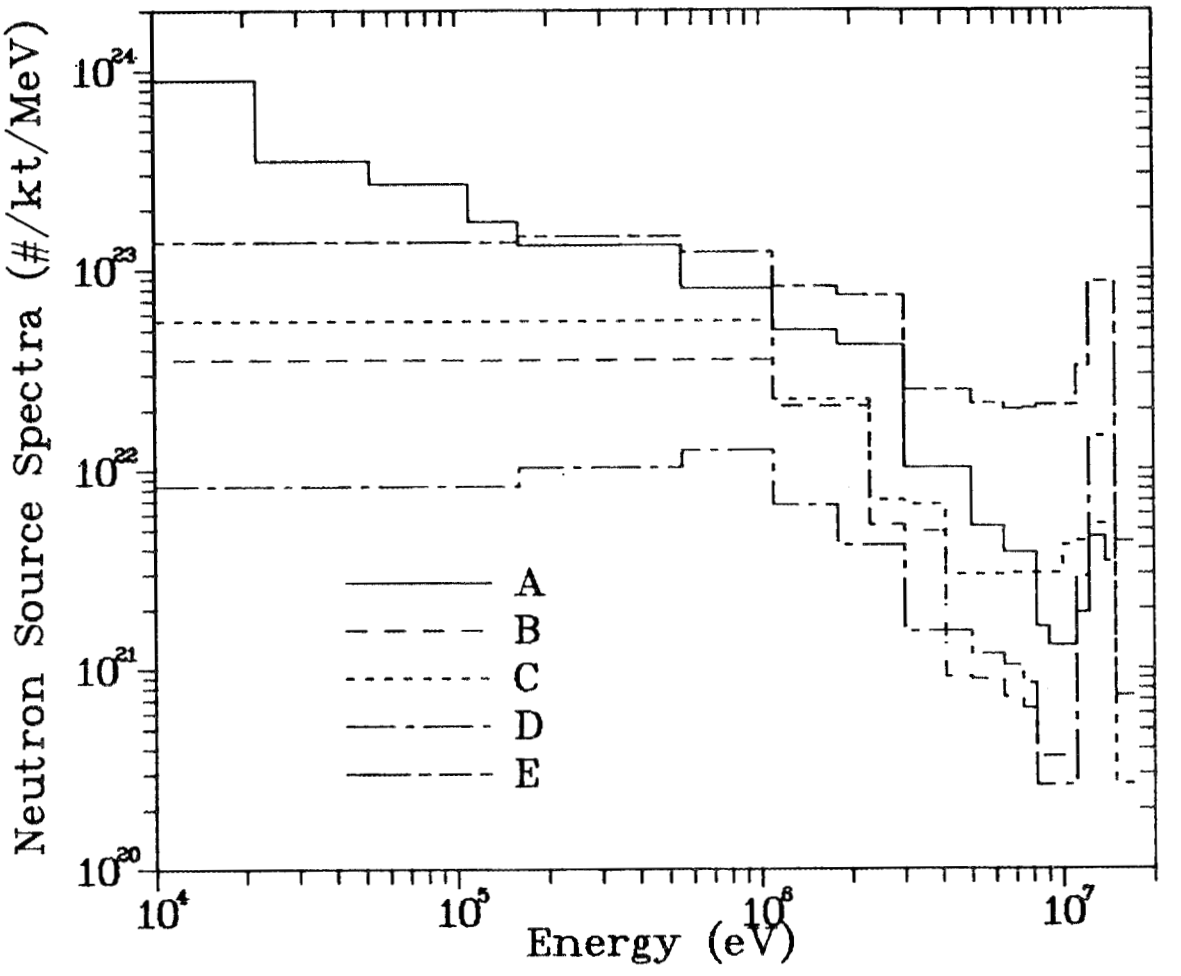

A = Tactical Weapon, Rhoades Reference 23
B = Fission Weapon, Dolan Reference 25
C = Thermonuclear Weapon, Dolan Reference 25
D = Tactical Weapon, Gsponer Reference 24
E = Enhanced Radiation Weapon, Gsponer Reference 24

Figure 9. A comparison of nuclear weapon neutron spectra from literature (kt=kTon).

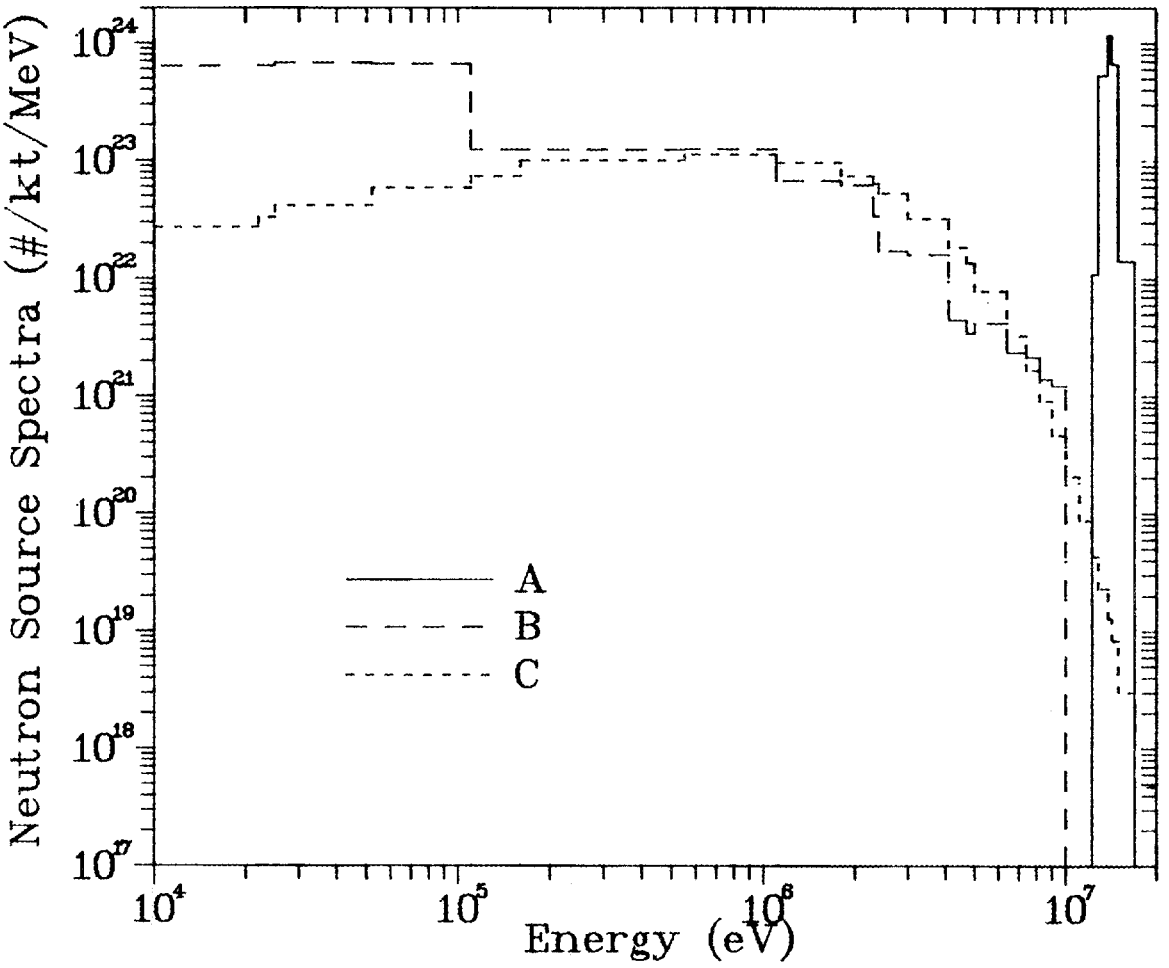

A = D–T 14 MeV normalized to 1.49×10^{24} n/kTon
B = Fission normalized to 3.18×10^{23} n/kTon
C = $e^{-E} \sinh \sqrt{2E}$ normalized to 3.18×10^{23} n/kTon

Figure 10. Additional nuclear weapon neutron spectra from literature (kt=kTon).

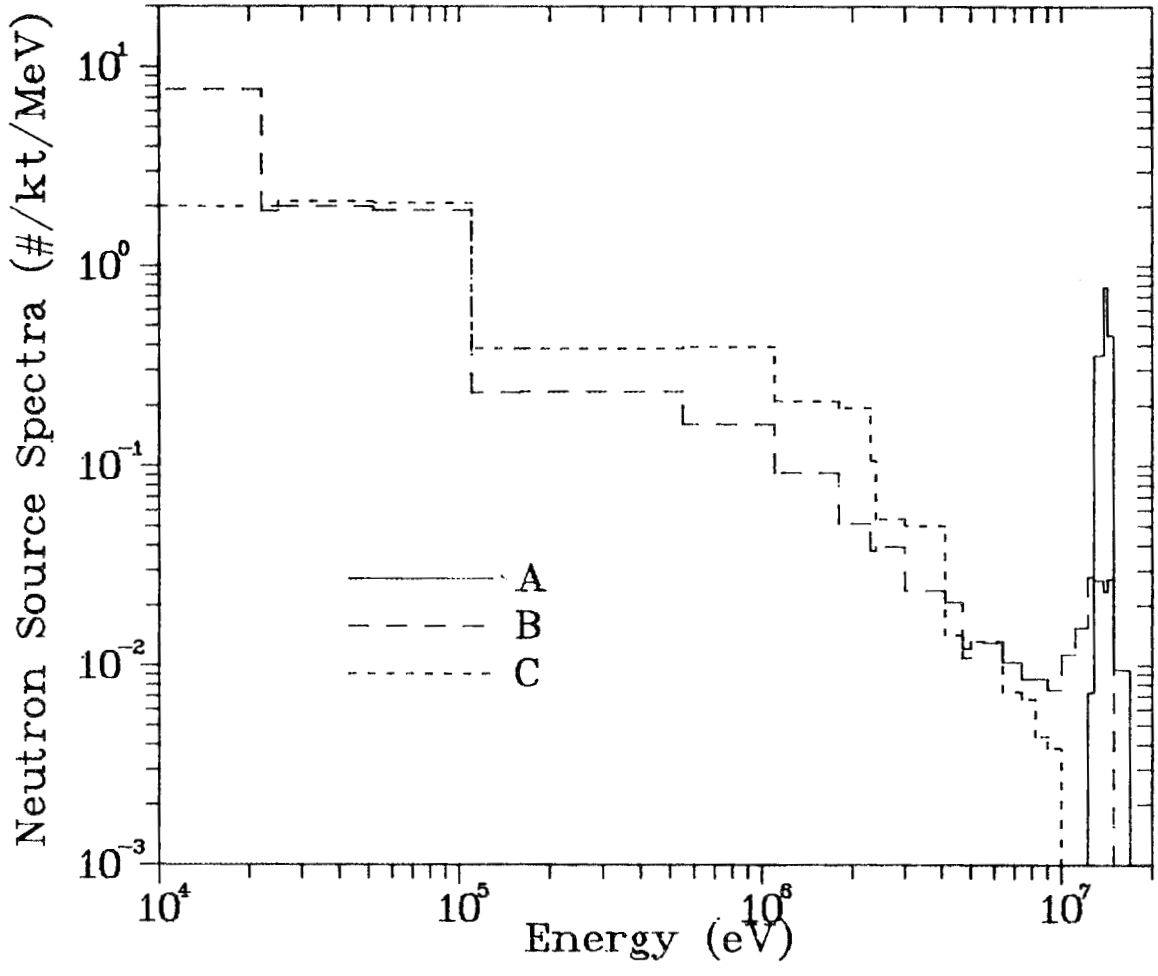

A = D–T 14 MeV, Bartine Reference 13
B = Thermonuclear, Bartine Reference 13
C = Fission, Bartine Reference 13

Figure 11. Normalized nuclear weapon neutron spectra.

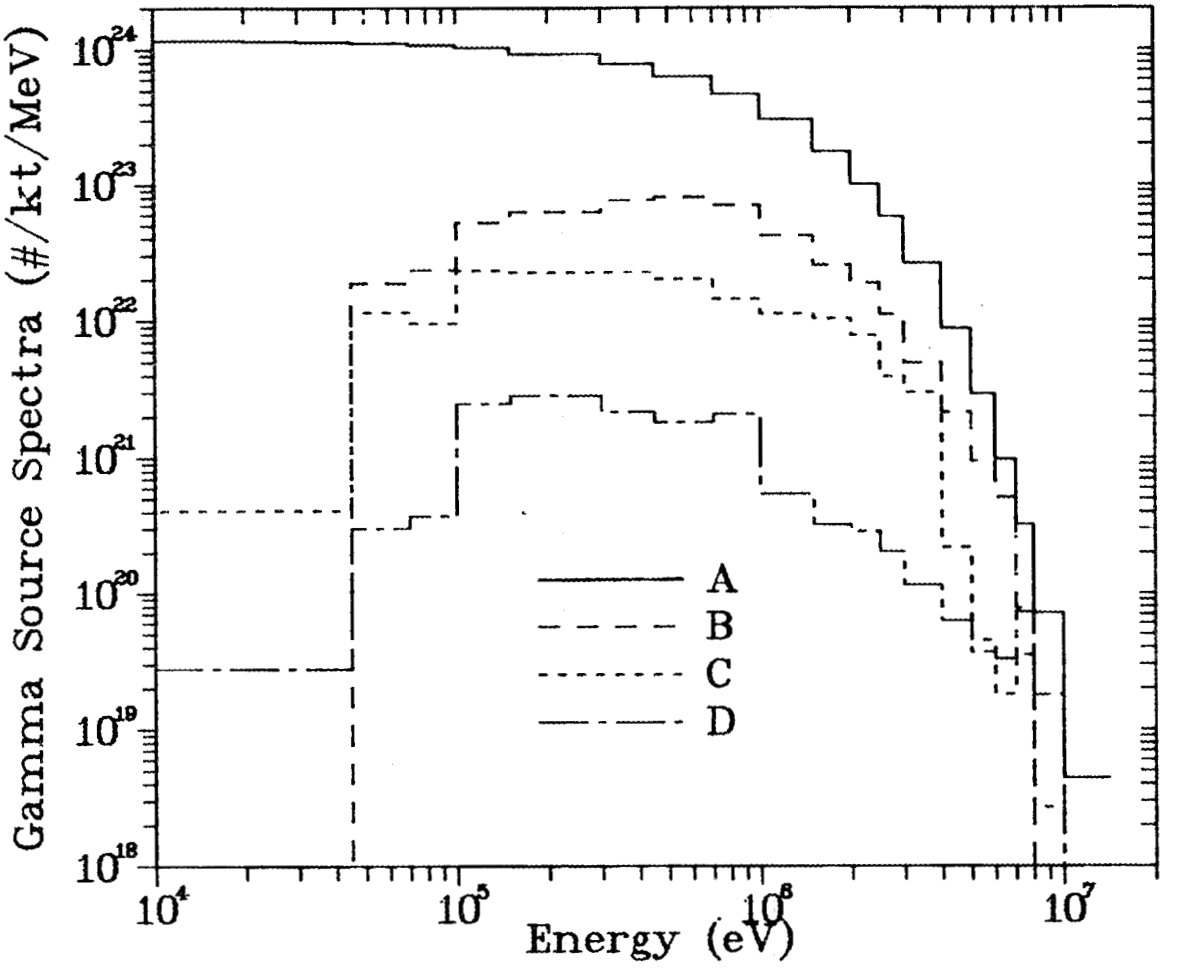

A = Prompt fission normalized to 1.058×10^{24} γ/kTon
B = Gabriel, Reference 26
C = Nagasaki normalized to 3.79×10^{22} γ/kTon
D = Hiroshima normalized to 3.79×10^{22} γ/kTon

Figure 12. A comparison of nuclear weapon gamma ray spectra from literature (kt=kTon).

Table 6

Displacements Per Atom (Electrons, Positrons, and X-rays) Cross Sections

Electrons and Positrons*		X-rays	
Energy (MeV)	Cross Section (barns)	Energy (MeV)	Cross Section (barns)
0.165	0.0	0.165	0.0
0.170	6.9	0.500	0.006
0.180	12.6	1.00	0.350
0.190	15.8	1.50	0.720
0.200	18.6	2.00	1.21
0.210	21.0	2.50	1.73
0.220	23.3	3.00	2.23
0.240	27.5	3.50	2.76
0.260	32.0	4.00	3.28
0.280	33.5	4.50	3.82
0.300	36.0	5.00	4.50
0.320	38.4	5.50	5.12
0.340	40.5	6.00	5.75
0.360	42.8	6.50	6.40
0.380	44.2	7.00	7.00
0.400	46.0		
0.430	48.0		
0.460	49.5		
0.500	51.5		
1.00	70.0		
1.50	88.0		
2.00	103.		
2.50	115.		
3.00	124.		
3.50	133.		
4.00	141.		
4.50	148.		
5.00	155.		
5.50	160.		
6.00	165.		
6.50	170.		
7.00	174.		

*See text on equating electron and positron cross sections.

"$e^{-E}\sinh\sqrt{2E}$" and "D-T" would be used for the fission neutron and fusion neutron source spectra, respectively (see Figure 10) and "prompt fission" would be used for the gamma source spectrum (see Figure 12). These spectra are given in Tables 7 and 8. These spectra will be normalized to 3.18×10^{23} $n/kTon$, 1.49×10^{24} $n/kTon$, and 1.06×10^{24} $\gamma/kTon$, respectively, which represents a 100% efficient device ($1kTon = 10^{12}$ cal.).

To obtain a spectrum for a thermonuclear device, a combination of 90% "pure 14 MeV," 10% "pure fission," and 10% "prompt fission," was used.

A nuclear detonation will heat the device and surrounding material to tens of millions of degress Kelvin. Due to this large temperature, black body radiation will occur in the form of X-ray radiation. Approximately 75% of the total energy emitted during a detonation will appear in this form of emission.[27] X-ray radiation will be reduced rather rapidly if a nuclear detonation occurs in the atmosphere due to absorption in the air and to $1/R^2$ divergence. However, in space, only $1/R^2$ divergence is initially available and shielding must be provided to reduce this large amount of energy to acceptable levels.

The differential energy distribution (X-rays/unit energy) associated with X-rays can be written

$$\frac{dN(E,kT)}{dE} \propto \frac{E^2}{e^{E/kT}-1}$$

where N is the number of X-rays with energy E about dE and kT is the temperature of the emitting object.[28] A plot of this distribution is given in Figure 13 for various kT values, 1 keV, 2 keV, 5 keV, 10 keV, 15 keV, 20 keV, and 25 keV. Each curve has been normalized to one X-ray. As the temperature of the black body radiator increases, the emission spectrum hardens. For the temperatures shown, the average energy of an emitted X-ray is 2.66-, 5.38-, 13.5-, 27.0-, 40.4-, 53.9-, and 67.4-keV.

Directed particle beams (neutral protons, alpha particles, and heavy ions) are also being considered as possible weapons for space. As a consequence, dose levels induced by these particles must be calculated. The energy range under consideration includes 30 to 200 MeV/nucleon. Since proton accelerators will probably be built and tested first, this type of beam will be treated in this scoping study. The energies considered are 50, 100, and 200 MeV. In addition, it will be assumed that the particle beam has diverged such that it completely illuminates the projected area of the KEW shield.

2.4.2. Van Allen Belt Protons

To perform calculations dealing with the Van Allen belt protons, it is necessary to know the energy and angular distributions of this radiation. In passing through these belts, a spacecraft will encounter various flux levels. To determine the average particle flux $\phi(E)$ that is incident on the spacecraft during orbit requires integrating over time, i.e.,

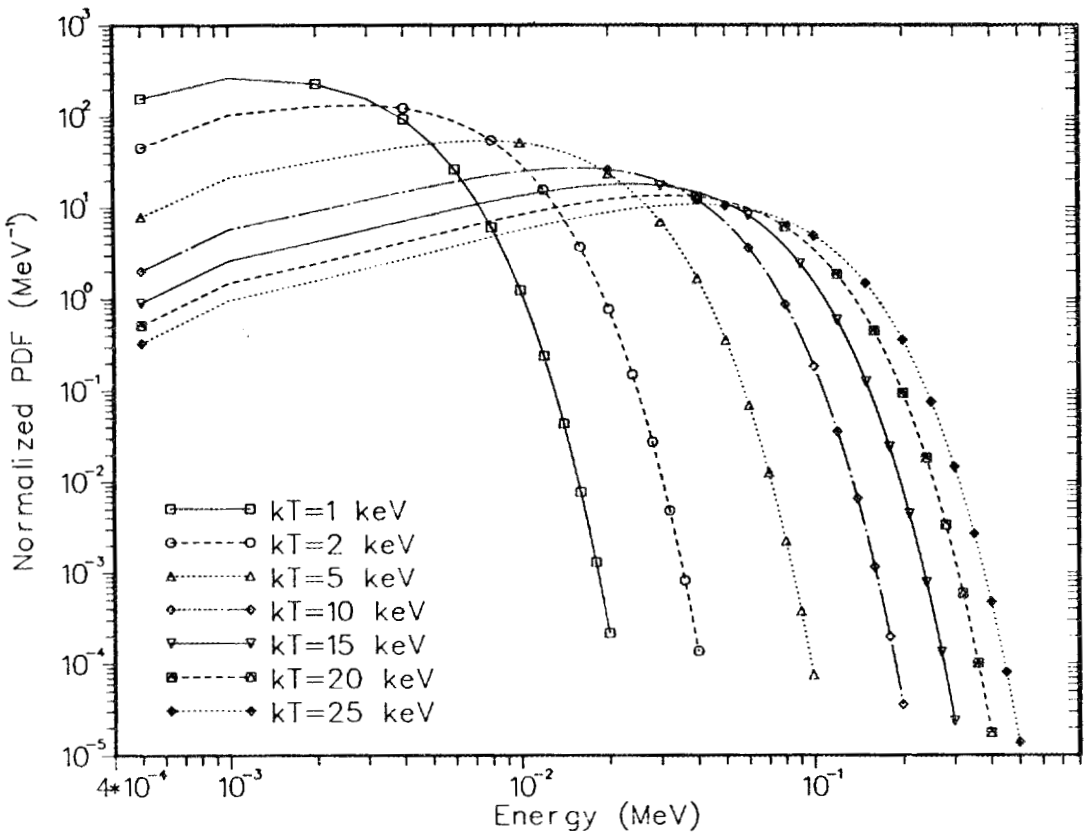

Figure 13. Black body X-ray spectra for various kT values.

Table 7

Selected Neutron Source Distributions

Group	Upper Energy Boundary (MeV)	Neutron Sources: Pure 14 MeV	Neutron Sources: Pure fission[a]
1	19.6	0.0	3.99−6
2	16.9	1.89−02[b]	1.89−5
3	14.9	3.12−01	1.81−5
4	14.2	3.12−01	1.61−5
5	13.8	3.54−01	7.23−5
6	12.8	4.37−03	8.11−5
7	12.2	0.0	2.99−4
8	11.1	0.0	7.10−4
9	10.0	0.0	1.45−3
10	9.0	0.0	2.29−3
11	8.2	0.0	4.18−3
12	7.4	0.0	1.02−2
13	6.4	0.0	3.43−2
14	5.0	0.0	1.28−2
15	4.7	0.0	3.48−2
16	4.1	0.0	1.11−1
17	3.0	0.0	9.90−2
18	2.4	0.0	1.99−2
19	2.3	0.0	1.16−1
20	1.8	0.0	2.10−1
21	1.1	0.0	1.93−1
22	5.5−01	0.0	1.22−1
23	1.6−01	0.0	1.15−2
24	1.1−01	0.0	1.06−2
25	5.2−02	0.0	3.51−3
26	2.5−02	0.0	3.10−4
27	2.2−02	0.0	1.02−3
28	1.0−02	0.0	3.64−4
29	3.4−03	0.0	7.14−5
30	1.2−03	0.0	1.26−5
31	5.8−04	0.0	5.92−6
32	1.0−04	0.0	3.85−7
33	2.9−05	0.0	5.46−8
34	1.1−05	0.0	1.42−8
35	3.1−06	0.0	1.97−9
36	1.1−06	0.0	4.07−10
37	4.1−07	0.0	1.20−10
	1.0−11		
TOTAL		1.00	1.00

[a] $\frac{dN}{dE} \propto \sinh(\sqrt{2E})e^{-E}$.

[b] Read 1.89×10^{-2}.

Table 8

Prompt Gamma Fission Source

Group	Upper Energy Boundary (MeV)	Gamma/Source Gamma
1	14.0	1.65–5*
2	10.0	1.34–4
3	8.0	3.02–4
4	7.0	9.08–4
5	6.0	2.73–3
6	5.0	8.19–3
7	4.0	2.46–2
8	3.0	2.70–2
9	2.5	4.69–2
10	2.0	8.12–2
11	1.5	1.41–1
12	1.00	1.30–1
13	0.70	1.47–1
14	0.45	1.09–1
15	0.30	1.29–1
16	0.15	4.79–2
17	0.10	3.01–2
18	0.070	2.58–2
19	0.045	1.58–2
20	0.030	1.07–2
21	0.020	1.08–2
	0.010	
TOTAL		0.98

*Read as 1.65×10^{-5}.

$$\phi(E) = \frac{1}{T}\int_0^T \phi'(E, B(t), L(t))dt$$

where $B(t)$ is the magnetic field intensity, $L(t)$ is the magnetic shell parameter, (B and L represent a coordinate system developed by C. E. McIlwain[29] for mapping magnetically trapped particles) and T is a time that must be sufficiently large so that $\phi(E)$ is independent of T. Several computer codes exist to calculate these time-averaged particle spectra.[30]

The angular distributions of these particles incident on the spacecraft are assumed to be isotropic. This assumption is made because of a lack of adequate data, and in some cases, may lead to poor results.

The differential proton flux in the Van Allen belt for circular orbits of 240 and 1500 nautical miles for various inclinations is shown in Figures 14 and 15. The proton flux is not zero at energies <30 MeV. However, the KEW shield will stop these particles and they will not contribute to the silicon dose. In addition, the assumption is made here that all Van Allen belt proton spectra are zero above 1000 MeV. This choice of 1000 MeV as the energy above which there are no trapped protons in the earth's magnetic field is largely arbitrary. The assumption of a zero flux above 1000 MeV is made because of a lack of data and not because there can be no trapped particles at higher energies.

2.4.3. Van Allen Belt Electrons

The differential electron flux in the Van Allen belt for a circular orbit of 1500 nautical miles for various inclinations is shown in Figure 16. In contrast to the high energy protons trapped in the belt, the electron energies are low, on the order of a few MeV. Due to the very short ranges of these particles, the majority of the dose in the silicon is expected to result from secondary bremstrahlung gamma rays which are produced by the primary electrons.

2.4.4. Energy Spectra of Solar Flare Particles

The intensity, energy spectra, and angular distribution of solar flare particles vary widely from event to event and as a function of time during an event. The duration of a flare is on the order of a day. For most shielding purposes, it is sufficient to consider only the time-integrated effect of the flare, so only the time-integrated flare spectra have been considered in these calculations. During the early stages of a flare, the angular distribution of the particles is quite anisotropic, but the distribution tends toward isotropy and is isotropic during most of the life of the event.

The differential energy spectrum of the particles in a flare may be written[31]

$$-\frac{dJ_j}{dE} = \frac{J_{oj}}{Z_j P_o}\frac{E + m_j}{\sqrt{E^2 + 2m_j E}}\exp\left[-\frac{\sqrt{E^2 + 2m_j E}}{Z_j P_o}\right]$$

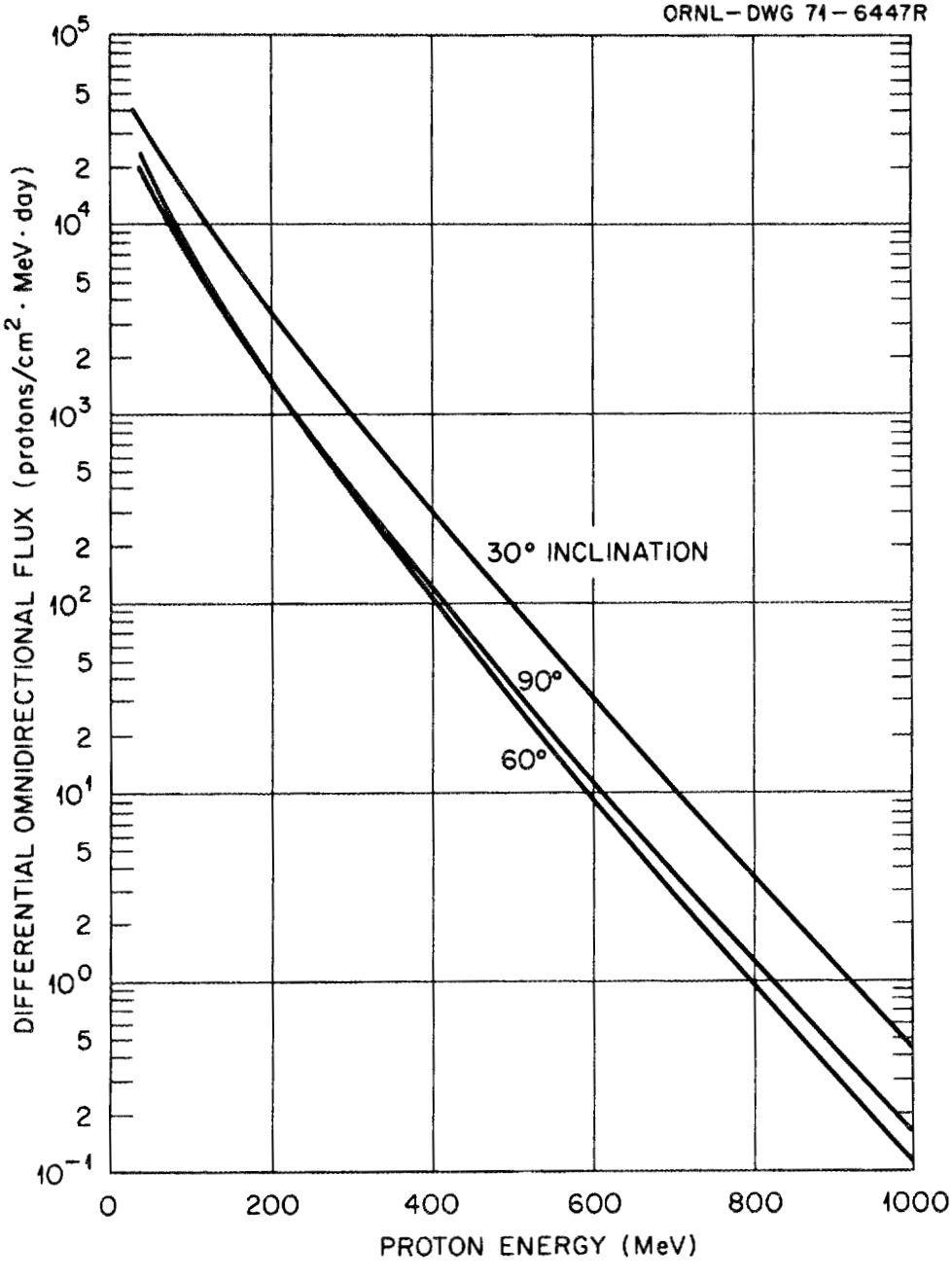

Figure 14. The differential proton flux in the Van Allen belt for circular orbits with several inclinations at an altitude of 240 nautical miles.

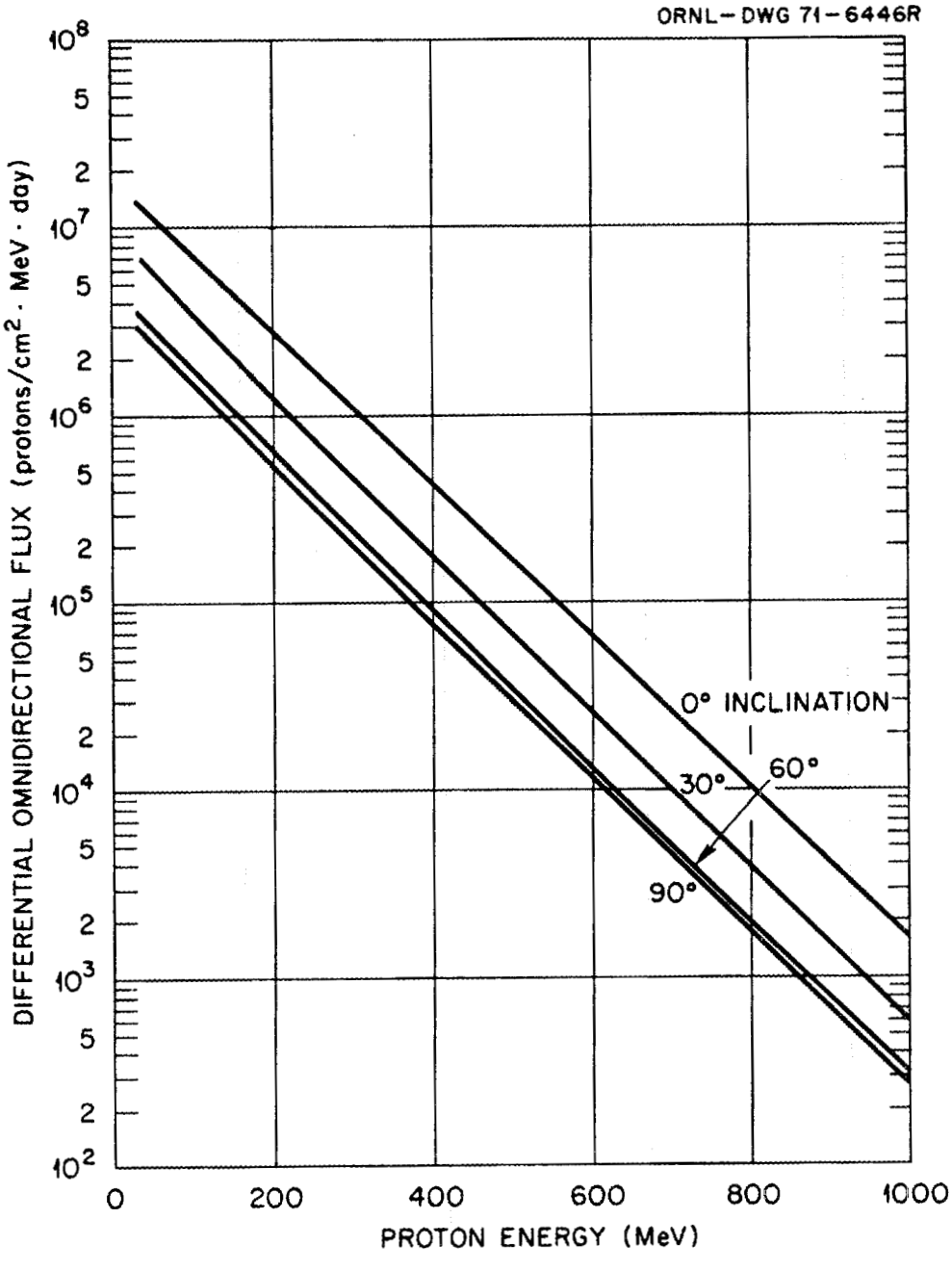

Figure 15. The differential proton flux in the Van Allen belt for circular orbits with several inclinations at an altitude of 1500 nautical miles.

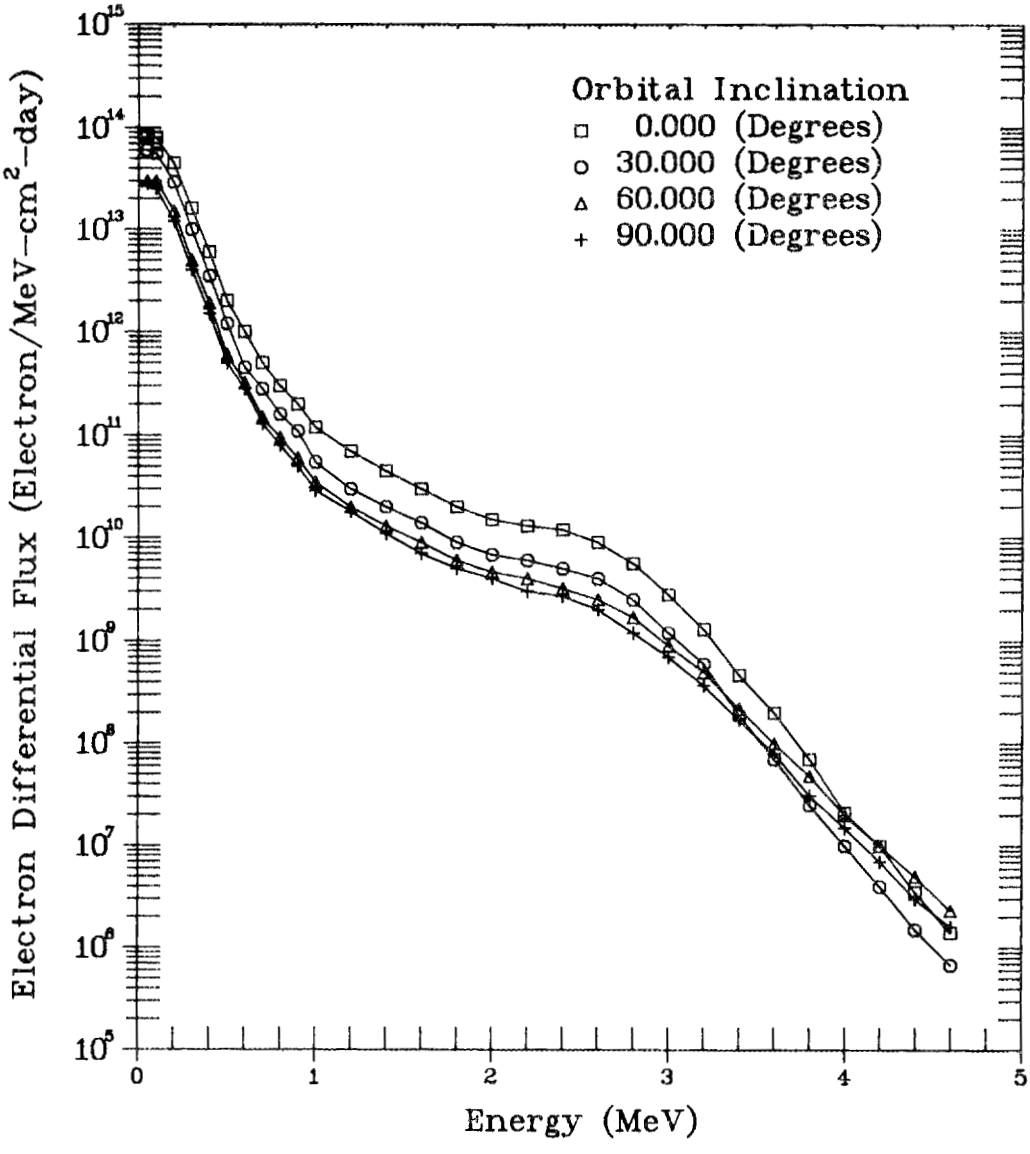

Figure 16. Electron differential flux versus energy at orbital altitude 1500 nautical miles for several orbital inclinations.

where

j = protons or alphas,

m_j = mass of the particle of type j,

Z_j = charge of the particle of type j, and

J_{oj}, P_o = the parameters that characterize a particular flare.

Typical values of P_o (rigidity) vary between 50 and 200 MV and typical numbers of particles >30 MeV in a flare vary from $\approx 10^6$ to $\approx 10^9$ protons/cm^2. J_{oj} is basically a normalization constant.

For the present calculations, the flare spectra have been normalized to 10^9 protons/cm^2 (30 MeV $< E <$ 3000 MeV) and the values of P_o considered are 50, 100, and 200 MV. Plots of solar flare spectra are given in Figure 17.

2.4.5. Galactic Proton Spectra

Galactic cosmic rays are composed of approximately 87% protons, 12% alpha particles, and 1% heavier nuclei, and have an energy spectrum which decreases rapidly with increasing energy, but which extends to very high energies. For practical purposes, their angular distribution may be taken to be isotropic outside of the magnetosphere as has been assumed in the present calculations. The omnidirectional fluxes of protons and alpha particles with kinetic energy greater than E per nucleon are plotted in Figure 18 as a function of energy divided by the number of nucleons in a given species. The solar-minimum proton and alpha spectra are taken from the review of McDonald[32] and the solar-maximum proton spectrum is based on the 1959 spectrum predicted by the solar-wind modulation theory of Durgaprasad et al.[33] The solar-maximum alpha particle spectrum is taken from reference 34 and from the experimental data of McDonald,[35] Frier et al.,[36] and Fan et al.[37] The differential omnidirectional solar-minimum and solar-maximum proton and alpha particle flux spectra per unit energy per nucleon, which, when integrated over energy per nucleon, gives the corresponding fluxes in Figure 18, are given in Figure 19.

The variation between the maximum and minimum in the galactic cosmic ray fluxes of protons and alpha particles results from changes in solar activity and generally follows the approximate 11-year cycle of solar activity. When the maximum activity of the solar cycle is reached (as measured by the sunspot number, for example), the cosmic ray intensity reaches a minimum and then starts increasing until the maximum is reached at the time of minimum solar activity. For shielding and damage purposes, the solar-minimum and solar-maximum spectra may be taken as upper and lower limits, respectively, on the particle fluxes that will be encountered in space outside the magnetosphere.

Shielding calculations for incident galactic cosmic rays are somewhat different from those for solar cosmic rays (solar flares) and Van Allen belt protons because

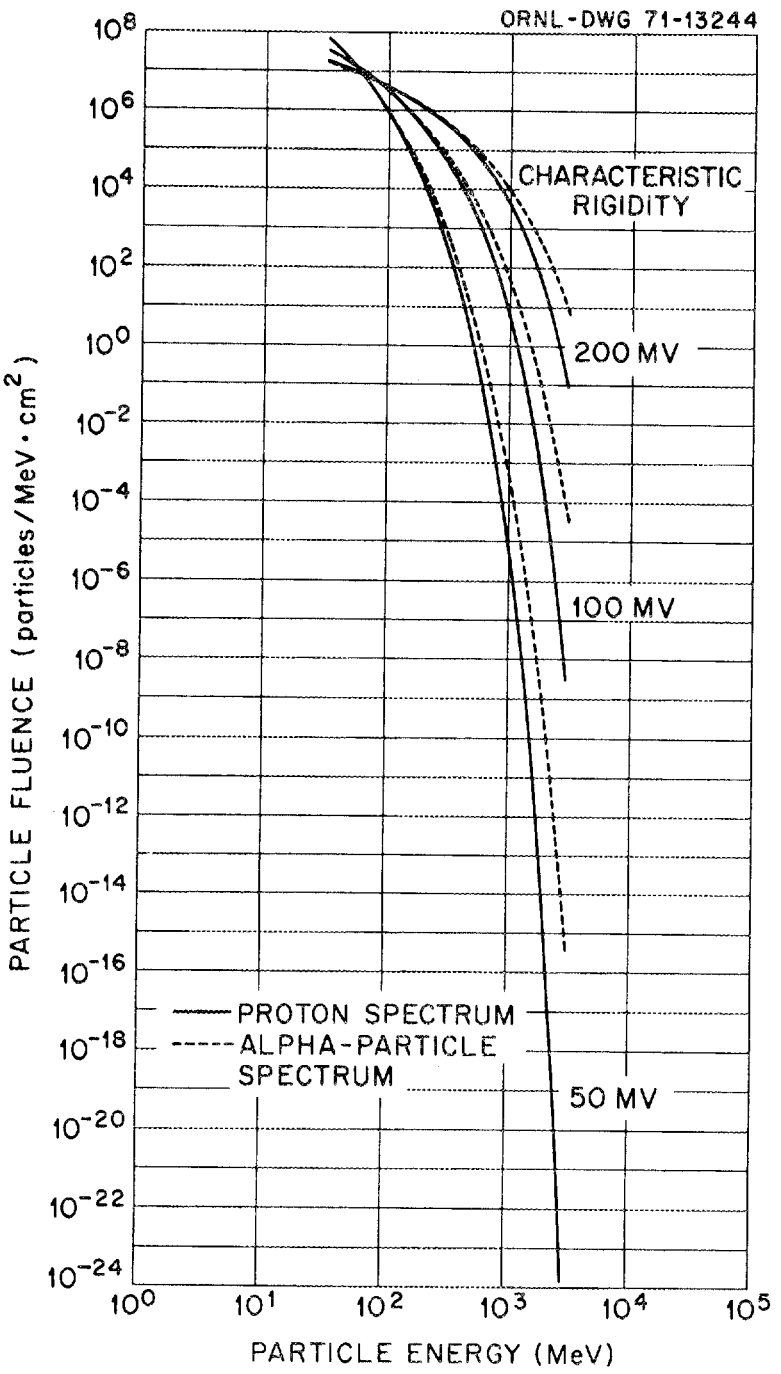

Figure 17. Solar-flare proton and alpha-particle spectra for characteristic rigidities of 50, 100, and 200 MV.

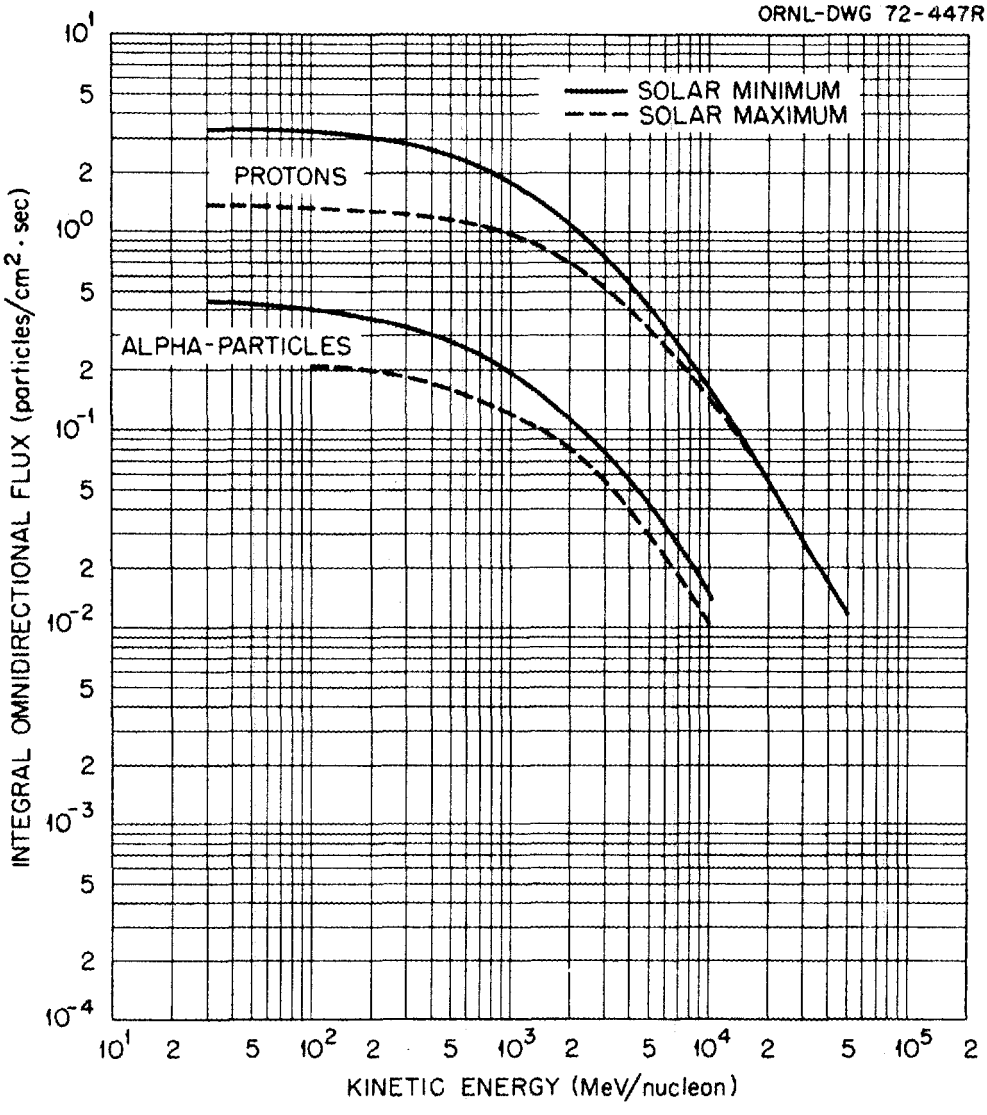

Figure 18. Integral flux of galactic cosmic-ray protons and alpha particles.

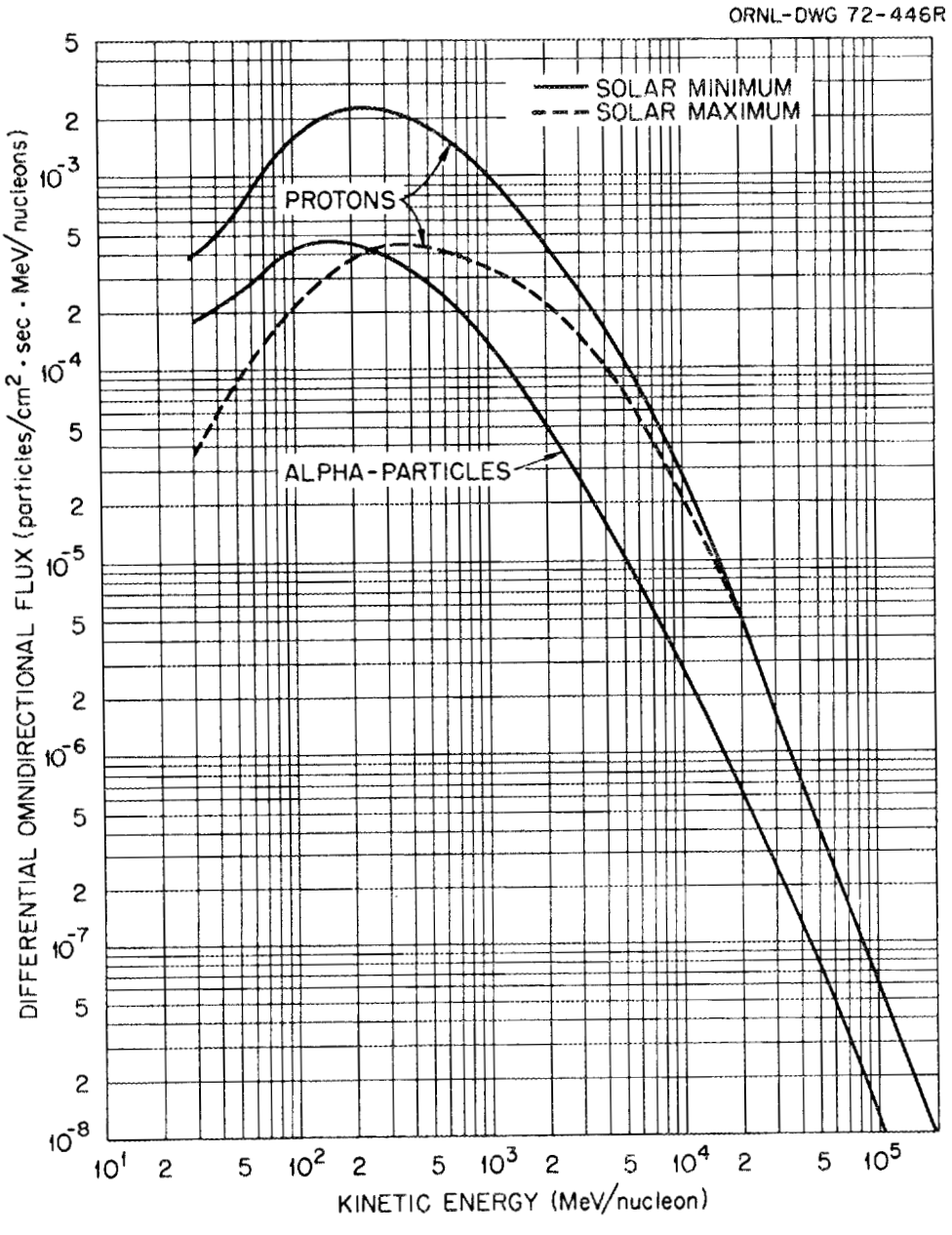

Figure 19. Differential omnidirectional galactic proton flux at solar minimum and solar maximum and alpha-particle flux at solar minimum.

of the much higher energies involved. It has been shown in previous calculations that to a reasonable approximation for small to medium amounts (5-30 g/cm^2) of shielding, the secondary particles produced by nuclear reactions may be neglected or approximated in shielding against solar cosmic ray protons and Van Allen belt protons.[38] In the case of galactic cosmic rays, because of the higher energies involved, this is only the case when there is minimal shielding, at least to an accuracy factor of 2-3. To carry out shielding calculations when a large amount of shielding is present requires a substantial amount of differential particle-production cross-section data from high energy nuclear collisions. Fortunately, these preliminary calculations involved small amounts of shielding and therefore only unattenuated primary ionization energy deposition needs to be considered. When more shielding is added around the silicon, secondary particle-nuclear collisions will have to be considered if realistic dose levels are to be calculated.

2.5. ENERGY AND ANGULAR BIASING OF THE INCIDENT SPECTRA

Some of the damage levels calculated in this report were obtained with energy and angular biasing of the incident source distributions. These radiation sources included the Van Allen belt protons and electrons, the solar flare protons, and the galactic protons. The unbiased source distributions for Van Allen belt proton and electron spectra, solar-flare proton spectra, and galactic proton spectra may be expressed in the form

$$J(E,\bar{\Omega}) = \Phi_o G(E,\vec{\Omega})\,, \tag{1}$$

where

$J(E,\vec{\Omega}) =$ the incident source particle current,

$\Phi_o =$ a normalization constant, and

$G(E,\bar{\Omega}) = F(E,\mu,\phi) =$ the unbiased probability density function (pdf) for source particles having energy E and directions $\mu = \cos\theta$ and ϕ.

The unbiased pdf is normalized so that

$$\int_{E_{\min}}^{E_{\max}} \int_o^1 \int_o^{2\pi} dE\, d\mu\, d\phi\, F(E,\mu,\phi) = 1 \tag{2}$$

for all particles having energies greater than the cutoff energy $E_{\min}$.

Let $\Phi(E)$ be the omnidirectional (over 4π) flux spectrum, then

$$J(E,\bar{\Omega}) = \Phi(E)\left(\frac{\mu}{2}\right)\left(\frac{1}{2\pi}\right). \tag{3}$$

Integrating Eq. (3) over all directions and over all particle energies above the cutoff energy $E_{\min}$ leads to the normalization constant Φ_o; that is,

$$\Phi_o = \int_{E_{\min}}^{E_{max}} dE\Phi(E)\int_o^1 d\mu\,\frac{\mu}{2}\int_o^{2\pi} d\phi\,\frac{1}{2\pi} = \frac{\psi(E_{\min})-\psi(E_{\max})}{4}, \tag{4}$$

where

$$\psi(E) = \int_E^{\infty} \Phi(E')dE'.$$

Introducing $F(E,\mu,\phi) = f(E)\,g(\mu)\,h(\phi)$, the unbiased source distribution may be written

$$J(E,\vec{\Omega}) = \frac{\psi(E_{\min})-\psi(E_{\max})}{4}\,f(E)\,g(\mu)\,h(\phi), \tag{5}$$

where

$$\begin{aligned}
\tfrac{\psi(E_{\min})-\psi(E_{\max})}{4} &= W_o = \text{the initial weight assigned to each source particle,}\\
f(E) &= \text{the pdf in energy} = \tfrac{\Phi(E)}{\psi(E_{\min})-\psi(E_{\max})},\\
g(\mu) &= \text{the pdf in polar angle} = 2\mu,\\
h(\phi) &= \text{the pdf in azimuthal angle} = (2\pi)^{-1}.
\end{aligned}$$

To improve the statistical fluctuations in the dose distributions in the silicon, the source particle energies and directions were not sampled from the pdf's given above but instead were sampled from biased distributions. These biased distributions were constructed so that those source-particle energies and directions that resulted in relatively large dose contributions were sampled more frequently. Statistical weighting fractions to account for the biasing were then applied to each source particle so that the original incident source spectral shape and normalization are preserved. For the energy biasing, the energy intervals, ΔE, and the sampling fractions for each energy interval used, P_E, are summarized in Table 9 for Van Allen belt, solar-flare and galactic spectra. The particle energy was selected uniformly within each energy interval according to the relation

$$E_S = E_U - R(E_U - E_L) = E_U - R(\Delta E), \tag{6}$$

Table 9

Energy Intervals and Sampling Fractions for Source Energy Biasing in HETC Calculations

Energy Interval (MeV)	Fraction (p_E)
Van Allen Belt Proton Spectra	
30-40	0.10
40-50	0.13
50-100	0.35
100-200	0.25
200-400	0.12
400-1000	0.05
Van Allen Belt Electron Spectra	
0.1-0.5	0.05
0.5-1.0	0.05
1.0-1.5	0.05
1.5-2.0	0.10
2.0-3.0	0.35
3.0-4.6	0.40
Solar-Flare Proton Spectra	
30-40	0.025
40-50	0.025
50-100	0.05
100-200	0.30
200-400	0.50
400-3000	0.10
Galactic Proton Spectra	
30-100	0.10
100-500	0.40
500-1000	0.20
1000-10000	0.20
10000-60000	0.07
60000-200000	0.03

where

$E_S =$ the sample energy,
$E_U, E_L =$ the upper and lower bounds, respectively, of the energy interval in which the sample is taken, and
$R =$ a random number between 0 and 1.

The biased pdf in energy is now given by

$$f^*(E) = \frac{P_E}{\Delta E}\,, \tag{7}$$

and Eq. (5) may be rewritten as

$$J(E,\bar{\Omega}) = W_o \left[\frac{f(E)}{f^*(E)}\right] f^*(E)\, g(\mu)\, h(\phi)\,. \tag{8}$$

where

$$\left[\frac{f(E)}{f^*(E)}\right] = W_E = \text{the weight factor due energy biasing}.$$

Then

$$J(E,\vec{\Omega}) = W_o\, W_E\, f^*(E)\, g(\mu)\, h(\phi)\,. \tag{9}$$

Angular biasing of the incident spectra was accomplished using similar techniques. The angular intervals, $\Delta\mu$, and the sampling fractions, p_μ, for samples within various solid angles are summarized in Table 10.

Particles were selected uniformly within each angular interval according to the formula

$$\mu' = \mu_j - R(\mu_j - \mu_{j+1}) = \mu_j - R\,\Delta\mu\,. \tag{10}$$

The biased pdf in polar angle can now be written

$$g^*(\mu) = \frac{P_\mu}{\Delta\mu}\,,$$

and Eq. (9) may be written

$$J(E,\bar{\Omega}) = W_o\, W_E\, W_\mu\, f^*(E)\, g^*(\mu)\, h(\phi)\,, \tag{11}$$

where

Table 10

Angular Intervals and Sampling Fractions for Source Particle Biasing in HETC Calculations

Angular Interval[a] ($\Delta\mu$)	Sampling Fraction (p_μ)	
	Van Allen Belt, Solar-Flare, and Galactic Proton Spectra	Van Allen Belt Electron Spectra
0.0-1.56	0.90	0.11
1.56-2.59	0.02	0.11
2.59-3.63	0.02	0.11
3.63-4.67	0.01	0.11
4.67-5.71	0.01	0.11
5.71-6.75	0.01	0.11
7.80-45.0	0.01	0.11
45.0-90.0	0.01	0.12

[a]Angles listed in degrees (θ) and not $\cos\theta$

$$W_\mu = \left[\frac{g(\mu)}{g^*(\mu)}\right] = \left[\frac{2\mu\Delta\mu}{p_\mu}\right] = \begin{array}{c}\text{the weight factor due to} \\ \text{direction biasing interval } \Delta\mu \text{ about } \mu.\end{array}$$

Since all source particles were uniformly sampled in the azimuthal angles, $h^*(\phi) = h(\phi)$.

Since the black body radiation completely and uniformly illuminates the projected surface of the spacecraft, and since the silicon represents a small projected area, a spacially biased source distribution was used. Let p_1 represent the biased probability of sampling over the silicon, then $1 - p_1 = p_2$ equals the probability of sampling over the rest of the spacecraft. To correct for this biased sample requires the following modification of the particle weight. If the sample is over the silicon area, the weight becomes $w_1 = \left[R_{Si}^2/R_{\max}^2\right]/p_1$ where R_{Si} is the radius of the silicon and $R_{\max}$ is the radius of the spacecraft. If the sample is over the remaining area, the weight becomes

$$w_1 = \left[\left(R_{\max}^2 - R_{Si}^2\right)/R_{\max}^2\right]/p_2$$

A uniform sampling in energy was used to properly sample from the X-ray spectrum. This was to allow more high-energy particles to be obtained. The modification of the weight to adjust for this biased sample is

$$w_2 = \left[C(E_{\max}, kT)E^2/(e^{E/kT} - 1)\right] E_{\max}$$

where $E_{\max}$ is the maximum energy X-ray considered and $C(E_{\max}, kT)$ is the normalization constant for black body radiation for $E_{\max}$ and temperature kT. $E_{\max}$ was chosen such that 99.5% of the total energy in the distribution was considered. The final weight of the chosen X-ray particle is the product of the above weights, $w = w_1 \cdot w_2$.

Similar spatial weighting was used in both the directed particle beam and the nuclear weapon calculations. Also similar uniform energy weighting was used in the nuclear weapon calculations, i.e., the weight of the uniformly sampled particles are

$$w = f(E) \cdot E_{\max}$$

where

E is the sampled energy,

$E_{\max}$ is the maximum neutron or gamma energy, and

$f(E)$ is the differential energy spectra.

3. RESULTS

3.1. MAN-MADE RADIATION ENVIRONMENTS

This section describes the results of calculations that have been carried out to determine the radiation damage in silicon (and to the spacecraft) due to the various man-made radiation environments expected to be placed in space. In particular, the radiation damage due to fission and fusion weapon neutrons, gamma rays and X-rays are considered in addition to directed neutral particle beams of energy 50, 100, and 200 MeV.

3.1.1. Fusion and Fission Weapons

3.1.1.1. Neutrons and Gamma Rays

A number of damage responses arising from the prompt radiations emanating from a nuclear detonation have been calculated for a small Si sphere enclosed in a KEW shield. Most current nuclear weapons are thermonuclear and comprised of both a fission and fusion component. The prompt neutron output from these devices can be approximated by mixing a pure 14 MeV D-T neutron spectrum and a prompt fission neutron spectrum. The prompt gamma ray output can be approximated with a prompt fission gamma ray spectrum. These prompt neutron and gamma ray spectra are shown in Figures 10 and 12. The delayed radiation from a nuclear detonation was not considered in the present analysis.

Separate damage responses for silicon due to a pure fission spectrum, a pure 14 MeV spectrum, and a prompt fission gamma ray spectrum were obtained using the spherical spacecraft model depicted in Figure 1. This model was employed in the three-dimensional MORSE[8] Monte Carlo radiation transport code. The calculations were carried out using the DLC31[13] 37 neutron and 21 gamma ray energy group cross-section library discussed in Section 2. The radiation source, i.e., the radiation from the weapon, was treated by employing a normally incident plane source uniformly distributed over one side of the spacecraft. To improve the Monte Carlo statistics, spatial biasing was employed to direct more particles toward the relatively small projected area of the silicon. As noted in Section 2, this source representation is equivalent to imposing an isotropic flux condition over the entire surface of the spacecraft because of spherical symmetry. All calculations were normalized to a one kiloton output of neutrons and gamma rays assuming 100% efficiency. This assumption results in 3.18×10^{23} prompt fission neutrons,

1.49×10^{24} pure 14 MeV neutrons, and 1.06×10^{24} prompt fission gamma rays per kiloton of yield.

The responses obtained from these calculations consisted of (1) the neutron fluence above 0.11 MeV, i.e., the damage fluence, (2) the atom displacements per Si atom, i.e., the DPA, (3) the damage energy per unit mass deposited in Si, i.e., that part of the total energy deposition which leads to atom displacements, (4) the total energy deposited by prompt neutrons per unit mass, and (5) the total energy deposited per unit mass by prompt and secondary gamma rays. These responses are presented in Table 11. Each entry in Table 11 has units corresponding to the units of that particular response times m^2/kiloton, e.g., the total neutron energy deposition in Si has units of rads-m^2/kiloton. For a given device, absolute responses may be obtained from the values in Table 11 by multiplying by the yield in kilotons and dividing by the square of the separation distance in meters between the spacecraft and the device.

The data in Table 11 may be used to construct distance vs. yield curves. Examples of such curves for the amount of damage fluence which will produce electronic device failure and electronic device degradation, and the total energy deposition which will cause bit upset or data flow interruption are presented in Figure 20 for a pure fission nuclear device. The total energy deposition for a pure fission device is the sum of the neutron and gamma ray energy depositions listed under pure fission and the gamma ray energy deposition listed under prompt gamma rays. The separation distance D may be determined as a function of yield y from the following relationship:

$$D = [R \cdot y/L]^{1/2}$$

where R is the calculated value of the damage response of interest (taken from Table 11) and L is the damage limit for that response, i.e., the values listed in Figure 20. For a given yield, the separation distance indicated by the curves represents the minimum separation distance. If the separation distance is smaller than this value, the damage limit corresponding to a particular effect will be exceeded. Conversely, for a given separation distance, a yield which exceeds that indicated by the curves will also produce adverse effects by causing the particular damage limit to be exceeded.

3.1.1.2. Black Body X-Ray Radiation

A nuclear detonation will heat the weapon to tens of millions of degrees Kelvin. Due to this high temperature, black body radiation will occur in the form of X-rays. Approximately 75% of the total energy emitted during a detonation will appear in the form of X-rays.[27] If the detonation occurs in the atmosphere, the X-ray radiation will be reduced rapidly due to absorption in the air and the geometric ($1/R^2$) divergence. In space, however, only geometric divergence is initially available

Table 11

Radiation Damage Parameters from Pure Fission,
Prompt Gamma Rays, and Pure 14 MeV Radiation

R	Responses ($R \cdot m^2$/kTon) Pure Fission	Prompt Gamma Rays	Pure 14 MeV
Flux > 0.11 MeV (cm^{-2})	1.54+18[a]		1.09+19
DPA in Si (dpa)	4.54−03		3.02−02
Damage Energy in Si (rads)	9.80+07		6.50+08
Neutron Energy Deposition in Si (rads)	2.34+08		1.56+10
Gamma-Ray Energy Deposition in Si (rads)	9.12+07	2.72+09	1.33+09

[a]Read as 1.54×10^{18}

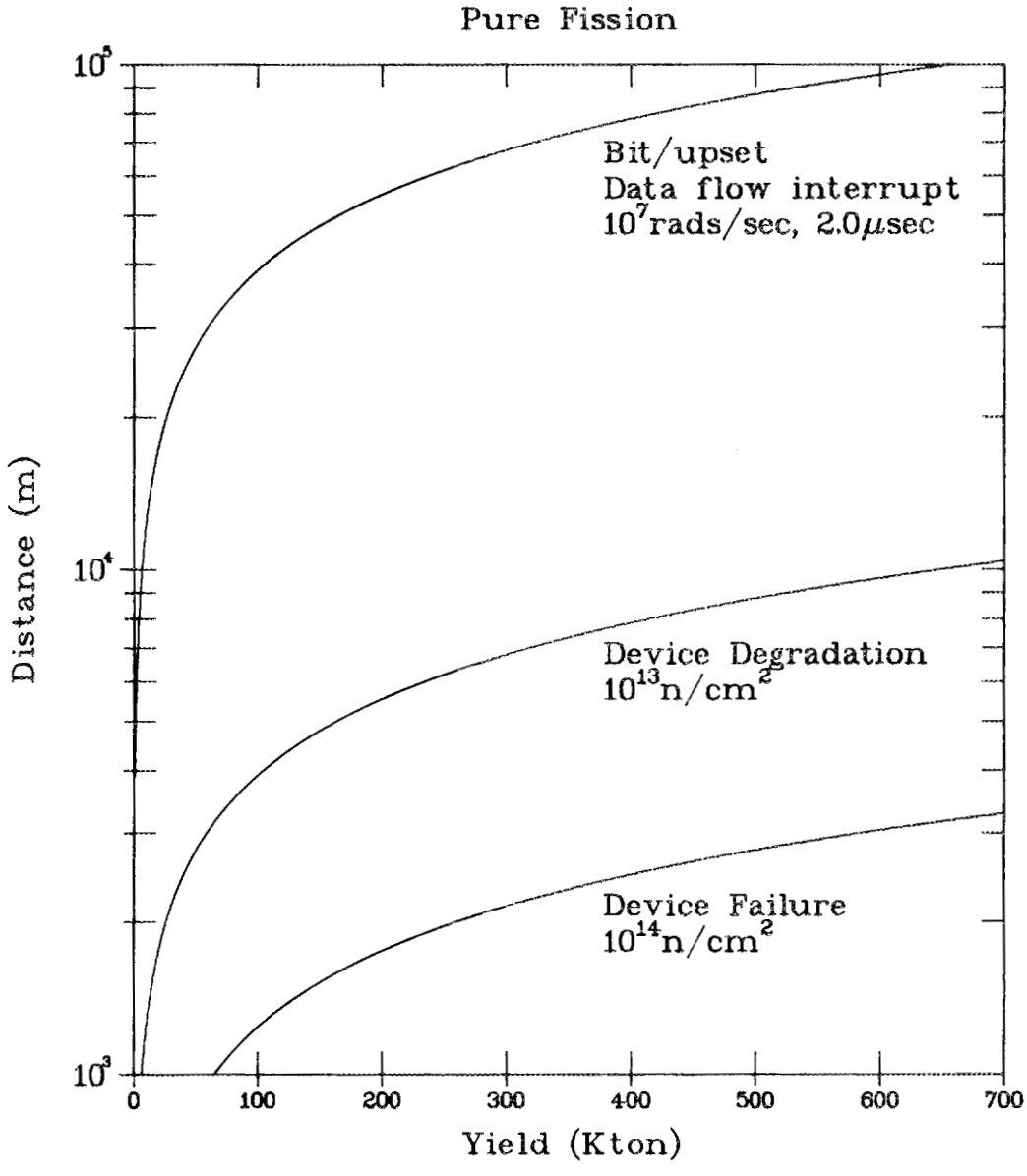

Figure 20. Device deterioration as a function of weapon yield and distance for a pure fission spectrum.

and therefore shielding must be provided to reduce this large amount of energy to acceptable levels.

Shielding and damage calculations were performed using the Electron Gamma-Ray Shower Code EGS and its cross section processor PEGS.[7] In particular, the energy deposition, particle tracklength, and displacements per atom (DPA) were calculated for the sensitive electronics of the spacecraft for various temperature black body radiators. Additionally, the energy deposition in the spacecraft hull was calculated to determine if enough energy was being deposited to melt the hull. The geometry used in the calculations is shown in Figure 1 and included only the KEW shield. The black body source spectra are presented in Section 2 for the various black body temperatures. Since the black body radiation completely and uniformly illuminates the projected surface of the spacecraft, and since the silicon represents a small projected area, a spacially biased source distribution was used. A detailed discussion of the biasing can also be found in Section 2.

Calculated results for the various black body temperatures are given in Table 12. The data at each temperature have been normalized on the assumption that 75% of the emitted energy is in the form of black body radiation. Due to the increasing average X-ray energy with increasing black body temperature, the absolute number of X-rays/kTon decreases as the temperature of the black body emitter increases. The results have been presented as a function of the kiloton yield of the device and the distance the spacecraft is from the detonation. Therefore, to obtain the absolute dose the spacecraft would receive from a detonation, (at a given temperature) multiply the data in Table 12 by the yield of the device (in kilotons) and divide by the distance squared from the detonation (in meters^2). Therefore, a one kiloton detonation at one kilometer would deposit 2.16×10^4 rads in the silicon and 7.86×10^5 rads in the aluminum hull for a 15 keV temperature black body emitter. Presenting the information in this manner allows for generation of spacecraft survivability curves given the dose levels needed to cause device failure (see Figure 20) or spacecraft melting. The general trend of the data presented in Table 12 shows the silicon dose increasing and the aluminum dose decreasing as the temperature of the black body emitter increases. Furthermore, the silicon dose starts to decrease at a temperature of 25 keV. These trends are attributable to the increase in the ranges of the X-rays as the average X-ray energy increases with increasing temperature and the X-ray source distribution gets harder as a function of energy. The collision DPA also increases as a function of increasing temperature and this data indicates that low DPA levels will lead to device damage or failure. The DPA calculated using the electron flux and the X-ray flux should agree since X-rays produce atom displacement through production of electrons or positrons. As seen in the results, the values for the DPA agree to a reasonable extent. Any differences can be attributed to the magnitude of the cross sections close to threshold values and to the treatment of the electrons produced by X-rays in reference 21.

3.1.2. Directed Neutral Particle Beams

Directed particle beams along with fusion and fission devices are expected to present the greatest radiation threat to the survivability of electronic components on a spacecraft. To evaluate the threat of directed particle beams, calculations were performed for incident beams composed of 50, 100, and 200 MeV hydrogen. In these calculations, the hydrogen beam was assumed to have diverged such that the entire projected surface area of the spherical spacecraft was illuminated with the plane wave beam. These calculations were performed using the CALOR code system[2] and considered both the unattenuated primary protons and full transport in the determination of the silicon dose. A synopsis of the calculational procedures used in the CALOR code system can be found in Section 2. Spherical geometry was used for the spacecraft in the calculations (see Figure 1).

The dose, displacements per atom (DPA), and surface loadings for the unattenuated primary proton beams are presented in Table 13 (for no shielding around the silicon except for the KEW shield). For the 50 MeV proton beam, no dose to the silicon is recorded because the kinetic energy weapon shield surrounding the spacecraft is thick enough to stop the incident beam. The results also show the dose due to the 200 MeV proton beam is smaller than the dose due to the 100 MeV proton beam. The primary reason for this effect is seen in the ionization energy loss curves for protons shown in Figure 21. In this figure, the average ionization energy loss (dE/dx) at 200 MeV is smaller than that at 100 MeV. Consequently less energy will be deposited in the silicon. Using these preliminary results and the fact that a directed particle beam of one amp contains 6.24×10^{18} protons/second (or 1.63×10^{14} protons/cm^2-sec), the dose rate in the silicon would be 1.23×10^7 rads/sec for the 200 MeV proton beam and 2.89×10^7 rads/sec for the 100-MeV proton beam. Therefore, if either one of these beams were on target for one second, the dose level in the electronics would be sufficient to cause device degradation and, in some types of devices, device failure. Both the DPA and surface loading levels are sufficiently high at one amp to indicate that damage can be expected.

To obtain the best shield material and configuration with respect to shield weight and to a given silicon dose, scoping studies were performed on several secondary radiation shielding materials. Initial calculations examined four materials, lead, iron, aluminum, and borated polyethylene, for the secondary shield. For the purpose of clarity, the kinetic energy weapon shield will be referred to as the primary shield, and the other shielding materials will be referred to as the secondary shield. These four materials were chosen because they represent some of the basic building blocks used in shield design and they encompass a wide range of material densities. The initial spacecraft geometry was the same as that used in the preliminary analysis above and consisted of the silicon plus primary shield. For the purpose of the scoping studies, the secondary shield material was placed around the silicon. This configuration would minimize the secondary shield weight. Based on the preliminary analysis results presented above, the initial studies employed

Table 12

Dose and Displacements Per Atom Due to
Various Temperature Black Body X-Ray Emitters

Temperature (KeV)	Number of X-Rays[a] (X-rays/kiloton)	Silicon Dose[b] (rads m^2/kiloton)	DPA[b,c] (DPA m^2/kiloton)		Aluminum Dose[b,c] (rads m^2/kiloton)
			$e^{\pm}$	γ	
1	7.37+27[d]	0.0	0.0	0.0	2.93+12
2	3.64+27	8.45+02	0.0	0.0	2.88+12
5	1.45+27	2.19+08	0.0	0.0	2.35+12
10	7.26+26	6.37+09	3.68−12	2.70−12	1.32+12
15	4.84+26	2.16+10	6.47−10	5.78−10	7.86+11
20	3.63+26	4.68+10	6.48−09	8.32−09	5.08+11
25	2.90+26	3.50+10	2.33−08	2.58−08	3.57+11

[a] Assumes 75% of the energy emission in terms of black body radiation. (10^{12} calories/kiloton).

[b] Data have already been divided by 4π and should be divided only by $R^2(m^2)$.

[c] KEW shield only.

[d] Read as 7.37×10^{27}

Table 13

Dose, Displacements Per Atom and Surface Loadings
Due to Directed Proton Beam Weapons[a]

Proton Energy (MeV)	Rads/sec $\frac{}{p/\text{cm}^2 \cdot \text{sec}}$	DPA/sec $\frac{}{p/\text{cm}^2 \cdot \text{sec}}$	Calories/cm^2 · sec $\frac{}{p/(\text{cm}^2 \cdot \text{sec})^b}$
50.	0.0	0.0	1.91−12[c]
100.	1.77−7	1.18−20	3.83−12
200.	7.55−8	3.61−21	7.66−12

[a]The results are for unattenuated primary protons only and for KEW shield only.
[b]Surface loading on the projected area of the spacecraft ($\pi(110.55\text{cm})^2$).
[c]Read as 1.91×10^{-12}.

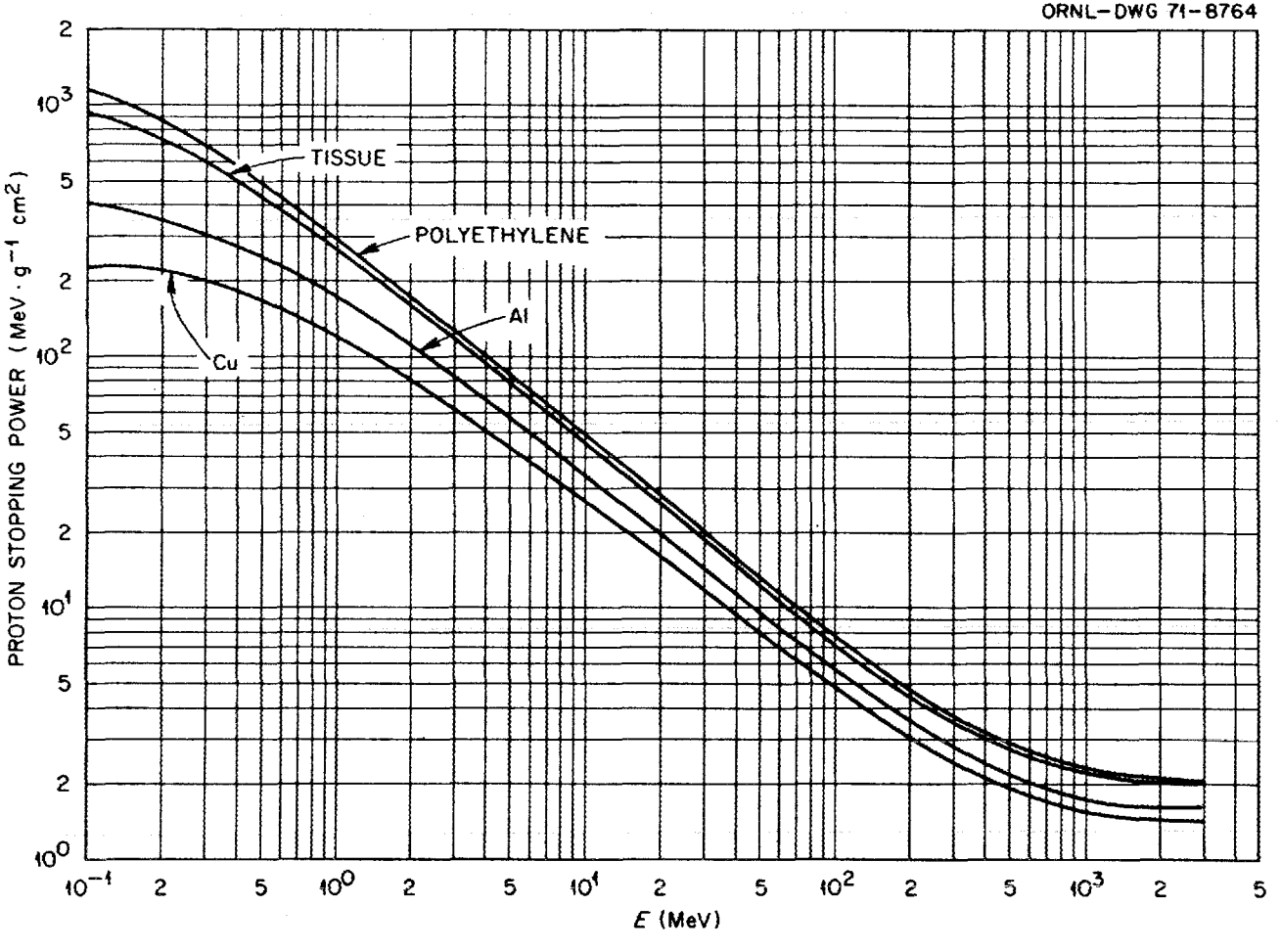

Figure 21. Proton stopping power vs. energy in various materials.

the 200 MeV and 100 MeV proton directed energy beams incident on the kinetic energy weapon shield. The source was modeled as a plane wave source incident on the surface of the sphere. The scoping study calculations modeled only a single material (no composite shield) and analyzed the dose to the silicon as a function of secondary shield thickness. All calculations included the primary shield and analyzed the dose for the unattenuated primary proton beam.

The results for the unattenuated 200 MeV proton directed energy beam weapon are presented in Table 14 for the base case (primary shield only) and the cases with various thicknesses of secondary shield material. In Table 14, the gram thickness is for the secondary shield only and does not include the primary shield. The results in Table 14 show the dose to the silicon increasing as a function of secondary shield thickness and then decreasing rapidly. This behavior is exhibited by all four secondary shield materials and is due to the average ionization energy loss (dE/dx) for the materials. As more secondary shield material is added, the primary protons lose more energy through multiple scattering and electron excitation and ionization. At lower energies, the average ionization energy loss (dE/dx) is larger (see Figure 21) and therefore more proton energy is deposited in the silicon. Eventually, enough secondary shield material is placed around the silicon such that the energy loss due to multiple scattering and electron excitation and ionization outweighs the larger ionization energy loss (dE/dx) in the silicon obtained at lower energies. At this point, the dose in the silicon begins to decrease rapidly as the primary particles are stopped in the shielding material.

A similar sequence of calculations was performed for the unattenuated 100 MeV proton directed energy beam weapon incident on the spacecraft. These results are presented in Table 15 and show a rapid decrease in the silicon dose as a function of increasing secondary shield thickness. The increase in the silicon dose depicted in the 200 MeV proton directed energy beam results is not exhibited here because the proton energy loss due to multiple scattering and electron excitation and ionization in the shielding material outweighs the larger ionization energy loss in the silicon (dE/dx) obtained at lower energies. Therefore less energy is deposited in the silicon. A graphical representation of the silicon dose as a function of secondary shield thickness is given in Figure 22 for the unattenuated 200 MeV proton directed energy beam weapon and in Figure 23 for the unattenuated 100 MeV proton directed energy beam weapon. These curves were obtained using cubic spline fits to the calculational results. For a given gram/cm^2 thickness of secondary shield material (or one of similar density), a reasonable estimate of the silicon dose can be obtained from these curves.

To study the effects of secondary particles produced from nuclear and electromagnetic collisions of the proton beam, some of the cases were analyzed to include the transport of all primary and secondary collision products. In particular, the contributions to the silicon dose from primary and secondary protons, heavy ion recoils (A>1), photons produced via high energy interactions, low energy

Table 14

Silicon Dose due to an Unattenuated 200 MeV Hydrogen
Directed Energy Beam Weapon Incident on the
Spacecraft Kinetic Energy Weapon Shield

Gram Thickness	KEW Shield	Silicon Dose (Rads(Si)/proton/cm^2) Lead Shield	Iron Shield	Aluminum Shield	Borated Poly Shield
0[a]	7.554-8[b]				
5		8.124-8	8.305-8	8.341-8	8.458-8
10		8.699-8	9.130-8	9.203-8	1.018-7
15		9.160-8	1.052-7	1.100-7	1.537-7
20		1.033-7	1.344-7	1.617-7	1.244-7
25		1.190-7	1.756-7	1.480-7	0.0
30		1.583-7	7.877-8	2.734-9	
35		1.732-7	0.0	0.0	
40		1.080-7			
45		3.295-8			
50		0.0			

[a] gm/cm^2
[b] Read as 7.554×10^{-8}

Table 15

Silicon Dose due to an Unattenuated 100 MeV Hydrogen Directed Energy Beam Weapon Incident on the Spacecraft Kinetic Energy Weapon Shield

Gram Thickness[a]	KEW Shield	Silicon Dose (Rads(Si)/proton/cm^2) Lead Shield	Iron Shield	Aluminum Shield	Borated Poly Shield
0	1.768-7[b]				
1.25		1.708-7	1.692-7	1.660-7	1.609-7
2.5		1.626-7	1.474-7	1.458-7	1.288-7
5.0		1.222-7	7.954-8	6.904-8	4.708-10
7.5		7.222-8	3.555-9	0.0	0.0
10.0		1.998-8	0.0		
12.5		0.0			

[a] gm/cm^2

[b] Read as 1.768×10^{-7}

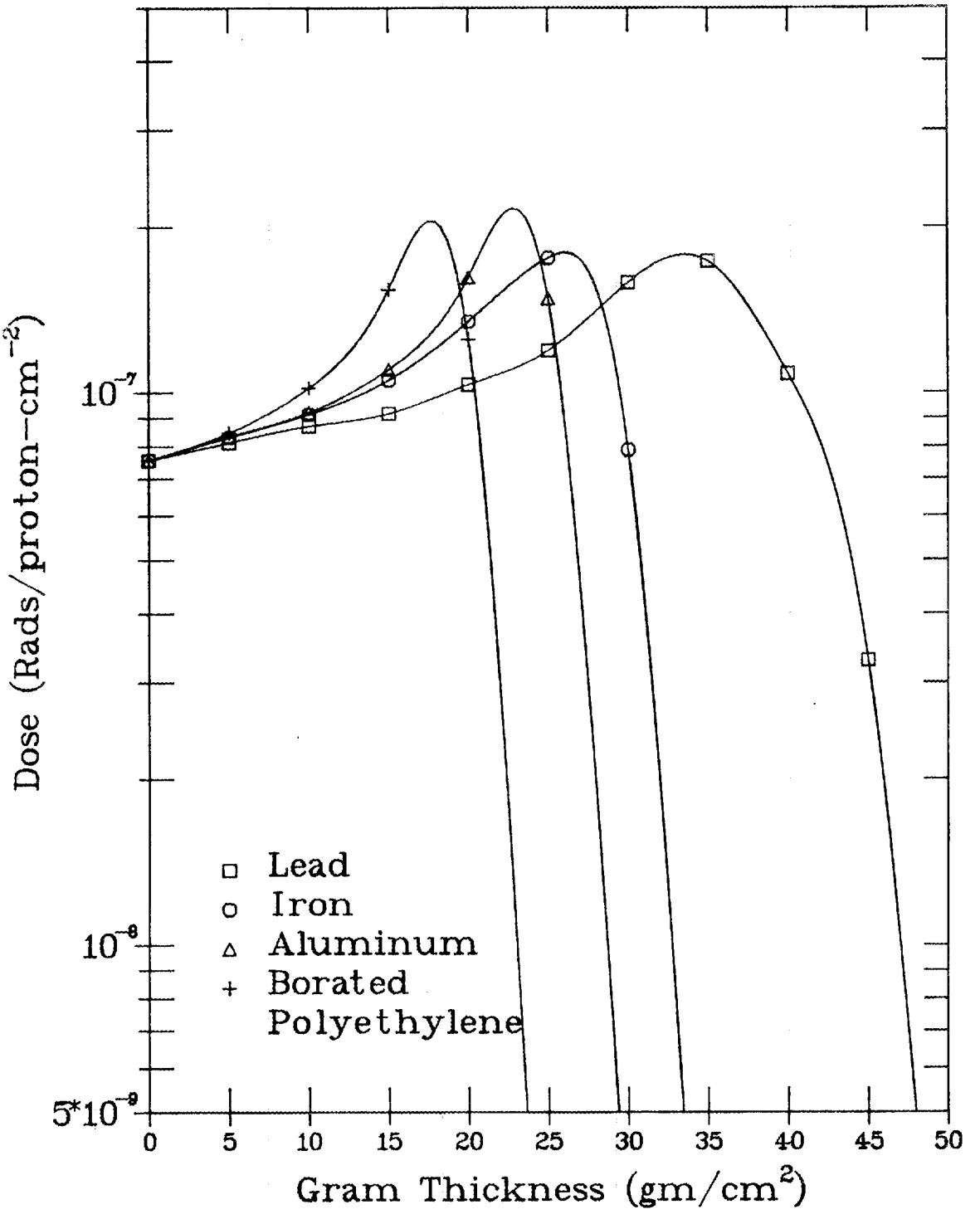

Figure 22. Silicon dose vs. secondary shield thickness for various shield materials and 200 MeV directed hydrogen beam (primary proton ionization only).

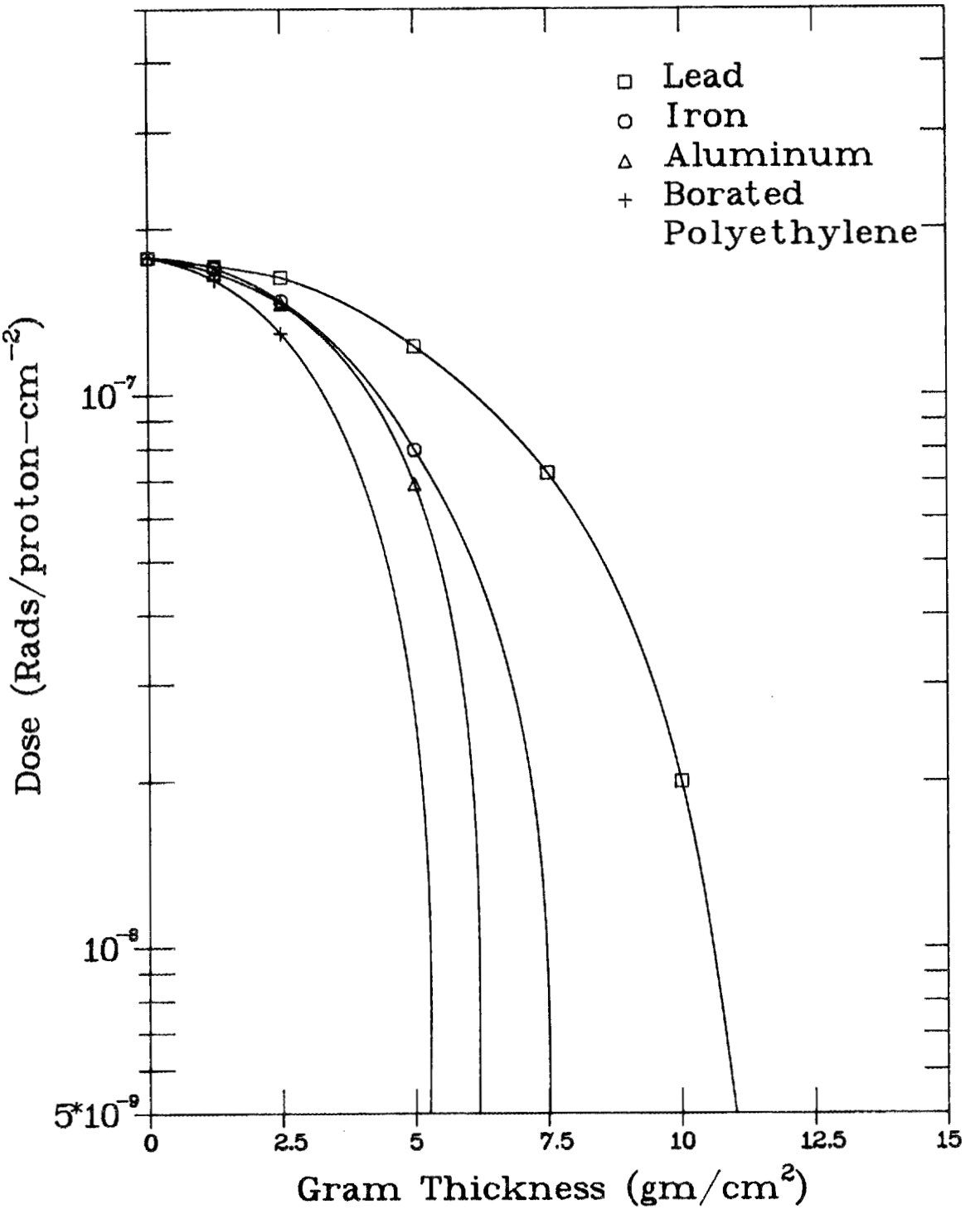

Figure 23. Silicon dose vs. secondary shield thickness for various shield materials and 100 MeV directed hydrogen beam (primary proton ionization only).

neutron collisions, and photons produced via low energy neutron interactions were considered. The High Energy Transport Code HETC[5] was used to transport the high energy protons and secondary particles, the Monte Carlo Ionization Chamber Analysis Package MICAP[10] was used to transport the low energy neutrons (E<20 MeV) produced during the HETC analysis, and the electron and gamma-ray shower code EGS[7] was used to transport the photons. The MORSE code system[8] was also used to transport the low energy neutrons and photons resulting from low energy neutron interactions. The 200 MeV proton directed energy beam was chosen as the source for this study, and the primary shield only and secondary shields of 10-, 20-, and 30-gram thicknesses were chosen for analysis. The results from these calculations are presented in Tables 16 through 28. The results in these tables show several trends with respect to the major contributors to the silicon dose. In all cases where the primary proton beam has not been sufficiently absorbed, the primary and secondary protons contribute over 75% of the dose to the silicon. The second major contributor is due to photons produced via high energy (E>20 MeV) interactions. The energy spectra and multiplicity of these gamma rays are not at all well known and additional research in this area may be needed. All other contributors are insignificant with respect to the silicon dose. (The 30 gram/cm^2 aluminum secondary shield (Table 25) and the 30 gram/cm^2 borated polyethylene shield (Table 28) attenuate the proton beam significantly and therefore do not exhibit the above trends.) The statistics on the results for the primary contributors mentioned above are less than 10% for the primary and secondary protons and less than 25% for the photons produced via high energy interactions. The statistical error on the results for the other contributors are all greater than 50% and therefore these results can only be used to show how insignificant these contributors are to the total silicon dose and cannot be used to obtain an absolute value for their contribution. It should be noted, however, that while these contributors are insignificant to silicon dose, they may be large contributors to other mechanisms of silicon damage and electronic component failure i.e., DPA, etc. Finally, a comparison of the total silicon dose from the unattenuated 200 MeV proton beam and from the 200 MeV proton beam with nuclear and electromagnetic collisions is presented in Table 29 for the primary shield only and the 10, 20, and 30 gram/cm^2 thicknesses of the secondary shield materials. The results in Table 29 show that for the primary shield only, the total dose to the silicon increased approximately 33% when all contributors were included. When secondary shielding was added, the increase in the total silicon dose was less than 15% for all secondary shield materials when all contributors were included. Furthermore, as the secondary shield thickness increases, the total silicon dose decreases and eventually will be less than the dose due to primary radiation only (for the same secondary shield thickness).

The above scoping calculations modeled only a single material (no composite shield) and analyzed the dose to the silicon as a function of the secondary shield thickness. A final calculation incorporated a composite shield (2.6 cm lead +

Table 16

Individual Contributions to the Silicon Dose When Primary and Secondary Collisions and Particle Transport are Considered: 200-MeV Directed Hydrogen Beam Incident Upon Kinetic Energy Weapon (KEW) Shield

Contributors	Rads/sec / $p/cm^2 \cdot sec$	Percent of Total
Primary protons	7.00-8[a]	69.3
Secondary protons	6.19-9	6.1
Heavy ion recoils (A>1)	5.71-10	0.6
Photons H[b]	2.39-8	23.7
Neutrons ($E_{neutron} < 20$ MeV)	1.64-11[d] (8.43-12)[e]	0.016 (0.008)
Photons L[c]	2.09-12[d] (5.46-13)[e]	0.002 (0.001)
Total	1.01-7	

[a] Read as 7.00×10^{-8}

[b] Photons produced by particle collisions in HETC.

[c] Photons produced by neutron collisions for $E_{neutron} < 20$ MeV.

[d] Values are from MORSE analysis.

[e] Values in parentheses are from MICAP analysis.

Table 17

Individual Contributions to the Silicon Dose When Primary and Secondary Collisions and Particle Transport are Considered: 200-MeV Directed Hydrogen Beam Incident Upon KEW + 10 gm/cm^2 Thickness Lead Shield

Contributors	$\frac{\text{Rads/sec}}{\text{p}/cm^2 \cdot \text{sec}}$	Percent of Total
Primary protons	7.61-8[a]	82.3
Secondary protons	7.22-9	7.8
Heavy ion recoils (A>1)	4.50-10	0.5
Photons H[b]	8.71-9	9.4
Neutrons ($E_{neutron} < 20$ MeV)	4.34-11[d] (4.24-11)[e]	0.047 (0.046)
Photons L[c]	1.04-11[d] (1.13-11)[e]	0.011 (0.012)
Total	9.25-8	

[a] Read as 7.61×10^{-8}

[b] Photons produced by particle collisions in HETC.

[c] Photons produced by neutron collisions for $E_{neutron} < 20$ MeV.

[d] Values are from MORSE analysis.

[e] Values in parentheses are from MICAP analysis.

Table 18

Individual Contributions to the Silicon Dose When Primary and Secondary Collisions and Particle Transport are Considered: 200-MeV Directed Hydrogen Beam Incident Upon KEW + 20 gm/cm^2 Thickness Lead Shield

Contributors	$\frac{\text{Rads/sec}}{\text{p}/cm^2 \cdot \text{sec}}$	Percent of Total
Primary protons	8.73-8[a]	80.8
Secondary protons	7.24-9	6.7
Heavy ion recoils (A>1)	4.13-10	0.4
Photons H[b]	1.30-8	12.0
Neutrons ($E_{neutron} < 20$ MeV)	4.49-11[d] (3.67-11)[e]	0.042 (0.034)
Photons L[c]	1.17-11[d] (1.25-11)[e]	0.011 (0.012)
Total	1.08-7	

[a] Read as 8.73×10^{-8}

[b] Photons produced by particle collisions in HETC.

[c] Photons produced by neutron collisions for $E_{neutron} < 20$ MeV.

[d] Values are from MORSE analysis.

[e] Values in parentheses are from MICAP analysis.

Table 19

Individual Contributions to the Silicon Dose When Primary and Secondary Collisions and Particle Transport are Considered: 200-MeV Directed Hydrogen Beam Incident Upon KEW + 30 gm/cm^2 Thickness Lead Shield

Contributors	Rads/sec / p/$cm^2 \cdot$ sec	Percent of Total
Primary protons	1.27-7[a]	78.9
Secondary protons	5.75-9	3.6
Heavy ion recoils (A>1)	3.37-10	0.2
Photons H[b]	2.74-8	17.0
Neutrons ($E_{neutron} < 20$ MeV)	3.99-11[d] (3.01-11)[e]	0.025 (0.019)
Photons L[c]	1.95-11[d] (1.15-11)[e]	0.012 (0.007)
Total	1.61-7	

[a] Read as 1.27×10^{-7}

[b] Photons produced by particle collisions in HETC.

[c] Photons produced by neutron collisions for $E_{neutron} < 20$ MeV.

[d] Values are from MORSE analysis.

[e] Values in parentheses are from MICAP analysis.

Table 20

Individual Contributions to the Silicon Dose When Primary and Secondary Collisions and Particle Transport are Considered: 200-MeV Directed Hydrogen Beam Incident Upon KEW + 10 gm/cm^2 Thickness Iron Shield

Contributors	Rads/sec / p/$cm^2 \cdot$ sec	Percent of Total
Primary protons	7.95-8[a]	75.7
Secondary protons	8.13-9	7.7
Heavy ion recoils (A>1)	4.53-10	0.4
Photons H[b]	1.71-8	16.3
Neutrons ($E_{neutron} < 20$ MeV)	3.02-11[d] (3.29-11)[e]	0.029 (0.031)
Photons L[c]	1.09-11[d] (1.40-11)[e]	0.010 (0.013)
Total	1.05-7	

[a] Read as 7.95×10^{-8}

[b] Photons produced by particle collisions in HETC.

[c] Photons produced by neutron collisions for $E_{neutron} < 20$ MeV.

[d] Values are from MORSE analysis.

[e] Values in parentheses are from MICAP analysis.

Table 21

Individual Contributions to the Silicon Dose When Primary and Secondary Collisions and Particle Transport are Considered: 200-MeV Directed Hydrogen Beam Incident Upon KEW + 20 gm/cm^2 Thickness Iron Shield

Contributors	$\frac{\text{Rads/sec}}{\text{p}/cm^2 \cdot \text{sec}}$	Percent of Total
Primary protons	1.09-7[a]	80.1
Secondary protons	8.13-9	6.0
Heavy ion recoils (A>1)	3.34-10	0.2
Photons H[b]	1.80-8	13.2
Neutrons ($E_{neutron} < 20$ MeV)	2.91-11[d] (2.36-11)[e]	0.021 (0.017)
Photons L[c]	1.31-11[d] (1.85-11)[e]	0.010 (0.014)
Total	1.36-7	

[a] Read as 1.09×10^{-7}

[b] Photons produced by particle collisions in HETC.

[c] Photons produced by neutron collisions for $E_{neutron} < 20$ MeV.

[d] Values are from MORSE analysis.

[e] Values in parentheses are from MICAP analysis.

Table 22

Individual Contributions to the Silicon Dose When Primary and Secondary Collisions and Particle Transport are Considered: 200-MeV Directed Hydrogen Beam Incident Upon KEW + 30 gm/cm^2 Thickness Iron Shield

Contributors	$\frac{\text{Rads/sec}}{\text{p}/cm^2 \cdot \text{sec}}$	Percent of Total
Primary protons	5.83-8[a]	81.0
Secondary protons	9.71-10	1.3
Heavy ion recoils (A>1)	4.85-11	0.1
Photons H[b]	1.26-8	17.5
Neutrons ($E_{neutron} < 20$ MeV)	3.05-11[d] (2.08-11)[e]	0.042 (0.029)
Photons L[c]	3.88-11[d] (7.60-11)[e]	0.054 (0.01)
Total	7.20-8	

[a] Read as 5.83×10^{-8}

[b] Photons produced by particle collisions in HETC.

[c] Photons produced by neutron collisions for $E_{neutron} < 20$ MeV.

[d] Values are from MORSE analysis.

[e] Values in parentheses are from MICAP analysis.

Table 23

Individual Contributions to the Silicon Dose When Primary and Secondary Collisions and Particle Transport are Considered: 200-MeV Directed Hydrogen Beam Incident Upon KEW + 10 gm/cm^2 Thickness Aluminum Shield

Contributors	$\frac{\text{Rads/sec}}{\text{p}/cm^2 \cdot \text{sec}}$	Percent of Total
Primary protons	7.93-8[a]	78.5
Secondary protons	8.23-9	8.1
Heavy ion recoils (A>1)	4.27-10	0.4
Photons H[b]	1.33-8	13.2
Neutrons ($E_{neutron} < 20$ MeV)	2.35-11[d] (1.78-11)[e]	0.023 (0.018)
Photons L[c]	6.91-12[d] (7.60-11)[e]	0.007 (0.01)
Total	1.01-7	

[a] Read as 7.93×10^{-8}

[b] Photons produced by particle collisions in HETC.

[c] Photons produced by neutron collisions for $E_{neutron} < 20$ MeV.

[d] Values are from MORSE analysis.

[e] Values in parentheses are from MICAP analysis.

Table 24

Individual Contributions to the Silicon Dose When Primary and Secondary Collisions and Particle Transport are Considered: 200-MeV Directed Hydrogen Beam Incident Upon KEW + 20 gm/cm^2 Thickness Aluminum Shield

Contributors	$\frac{\text{Rads/sec}}{\text{p}/cm^2 \cdot \text{sec}}$	Percent of Total
Primary protons	1.23-7[a]	85.4
Secondary protons	7.12-9	4.9
Heavy ion recoils (A>1)	3.12-10	0.2
Photons H[b]	1.34-8	9.3
Neutrons ($E_{neutron} < 20$ MeV)	2.37-11[d] (1.53-11)[e]	0.016 (0.011)
Photons L[c]	1.01-10[d] (6.62-12)[e]	0.01 (0.005)
Total	1.44-7	

[a] Read as 1.23×10^{-7}

[b] Photons produced by particle collisions in HETC.

[c] Photons produced by neutron collisions for $E_{neutron} < 20$ MeV.

[d] Values are from MORSE analysis.

[e] Values in parentheses are from MICAP analysis.

Table 25

Individual Contributions to the Silicon Dose When Primary and Secondary Collisions and Particle Transport are Considered: 200-MeV Directed Hydrogen Beam Incident Upon KEW + 30 gm/cm^2 Thickness Aluminum Shield

Contributors	$\frac{\text{Rads/sec}}{\text{p}/cm^2 \cdot \text{sec}}$	Percent of Total
Primary protons	2.13-9[a]	14.4 (14.6)
Secondary protons	3.15-11	0.2
Heavy ion recoils (A>1)	3.67-12	0.025
Photons H[b]	1.24-8	83.8 (84.9)
Neutrons ($E_{neutron} < 20$ MeV)	2.15-10[d] (7.60-11)[e]	1.5 (0.5)
Photons L[c]	6.37-11[d] (7.67-12)[e]	0.4 (0.1)
Total	1.48-8 (1.46-8)	

[a] Read as 2.13×10^{-9}

[b] Photons produced by particle collisions in HETC.

[c] Photons produced by neutron collisions for $E_{neutron} < 20$ MeV.

[d] Values are from MORSE analysis.

[e] Values in parentheses are from MICAP analysis.

Table 26

Individual Contributions to the Silicon Dose When Primary and Secondary Collisions and Particle Transport are Considered: 200-MeV Directed Hydrogen Beam Incident Upon KEW + 10 gm/cm^2 Thickness Borated Poly Shield

Contributors	$\frac{\text{Rads/sec}}{\text{p}/cm^2 \cdot \text{sec}}$	Percent of Total
Primary protons	8.51-8[a]	79.5
Secondary protons	7.63-9	7.1
Heavy ion recoils (A>1)	3.86-10	0.4
Photons H[b]	1.41-8	13.2
Neutrons ($E_{neutron} < 20$ MeV)	1.72-11[d] (9.82-12)[e]	0.016 (0.009)
Photons L[c]	4.72-11[d] (1.43-12)[e]	0.044 (0.001)
Total	1.07-7	

[a] Read as 8.51×10^{-8}

[b] Photons produced by particle collisions in HETC.

[c] Photons produced by neutron collisions for $E_{neutron} < 20$ MeV.

[d] Values are from MORSE analysis.

[e] Values in parentheses are from MICAP analysis.

Table 27

Individual Contributions to the Silicon Dose When Primary and Secondary Collisions and Particle Transport are Considered: 200-MeV Directed Hydrogen Beam Incident Upon KEW + 20 gm/cm^2 Thickness Borated Poly Shield

Contributors	$\frac{\text{Rads/sec}}{\text{p}/cm^2 \cdot \text{sec}}$	Percent of Total
Primary protons	9.21-8[a]	87.3 (87.7)
Secondary protons	1.99-9	1.9
Heavy ion recoils (A>1)	5.75-11	0.1
Photons H[b]	1.12-8	10.6 (10.7)
Neutrons ($E_{neutron} < 20$ MeV)	9.91-12[d] (6.40-12)[e]	0.001 (0.006)
Photons L[c]	1.55-10[d] (3.32-12)[e]	0.1 (0.003)
Total	1.06-7 (1.05-7)	

[a] Read as 9.21×10^{-8}

[b] Photons produced by particle collisions in HETC.

[c] Photons produced by neutron collisions for $E_{neutron} < 20$ MeV.

[d] Values are from MORSE analysis.

[e] Values in parentheses are from MICAP analysis.

Table 28

Individual Contributions to the Silicon Dose When Primary and Secondary Collisions and Particle Transport are Considered: 200-MeV Directed Hydrogen Beam Incident Upon KEW + 30 gm/cm^2 Thickness Borated Poly Shield

Contributors	$\frac{\text{Rads/sec}}{\text{p}/cm^2 \cdot \text{sec}}$	Percent of Total
Primary protons	0.0	0.0
Secondary protons	6.00-13[a]	0.4 (1.1)
Heavy ion recoils (A>1)	1.88-13	0.1 (0.3)
Photons H[b]	5.36-11	38.0 (94.9)
Neutrons ($E_{neutron} < 20$ MeV)	2.52-12[d] (1.93-12)[e]	1.8 (3.4)
Photons L[c]	8.41-11[d] (1.84-13)[e]	59.6 (0.3)
Total	1.41-10 (5.65-11)	

[a] Read as 6.00×10^{-13}

[b] Photons produced by particle collisions in HETC.

[c] Photons produced by neutron collisions for $E_{neutron} < 20$ MeV.

[d] Values are from MORSE analysis.

[e] Values in parentheses are from MICAP analysis.

Table 29

Comparison of the Silicon Dose Due to a 200 MeV Hydrogen Directed Energy Beam Weapon Incident on the Spacecraft Kinetic Energy Weapon Shield

Shield Configuration	Silicon Dose (Rads/sec/proton/cm^2· sec)	
	Primary[a]	Primary & Secondary[b]
Kinetic Energy Weapon (KEW)	7.55-8[c]	1.01-7
KEW + 10 gm/cm^2 Pb	8.70-8	9.25-8
KEW + 20 gm/cm^2 Pb	1.03-7	1.08-7
KEW + 30 gm/cm^2 Pb	1.58-7	1.61-7
KEW + 10 gm/cm^2 Fe	9.13-8	1.05-7
KEW + 20 gm/cm^2 Fe	1.34-7	1.36-7
KEW + 30 gm/cm^2 Fe	7.88-8	7.20-8
KEW + 10 gm/cm^2 Al	9.20-8	1.01-7
KEW + 20 gm/cm^2 Al	1.62-7	1.44-7
KEW + 30 gm/cm^2 Al	2.73-9	1.46-8
KEW + 10 gm/cm^2 BP	1.02-7	1.07-7
KEW + 20 gm/cm^2 BP	1.25-7	1.05-7
KEW + 30 gm/cm^2 BP	0.0	5.65-11

[a] Dose due to unattenuated primary protons only.
[b] Dose due to primary and secondary collisions and complete particle transport.
[c] Read as 7.55×10^{-8}.

16.2 cm borated polyethylene) from the nuclear weapons studies (see Section 3.1) as a secondary shield and used the 200 MeV proton directed energy beam weapon incident on the spacecraft primary (KEW) shield as the source. Calculations were performed considering first the energy deposition from unattenuated primary protons and then the energy deposition when full transport of both primary and secondary particles is performed. The results of the analysis showed the dose rate to the silicon was zero for the unattenuated primary protons only. Therefore, the primary plus secondary shield was sufficient to stop the incident radiation. The results when both primary and secondary particles are transported yielded a total dose rate in the silicon of 1.49×10^{-10} rads/sec/proton/cm^2 · sec. This result represents approximately a factor of 10^3 decrease in the silicon dose received when only the KEW shield was used (see Table 29). The results for the case when full transport is considered are shown in Table 30. The major contributors to the silicon dose are the photons from high energy reactions and the low energy (E<20 MeV) neutrons generated in the secondary shield. It should be noted that the primary protons have been completely stopped and do not contribute to the dose. This dose level still yields a dose rate of 2.43×10^4 rads/sec/amp and consequently, temporary damage or data flow interrupt could occur if the spacecraft remained in a one amp proton beam for one second.

3.2. NATURAL RADIATION ENVIRONMENTS

This section describes the results of the calculations that have been carried out to determine the radiation damage in silicon due to the various natural radiation environments present in space. In particular, the radiation damage due to galactic cosmic rays, solar flare cosmic rays, and Van Allen belt radiation (protons and electrons) is presented for the source spectra and spacecraft geometry presented in Section 2.

3.2.1. Galactic Cosmic Rays

Galactic cosmic rays are composed predominately of protons (87%), and therefore only protons will be considered in calculating the silicon dose. For shielding and damage analysis purposes, the solar-minimum and solar-maximum cosmic ray flux spectra are used as upper and lower limits, respectively, on the particle flux that is encountered in space outside the earth's magnetosphere. The energy spectrum of the cosmic rays extends to high energy (E<200 GeV) but decreases rapidly with increasing energy. Furthermore, the angular distribution of the cosmic rays may be assumed isotropic outside the magnetosphere.

The dose, displacements per atom (DPA), and surface loadings for galactic minimum and maximum cosmic ray protons were calculated using the High Energy Transport Code HETC[5] and the source distribution given in Section 2. For these calculations, no attenuation of the proton beam was allowed. The results are

Table 30

Individual Contributions to the Dose When Primary and Secondary Collisions and Particle Transport are Considered: 200 MeV Directed Proton Beam Incident Upon KEW + 2.6 cm Lead + 16.2 cm Borated Polyethylene[a]

Contributors	$\frac{\text{Rads/sec}}{p/\text{cm}^2 \cdot \text{sec}}$	Percent of Total
Primary protons	0.0	0.0
Secondary protons	1.68−11[b]	11.3
Heavy ion recoils (A>1)	3.00−12	2.0
Photons H[c]	6.86−11	46.0
Neutrons ($E_{neutron} < 20$ MeV)	5.99−11	40.2
Photons L[d]	7.64−13	0.5
Total	1.49−10	

[a] 2.6 cm Lead = 29.51 gm/cm^2 ⇐
16.2 cm Borated Polyethylene = 16.20 gm/cm^2 ⇐
[b] Read as 1.68×10^{-11}.
[c] Photons produced by particle collisions in HETC.
[d] Photons produced by neutron collisions for $E_{neutron} < 20$ MeV.

HETC primaries only = 0.0 $\frac{\text{Rads/sec}}{p/\text{cm}^2 \cdot \text{sec}}$

presented in Table 31. Contributions from the galactic cosmic alpha particles and heavier nuclei were not considered in the preliminary analysis for reasons given above. The annual dose rate the spacecraft would receive varies from approximately 0.4 to 1.0 rads/year as the galactic cosmic proton flux intensity follows the 11-year cycle of solar activity. No anticipated damage to the electronics is expected to result from galactic cosmic protons. Furthermore, dose levels and damage due to other galactic particles are also expected to be substantially lower than the damage levels required to induce temporary or permanent device failure.

The results presented here are for the unattenuated primary galactic cosmic protons incident on the KEW shield. When more localized shielding is added around the sensitive electronic components, secondary particle-nuclear collisions will have to be considered if realistic dose levels are to be calculated.

3.2.2. Solar Flare Cosmic Rays

Solar flare cosmic rays are similar to galactic cosmic rays in composition, but are far less energetic with maximum energies extending only to approximately 3 GeV. The intensity, energy spectra, and angular distribution of solar flare particles vary widely from event to event and furthermore, exhibit a time dependence during an event. Typical values for the composition of a solar flare yield approximately 90% protons and 10% heavier nuclei particles, with alpha particles dominating the heavier nuclei particles. The duration of a solar flare is on the order of a day and therefore, for most shielding purposes, it is sufficient to consider only the time integrated effect of the solar flare. The angular distribution of the solar flare particles is highly anisotropic during the early stages of a solar flare. However, the angular distribution tends toward isotropy as the solar flare continues and is isotropic during most of the life of the solar flare.

Shielding and damage calculations for solar flare cosmic rays require consideration of several variables including number of solar flares, duration of each solar flare, and the rigidity of the solar flare. Rigidity is used to characterize the hardness of the solar flare energy spectra, with typical values varying between 50 and 200 MV and 10^6 to 10^9 particles/cm^2 being emitted with energy greater than 30 MeV. For the purposes of these shielding calculations, time-integrated solar flare energy spectra have been used in conjunction with an isotropic distribution of source particles. The calculations were performed on the spacecraft geometry shown in Figure 1 for the KEW shield only. The calculations were performed using three different values characterizing the rigidity of the incident source spectra and considered only unattenuated primary ionization energy deposition.

The dose, displacements per atom (DPA), and surface loadings for solar flare cosmic ray protons were calculated using the High Energy Transport Code HETC[5] and the source distribution given in Section 2. The results are presented in Table 32. Contributions from the solar flare cosmic alpha particles and heavier nuclei were not considered in the preliminary analysis. The annual dose rate the spacecraft would receive varies from approximately 85 to 300 rads/year assuming an average

Table 31

Dose, Displacements Per Atom, and Surface Loadings
Due to Galactic Solar Minimum and Maximum Protons[a]

Spectra	Rads/sec	DPA/sec	Calories/cm^2 · sec[b]
Solar Minimum	3.30−8[c]	7.00−22	9.88−11
Solar Maximum	1.14−8	1.23−22	7.25−11

[a]The results are for unattenuated primary protons only.
[b]Surface loading on the outside hull of the spacecraft due to galactic protons.
[c]Read as 3.30×10^{-8}.

of five flares per year. No anticipated damage to the electronics is expected to result from solar flare cosmic protons. Furthermore, dose levels and damage due to other solar flare particles are also expected to be substantially lower than the damage levels required to induce temporary or permanent device failure.

The results presented here are for the unattenuated primary solar flare cosmic protons incident on the KEW shield. When more localized shielding is added around the sensitive electronic components, secondary particle-nuclear collisions will have to be considered if more realistic dose levels are to be calculated.

3.2.3. Van Allen Belt Radiation

Van Allen belt radiation is primarily composed of protons and electrons trapped in the earth's magnetosphere. The proton energy spectra used in the analysis extend from 30 MeV to 1 GeV whereas the electron energy spectra only extend to approximately 5 MeV. The proton flux is not zero at energies less than 30 MeV, however, the thinnest shield considered will attenuate these particles. Also, the assumption of zero proton flux above 1 GeV is arbitrary. This assumption is made because of insufficient spectral data for the protons above this energy. The angular distributions for both types of Van Allen belt radiation are assumed to be isotropic due to lack of adequate data. This assumption may be insufficient for some spacecraft orbits and angles of inclination.

Shielding and damage calculations for Van Allen belt radiation require consideration of the spacecraft orbit and angle of inclination. For the Van Allen belt proton shielding calculations, circular orbits of 240 and 1500 nautical miles and spacecraft inclination angles of 0, 30, 60, and 90 degrees were chosen. This series of calculations encompass the minimum and maximum proton flux rates the spacecraft would encounter. For the Van Allen belt electron shielding calculations, only the circular orbit of 1500 nautical miles and a spacecraft inclination angle of 0 degrees was used. This spectrum represents the maximum electron flux rate the spacecraft would encounter. Due to the very short ranges of the low energy electrons, the majority of the dose in the electronics will result from secondary bremsstrahlung photons produced by the primary electrons.

The dose, displacements per atom (DPA), and surface loadings for the various Van Allen belt proton spectra are presented in Table 33. These results were obtained using HETC[5] and considered only the contribution from unattenuated primary ionization energy deposition. The calculations were performed on the spacecraft geometry shown in Figure 1 and used the source spectra presented in Section 2. The annual dose rate the spacecraft would receive varied from approximately 30 rads/year at 240 nautical miles and 90 degrees inclination to 43,500 rads/year at 1500 nautical miles and 0 degrees inclination for the KEW shield only. Therefore a spacecraft could survive the Van Allen belt proton radiation for approximately 20 years assuming 10^6 rads total dose are require for device failure and no self annealing occurs.

Table 32

Dose, Displacements Per Atom, and Surface Loadings
Due to Solar-Flare Protons[a,b]

Rigidity of Flare (MV)	Rads/Flare	DPA/Flare	Calories/cm^2/Flare[c]
50	1.67+1[d]	9.63−13	5.31−4
100	4.30+1	2.59−12	7.29−4
200	6.01+1	3.57−12	1.14−4

[a]The results are for unattenuated primary protons only.

[b]10^9 protons/cm^2/flare, normalization.

[c]Surface loading on the outside hull of the spacecraft due to solar flare of 10^9 protons/cm^2.

[d]Read as 1.67×10^1.

Table 33

Dose, Displacements Per Atom, and Surface Loadings
Due to Van Allen Belt Protons[a]

Spectra	Rads/day	DPA/day	Calories/cm^2/day[b]
1500m, 0°[c]	1.19+2[d]	6.98−12	2.20−3
1500m, 30°	4.53+1	2.60−12	8.87−4
1500m, 60°	2.73+1	1.60−12	4.83−4
1500m, 90°	2.24+1	1.30−12	4.08−4
240m, 30°	1.97−1	1.14−14	2.96−6
240m, 60°	9.20−2	5.49−15	1.31−6
240m, 90°	8.42−2	5.03−15	1.22−6

[a]The results are for unattenuated primary protons only.
[b]Surface loading on the outside hull of the spacecraft due to Van Allen belt spectra.
[c]1500 nautical miles and 0° orbital inclination.
[d]Read as 1.19×10^2.

As stated above, the results in Table 33 were obtained for the KEW shield only. To investigate the effect of additional local shielding around the electronics, the 1500 nautical mile and 0 degree angle of inclination proton spectrum was used. This spectrum yielded the maximum dose rate, DPA, and surface loading for the KEW shield results and therefore should yield the maximum results when a secondary shield around the electronics is considered. To investigate the effect of local shielding, the 2.6 cm thick lead and 16.2 cm thick borated polyethylene shield was placed around the silicon sphere. HETC calculations were performed to calculate the dose, DPA, and surface loadings for the spacecraft when all primary and secondary particle collisions are allowed. The electromagnetic and low energy neutron transport is accomplished using the Electron Gamma Shower Code EGS[7] and the Monte Carlo Ionization Chamber Analysis Package MICAP,[10] respectively.

The results for the spacecraft in the circular orbit at 1500 nautical miles with a 0° angle of inclination are presented in Table 34 for the KEW shield and unattenuated primaries only, the KEW + lead/borated polyethylene shield and unattenuated primaries only, and the KEW + lead/borated polyethylene shield with primaries and secondaries transported. In all three cases, the surface loading was the same (approximately 2.20×10^{-3} calories/cm^2/day) because it is dependent only on the incident proton spectrum. The results indicate a decrease in the annual dose rate by a factor of 6.7 when the lead/borated polyethylene shield is placed around the silicon and unattenuated primary protons are considered. When both primary and secondary particles are transported and the primary particles are allowed to undergo nuclear collisions, the dose rate decreases by a factor of 8.9 for the KEW + lead/borated polyethylene shield. Consequently, the radiation damage effects of Van Allen belt protons are reduced to a level which would not impair the operation of the spacecraft or restrict the expected lifetime of the spacecraft. A detailed analysis of the individual contributions to the dose when both primary and secondary particles are transported is shown in Table 35 for the KEW + lead/borated polyethylene shield. The results show that virtually all of the damage is coming from the primary protons and that the only other significant contributor to the dose is the secondary protons generated in nuclear collisions.

As stated above, the initial Van Allen belt electron analysis used the reference spacecraft geometry shown in Figure 1 and an electron differential flux spectrum at an orbital altitude of 1500 nautical miles with a spacecraft angle of inclination equal to 0° (see Section 2 for the source spectrum). Preliminary results from the analysis yielded low dose rates averaged over the 2 cm silicon sphere (approximately 0.4 rads/day) and high statistical error (approximately 70%). Further analysis proved these results insensitive to changes in the energy sampling or angular sampling probabilities. Furthermore, the results were significantly lower than the results presented in the AFWL report.[27] Therefore an attempt was made to recreate the AFWL results and to determine why there was such a large discrepancy between the two results.

Table 34

Dose and Displacements Per Atom Due to
Van Allen Belt Protons for a Circular Orbit
of 1500 Nautical Miles and 0° Angle of Inclination

Radiation Type Transported	Shield Configuration	Rads/day	DPA/day
Unattenuated Primaries	KEW	1.19+2[a]	6.98−12
Unattenuated Primaries	KEW + Pb/BP[b]	1.79+1	9.72−13
Primaries + Secondaries	KEW + Pb/BP[b]	1.34+1	9.10−13

[a]Read as 1.19×10^2.

[b]Pb/BP = 2.6 cm lead + 16.2 cm borated polyethylene.

Table 35

Individual Contributions to the Dose When Primary and Secondary Collisions and Particle Transport are Considered: Van Allen Belt Proton Spectra 1500m @ 0° Inclination KEW + 2.6 cm Lead + 16.2 cm Borated Polyethylene

Contributors	Rads/day $p/cm^2 \cdot sec$	Percent of Total
Primary protons	1.15+01[a]	86.1
Secondary protons	1.81+00	13.6
Heavy ion recoils (A>1)	3.81−02	0.3
Photons H[b]	2.66−02	0.02
Neutrons ($E_{neutron}$ <20MeV)	1.44−02	0.01
Photons L[c]	1.11−02	0.008
Total	1.34+01	

[a]Read as 1.15×10^1.

[b]Photons produced by particle collisions in HETC.

[c]Photons produced by neutron collisions for $E_{neutron} < 20MeV$.

To recreate the AFWL results, a semi-infinite aluminum slab 0.254 cm thick followed by a silicon slab 2.0 cm thick was modeled. The energy deposition in an interval volume next to the aluminum was calculated for various thicknesses of silicon ranging from 2.0 cm to 0.025 cm. The Van Allen belt electron source was located on the aluminum side away from the silicon. The results of the calculations are presented in Table 36 and show that the dose rate in the silicon initially increases and then decreases as the silicon thickness continuously decreases. A 0.035 thickness of silicon yielded the maximum dose rate of approximately 50.0 rads/day which is comparable to the 54.0 rads/day reported in the AFWL report for the same electron source spectrum. Consequently, the results indicate the damage that can be induced by Van Allen belt electrons is restricted to a surface effect and is primarily produced by soft photons. An unshielded spacecraft would receive dose rates on the order of 10^2 to 10^5 rads/year on the surface. A very thin shield, however, will completely mitigate the damage which could be induced by the Van Allen belt electrons. Therefore, shielding for other more substantial threats will take care of all Van Allen belt electron shielding requirements.

3.3. OPTIMIZATION CALCULATIONS

In this section, the steps taken to determine the optimal radiation shield for the spacecraft, and the results thereof will be discussed. The radiation shield configuration and materials were optimized relative to two typical nuclear weapon source terms, representing thermonuclear and fission devices. The major focus was on the thermonuclear source, as this was considered not only the most probable threat, but also gave rise to the largest doses. These source terms are fully described in Section 2.

Three computer codes were used in this analysis effort. AXMIX was employed to generate the cross section tables for the shield materials. Reference doses were calculated by ANISN and the optimization effort was performed by the code ASOP.[12] Code descriptions are provided in Section 2.

Calculations in this study have been done in one dimensional spherical geometry. The spacecraft is modeled by a silicon sphere of radius 2 cm, inside an as yet unspecified radiation shield, and a KEW shield at a radius of 100 cm. Geometry and material specifications can also be found in Section 2.

3.3.1. Material Scoping Studies

Initially, a composite radiation shield composed of lead, borated polyethylene, and iron was envisioned. An outer layer of iron would reduce the energy of the 14 MeV source neutrons to improve the neutron absorption of the borated polyethylene. The innermost layer of lead would attenuate the primary and secondary gamma rays incident upon the silicon target.

Table 36

Dose to Silicon Behind a Semi-Infinite Aluminum Slab[a]
for the Van Allen Belt Electron Spectrum at
1500 Nautical Miles and 0° Angle of Inclination

Silicon Thickness (cm)	Dose (rads/day)
2.0	0.4
0.4	8.1
0.2	17.4
0.1	33.0
0.075	39.1
0.050	42.7
0.035	49.2
0.025	33.3

[a]Thickness = 0.254 cm

Dose versus gram-thickness calculations were performed with the thermonuclear source for both iron and borated polyethylene to assess the validity of the outer iron component of the radiation shield. These calculations clearly indicate the superiority of the borated polyethylene in reducing the dose to the silicon target (see Figures 24 and 25). Therefore, iron was eliminated from consideration in the shield design.

Although the borated polyethylene was effective in reducing the neutron dose, the neutron absorption reaction causes an increase in the gamma dose due to production of secondary gamma rays

$$B^{10} + n \rightarrow Li^{7} + \alpha + \gamma.$$

This secondary gamma production limits the effectiveness of borated polyethylene as a radiation shield and necessitated a search for other potential shield materials. This led to lithium hydride as a component of the radiation shield. Although lithium-6 has a lower absorption cross section than boron-10 (941 barns vs. 3838 barns),[39] it has a much higher number density and does not contribute to the gamma dose through secondary gamma ray production. In addition, the density of lithium hydride is less than that of borated polyethylene. Calculations of dose versus gram-thickness were also made for lithium hydride (see Figure 26). Note that both constituents of dose, neutron and gamma, were reduced by the lithium hydride.

Scoping studies were also performed with the fission source. Lead, borated polyethylene, and lithium hydride were compared using this source term. The gamma component of the fission source is significantly larger than the neutron fraction and this fact is reflected in the scoping study results. The lead provides good attenuation of the gamma rays and a large reduction in total dose (Figure 27), while the borated polyethylene actually increases the total dose due to the secondary gamma production (Figure 28). The lithium hydride is superior to the borated polyethylene with a dose reduction of $\approx 30\%$ after 25 gram-thicknesses (Figure 29). The conclusion from this is the importance of the lead and the insignificance of the neutron shielding materials relative to a fission source. However, different devices can produce different neutron and gamma yields and therefore a wide range of devices should be studied in a final analysis.

3.3.2. Shield Optimization a.

Radiation shields made of Pb/LiH and Pb/borated polyethylene (B.P.) were optimized by weight using ASOP. For this study, cross sections and response functions from DLC31[13] were utilized and both source terms examined. Total neutron and gamma kermas were chosen. Results for dose attenuations of 33%, 50%, 67%, and 75% are listed below in Table 37 and plotted in Figures 30 and 31 for the thermonuclear source term. Fission results for dose attenuations of 33%, 50%, 67%, and 90% are compiled in Table 38 and plotted in Figures 32 and 33.

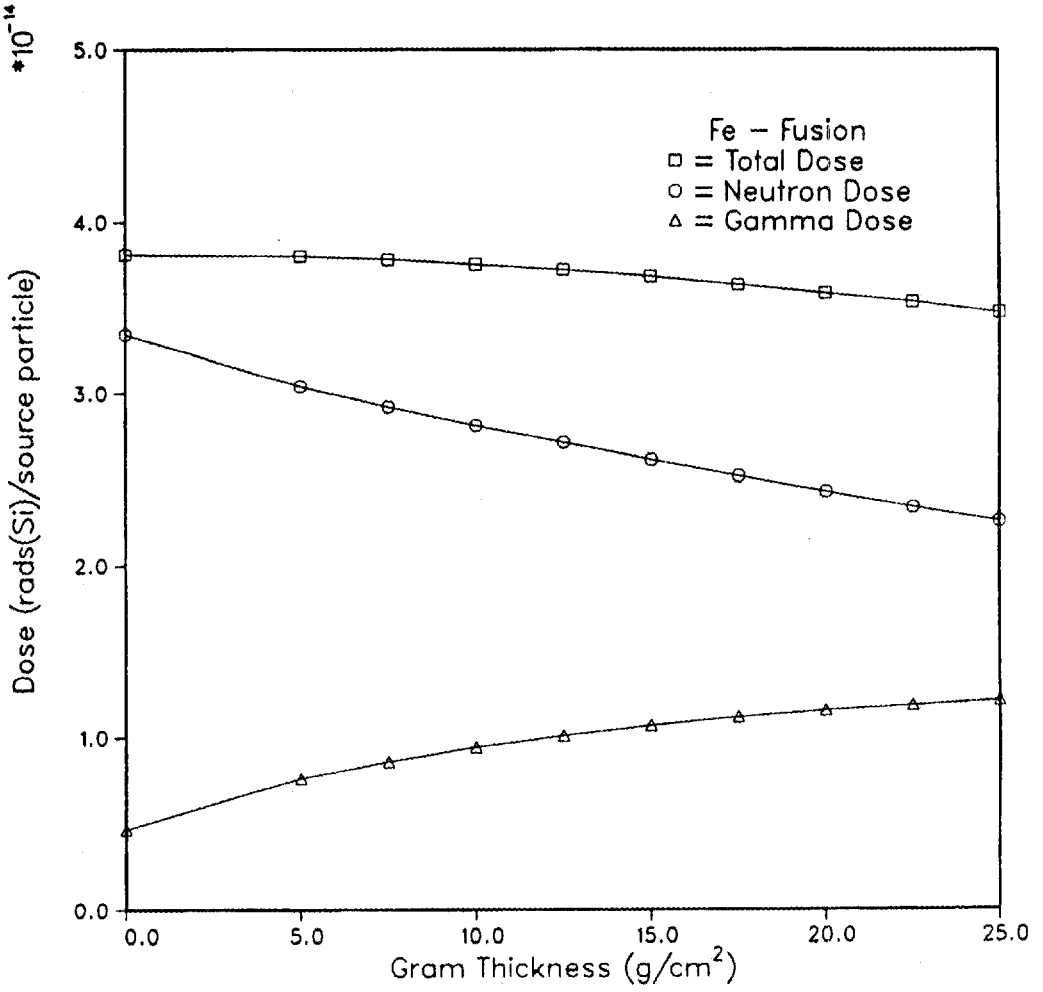

Figure 24. Dose vs. gram-thickness (g/cm^2) for iron, thermonuclear source.

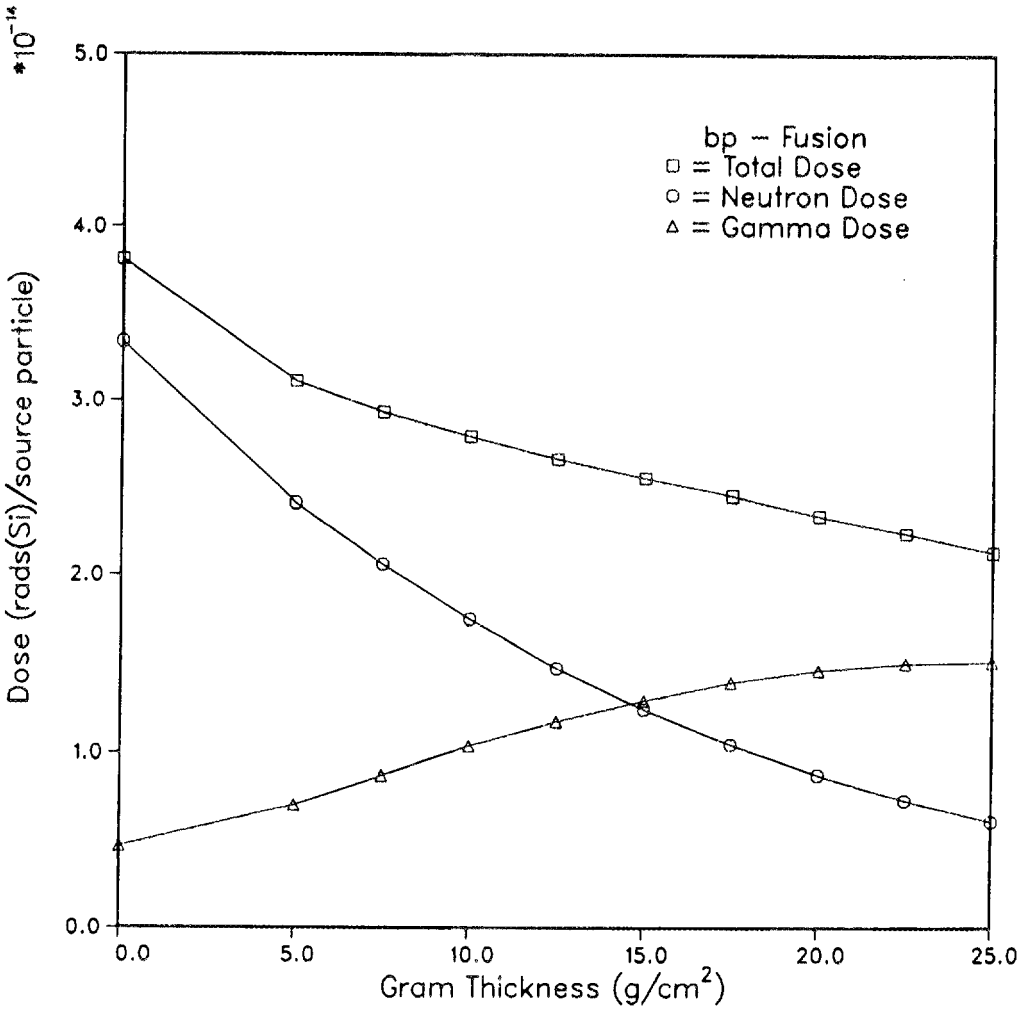

Figure 25. Dose vs. gram-thickness (g/cm^2) for borated polyethylene, thermonuclear source.

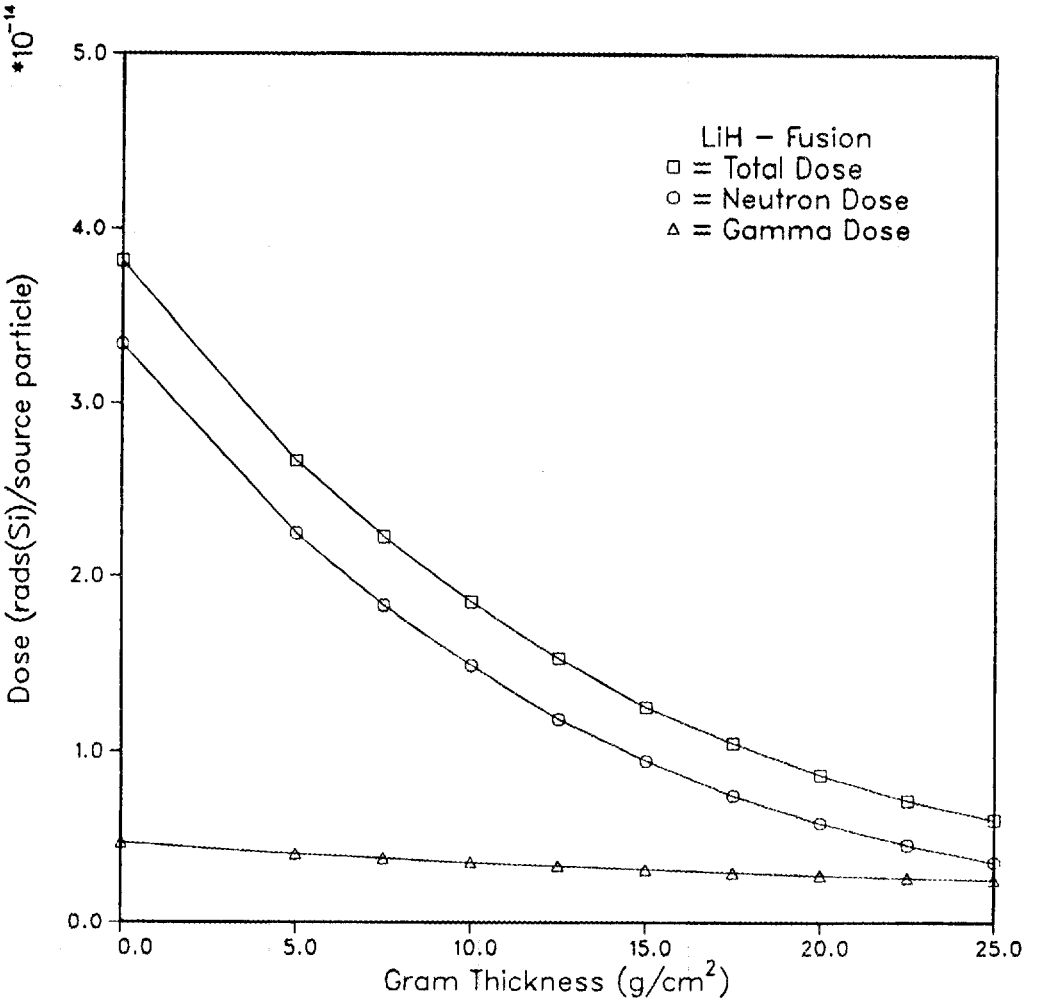

Figure 26. Dose vs. gram-thickness (g/cm^2) for lithium hydride, thermonuclear source.

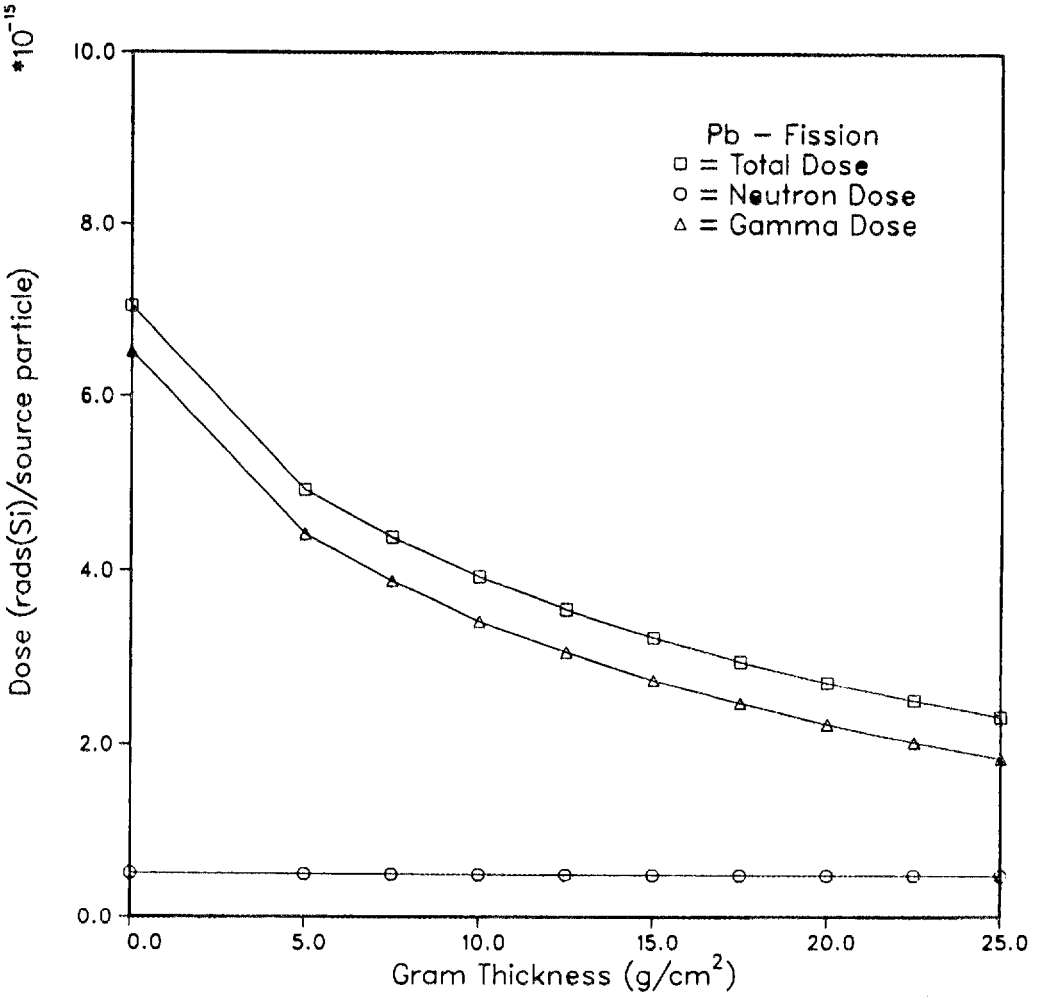

Figure 27. Dose vs. gram-thickness (g/cm^2) for lead, fission source.

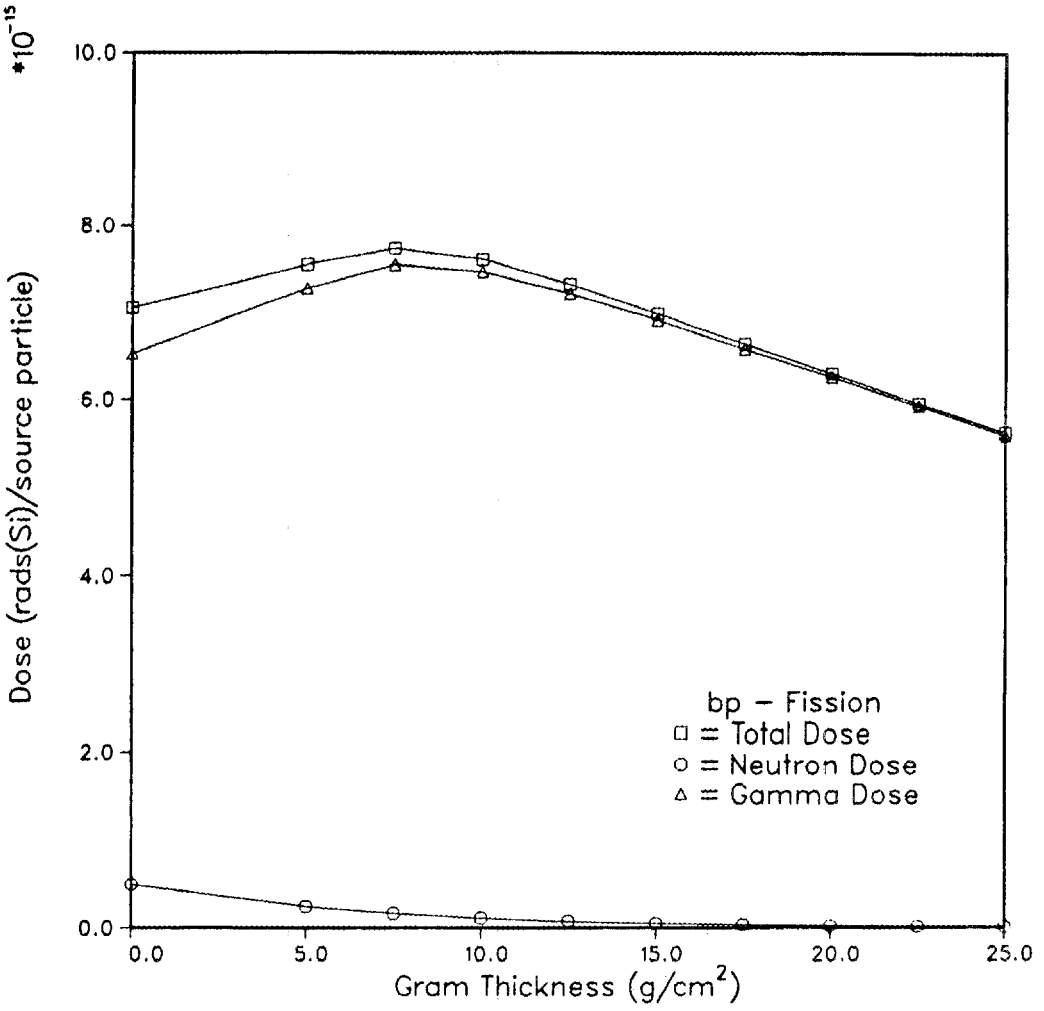

Figure 28. Dose vs. gram-thickness (g/cm^2) for borated polyethylene, fission source.

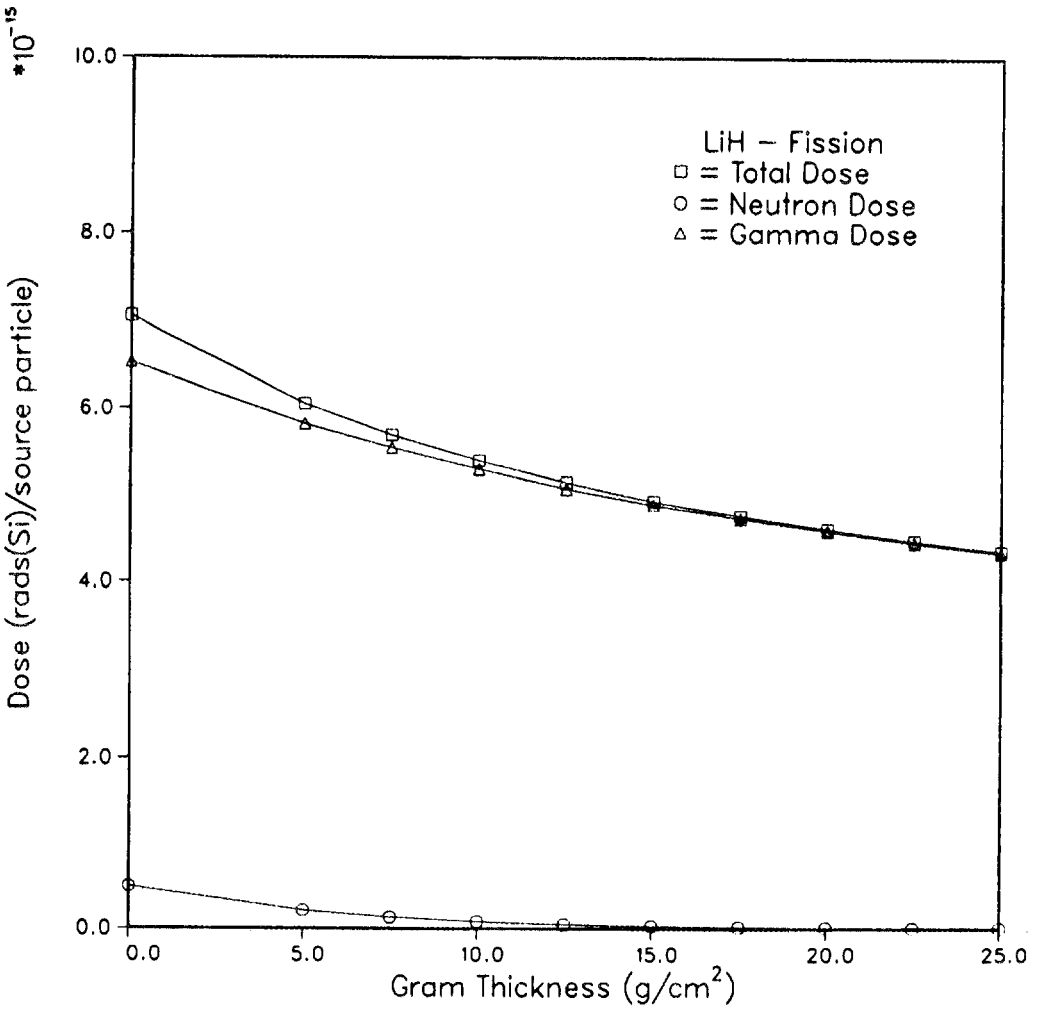

Figure 29. Dose vs. gram-thickness (g/cm^2) for lithium hydride, fission source.

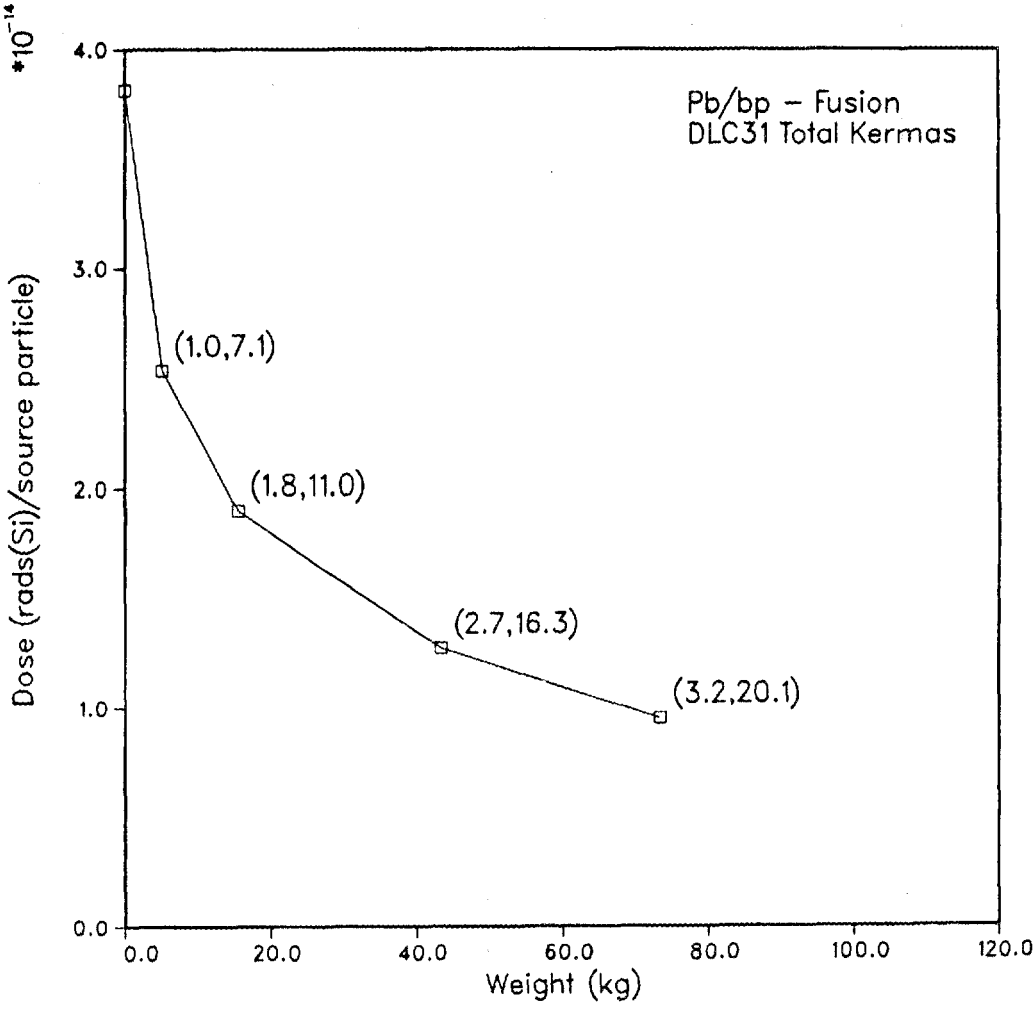

Figure 30. Dose vs. weight for a composite lead and borated polyethylene radiation shield and thermonuclear source. Numbers in parentheses represent shield thicknesses in cm for lead and borated polyethylene, respectively.

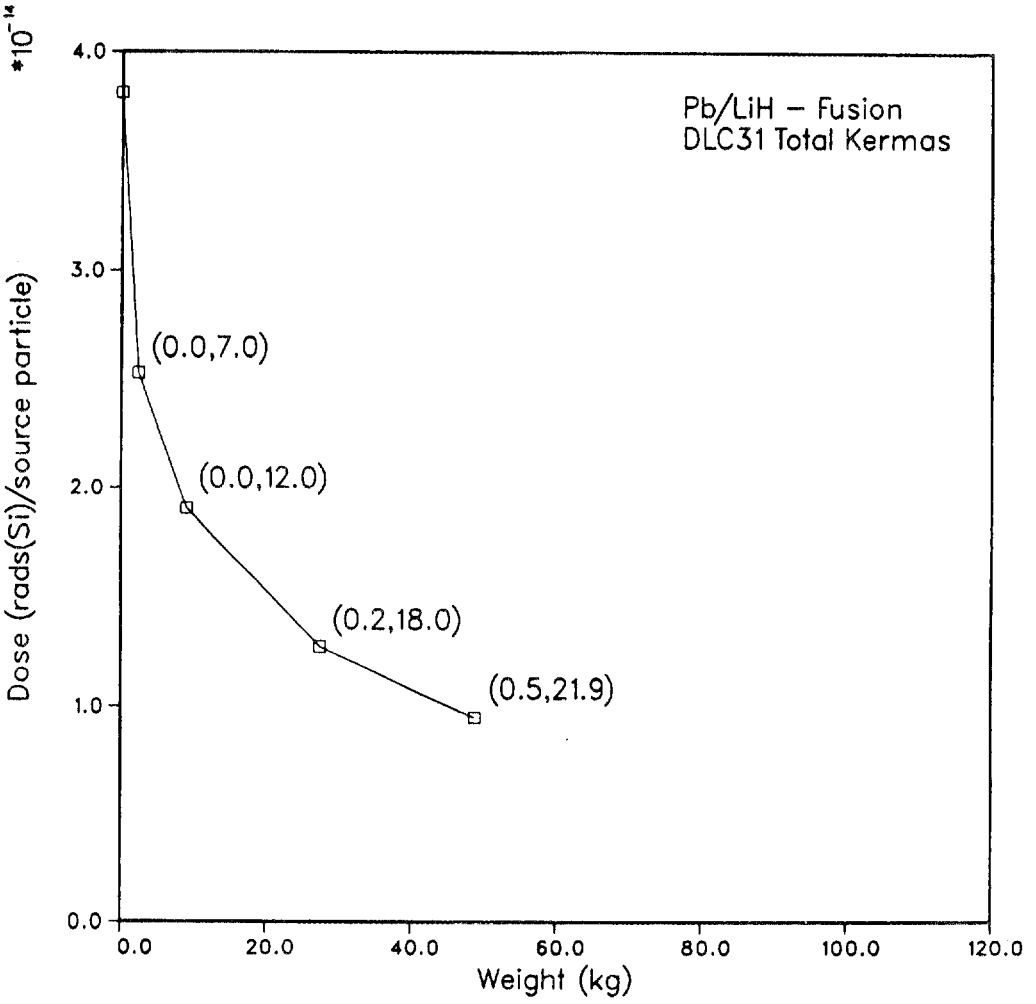

Figure 31. Dose vs. weight for a composite lead and lithium hydride radiation shield and thermonuclear source. Numbers in parentheses represent shield thicknesses in cm for lead and lithium hydride, respectively.

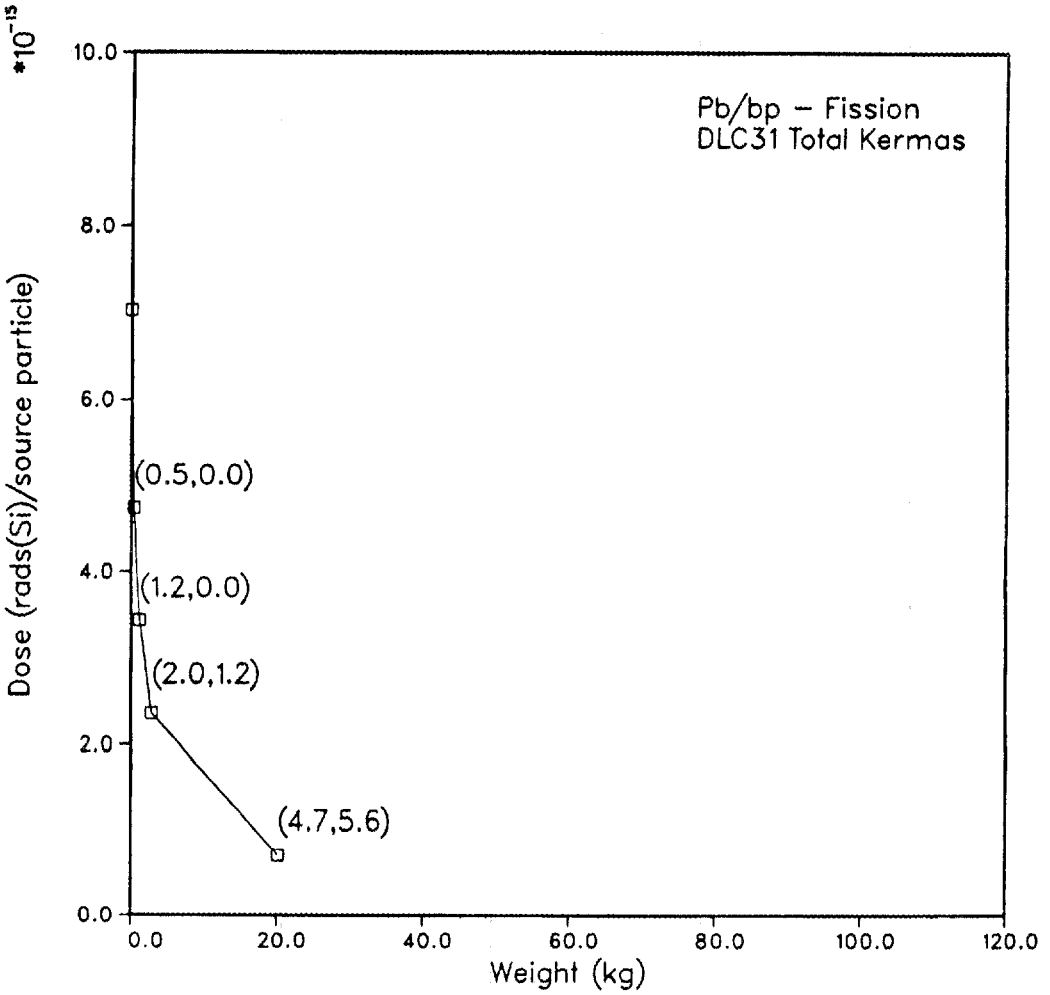

Figure 32. Dose vs. weight for a composite lead and borated polyethylene radiation shield and fission source. Numbers in parentheses represent shield thicknesses in cm for lead and borated polyethylene, respectively.

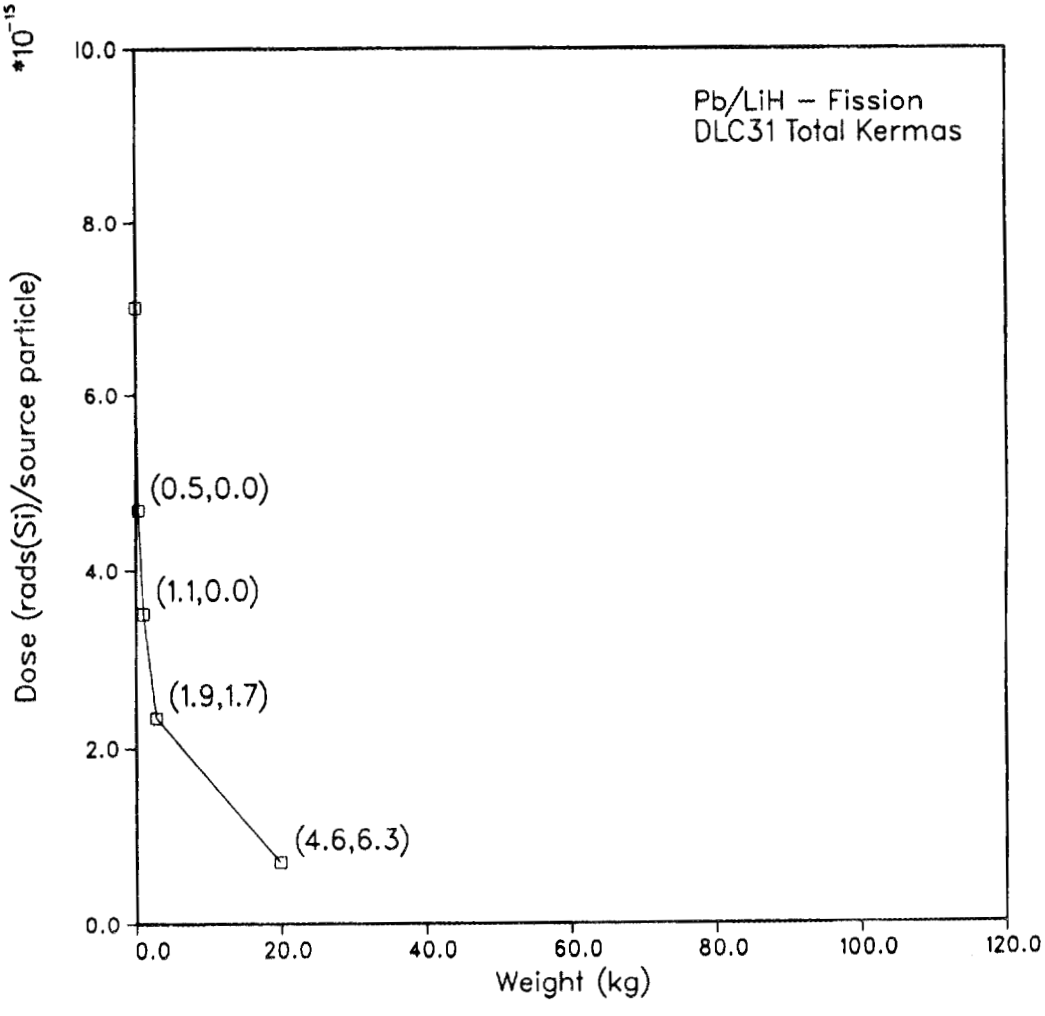

Figure 33. Dose vs. weight for a composite lead and lithium hydride radiation shield and fission source. Numbers in parentheses represent shield thicknesses in cm for lead and lithium hydride, respectively.

Table 37

Pb/LiH vs. Pb/borated polyethylene

Thermonuclear Source

Attenuation	Material	Thickness[a]	Dose[b]	Weight(kg)
33%	Pb/BP	1.02/7.07	2.53−14[c]	5.13
50%	Pb/BP	1.77/11.04	1.90−14	15.55
67%	Pb/BP	2.73/16.33	1.27−14	43.32
75%	Pb/BP	3.21/20.06	9.50−15	73.32
33%	Pb/LiH	0.00/6.97	2.53−14	2.39
50%	Pb/LiH	0.00/11.96	1.90−14	9.09
67%	Pb/LiH	0.19/17.95	1.27−14	27.49
75%	Pb/LiH	0.49/21.88	9.50−15	48.80

[a]cm of Pb/cm of borated polyethylene (B.P.) or LiH
[b]Rads(Si)/source particle, total neutron and gamma kerma factor from DLC31
[c]Read as 2.53×10^{-14}

Table 38

Pb/LiH vs. Pb/borated polyethylene

Fission Source

Attenuation	Material	Thickness[a]	Dose[b]	Weight(kg)
33%	Pb/BP	0.52/0.00	4.72−15[c]	0.38
50%	Pb/BP	1.18/0.00	3.43−15	1.15
67%	Pb/BP	1.96/1.21	2.36−15	2.89
90$	Pb/BP	4.67/5.61	7.08−16	20.22
33%	Pb/LiH	0.50/0.00	4.68−15	0.36
50%	Pb/LiH	1.08/0.00	3.52−15	1.01
67%	Pb/LiH	1.89/1.73	2.34−15	2.81
90%	Pb/LiH	4.64/6.32	7.01−16	19.85

[a]cm of Pb/cm of borated polyethylene (B.P.) or LiH
[b]Rads(Si)/source particle, total neutron and gamma kerma factor from DLC31
[c]Read as 4.72×10^{-15}

The superiority of the lithium hydride relative to the borated polyethylene as a neutron absorbing component of a radiation shield for space applications is readily apparent. At 50% attenuation with the thermonuclear source, the use of lithium hydride instead of borated polyethylene results in a weight savings of 36%. In contrast, for the fission source, neither material has a particular advantage for the attenuation levels investigated. This is due to the relative insignificance of the neutron dose from the fission source. At higher attenuation levels, however, the role of the neutron shield would increase in importance, and lithium hydride would be the material of preference.

3.3.3. Shield Optimization b.

Shield optimization studies were performed to investigate the importance of the ionization kerma relative to the total kerma for both fission and thermonuclear sources and both composite shields, Pb/LiH and Pb/borated polyethylene. As discussed in Section 2, the total kerma is the sum of the displacement kerma and the ionization kerma. Plots of dose versus shield weight are provided in Figures 34–37. The same conclusions drawn above can be made here, i.e., that lithium hydride is the superior material for shielding against neutrons. However, it is interesting to compare a plot of total kerma against one of ionization kerma. For example, looking at Figures 31 and 35 (both Pb/LiH and thermonuclear source), it is noted that the shield weights at every attenuation point are much greater for the ionization case. The ionization and total kerma results should be closer. The reason this difference occurs is the pertinent kerma factors in DLC31 are not from the same reference. Therefore, results from these kermas are not readily comparable (see Section 2).

3.3.4. Shield Optimization c.

Based upon the preceding information, other kerma factors were investigated. It was thought the gamma factors in DLC31 were accurate; the neutron data was probably outdated. Accordingly, neutron displacement kerma from Gabriel[2,17] and neutron displacement and ionization kerma factors from V. C. Rogers et al.[16] were employed. Plots of dose versus shield weight for the thermonuclear source were obtained for the neutron displacement only: Gabriel (Figure 38), Rogers (Figure 39), and DLC31 (revised units, Figure 40); neutron and gamma ionization (Figure 41); and total kerma with Rogers neutron data (Figure 42).

The displacement results are similar, although the revised DLC31 displacement kerma does not properly sum to the total DLC31 kerma when added to the ionization kerma. Its use is questionable. The coupled Rogers neutron ionization and DLC31 gamma ionization contrasts sharply with the pure DLC31 ionization data (Figure 41 versus Figure 35, respectively) again pointing to the differences in the neutron data. Comparing Figures 41 and 42, a strong dependence on ionization is noted for the total kerma. This is expected and it further justifies the use of Rogers and Gabriel neutron data in future work.

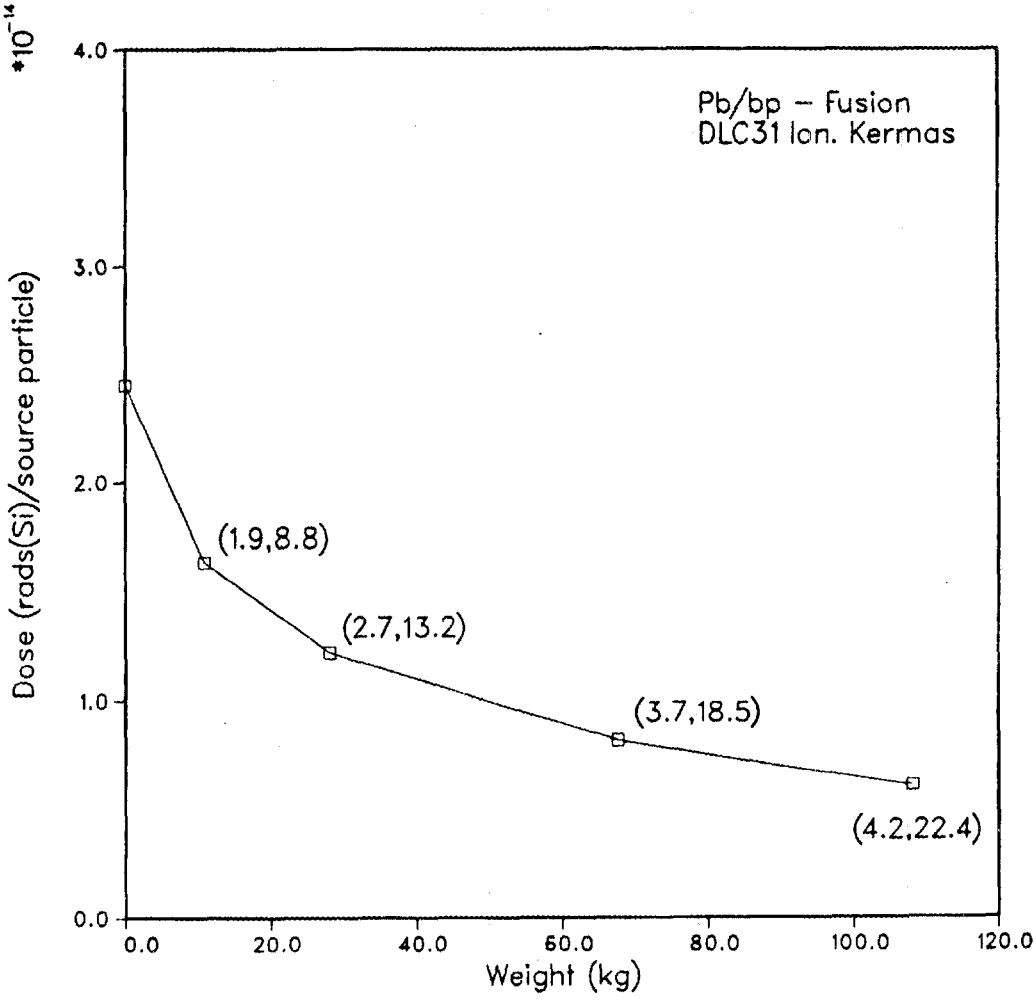

Figure 34. Dose vs. weight for a composite lead and borated polyethylene radiation shield using ionization kermas and thermonuclear source. Numbers in parentheses represent shield thicknesses in cm for lead and boated polyethylene, respectively.

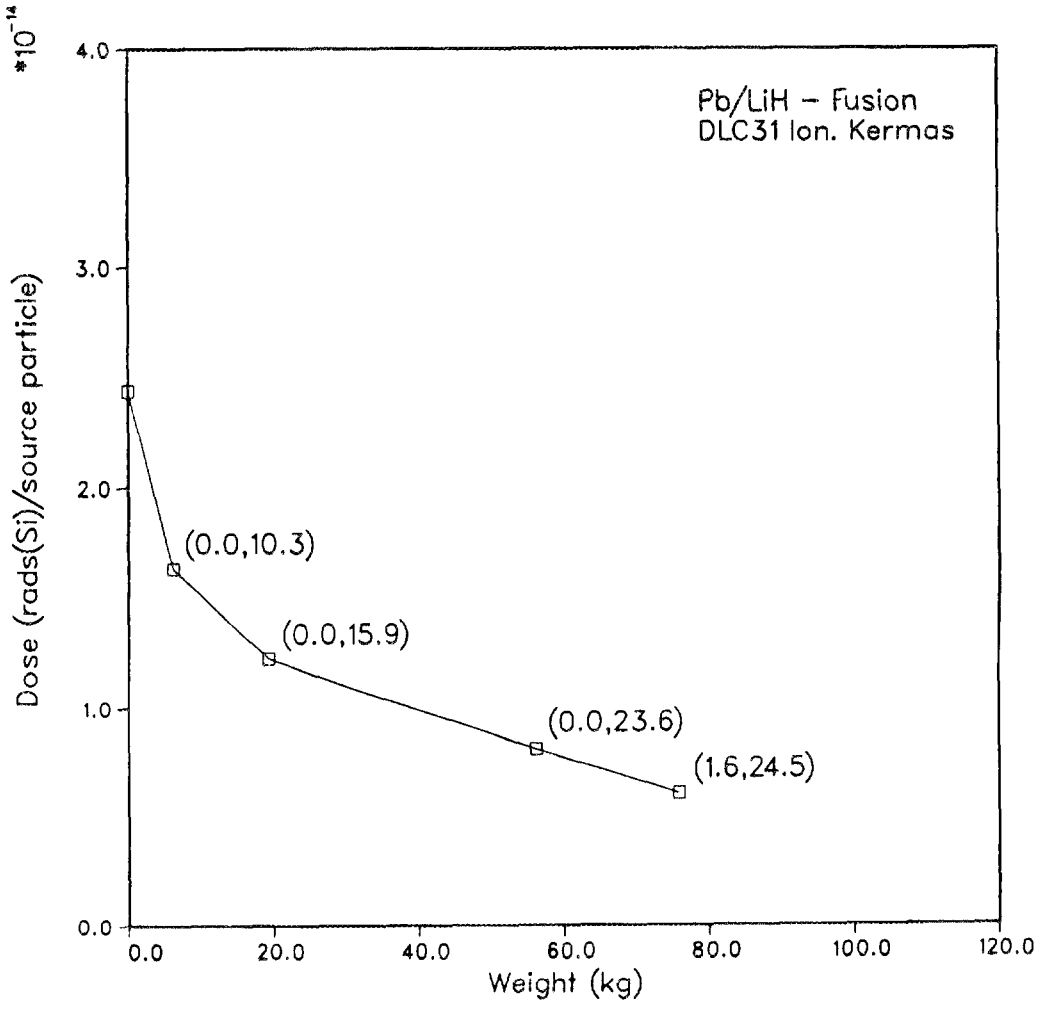

Figure 35. Dose vs. weight for a composite lead and lithium hydride radiation shield using ionization kermas and thermonuclear source. Numbers in parentheses represent shield thicknesses in cm for lead and lithium hydride, respectively.

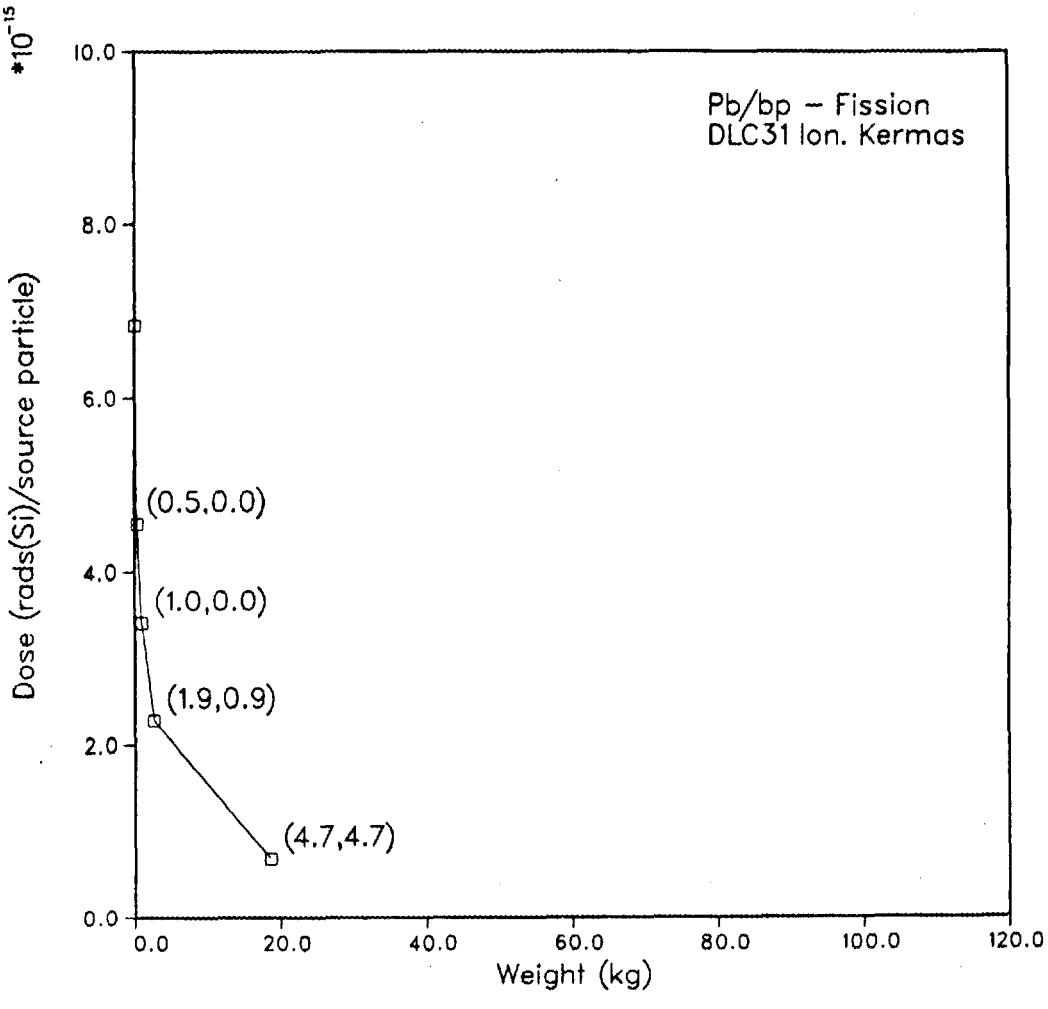

Figure 36. Dose vs. weight for a composite lead and borated polyethylene radiation shield using ionization kermas and fission source. Numbers in parentheses represent shield thicknesses in cm for lead and borated polyethylene, respectively.

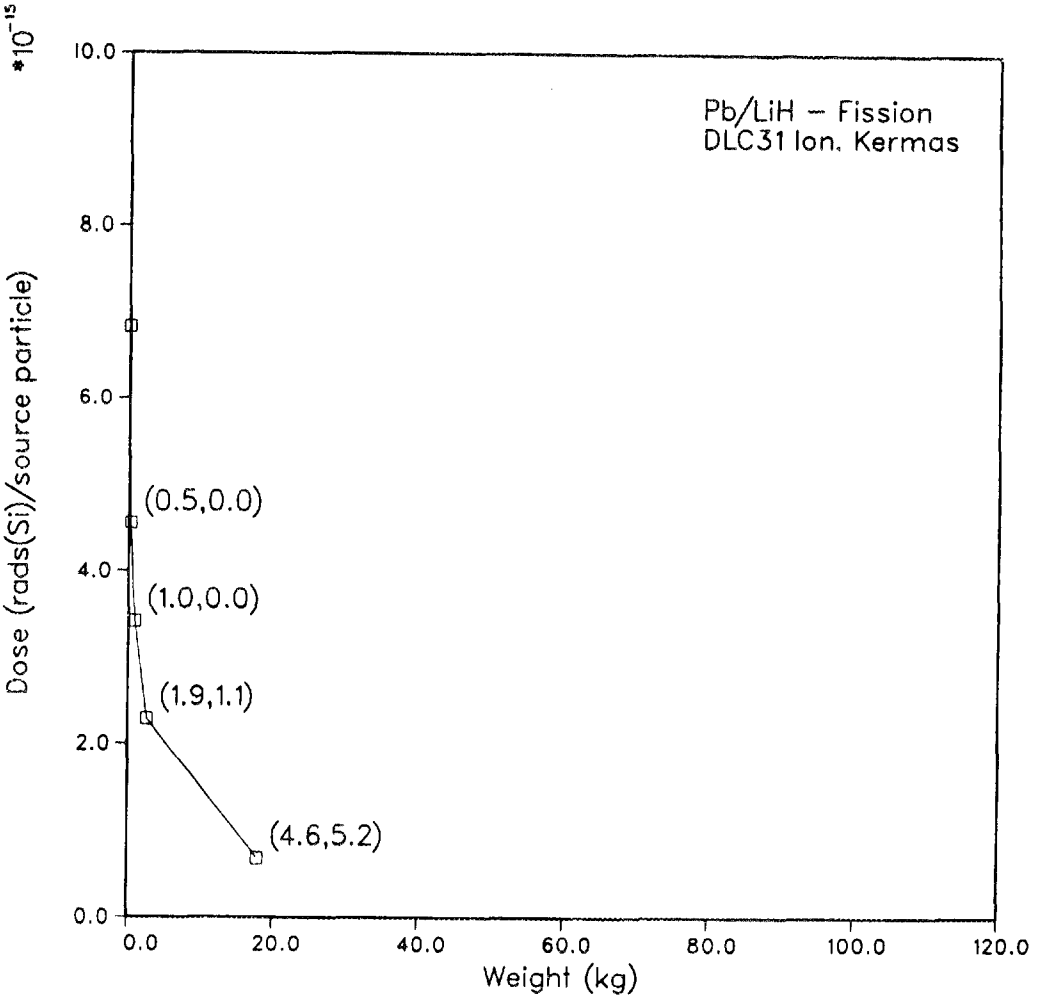

Figure 37. Dose vs. weight for a composite lead and lithium hydride radiation using ionization kermas and fission source. Numbers in parentheses represent shield thicknesses in cm for lead and lithium hydride, respectively.

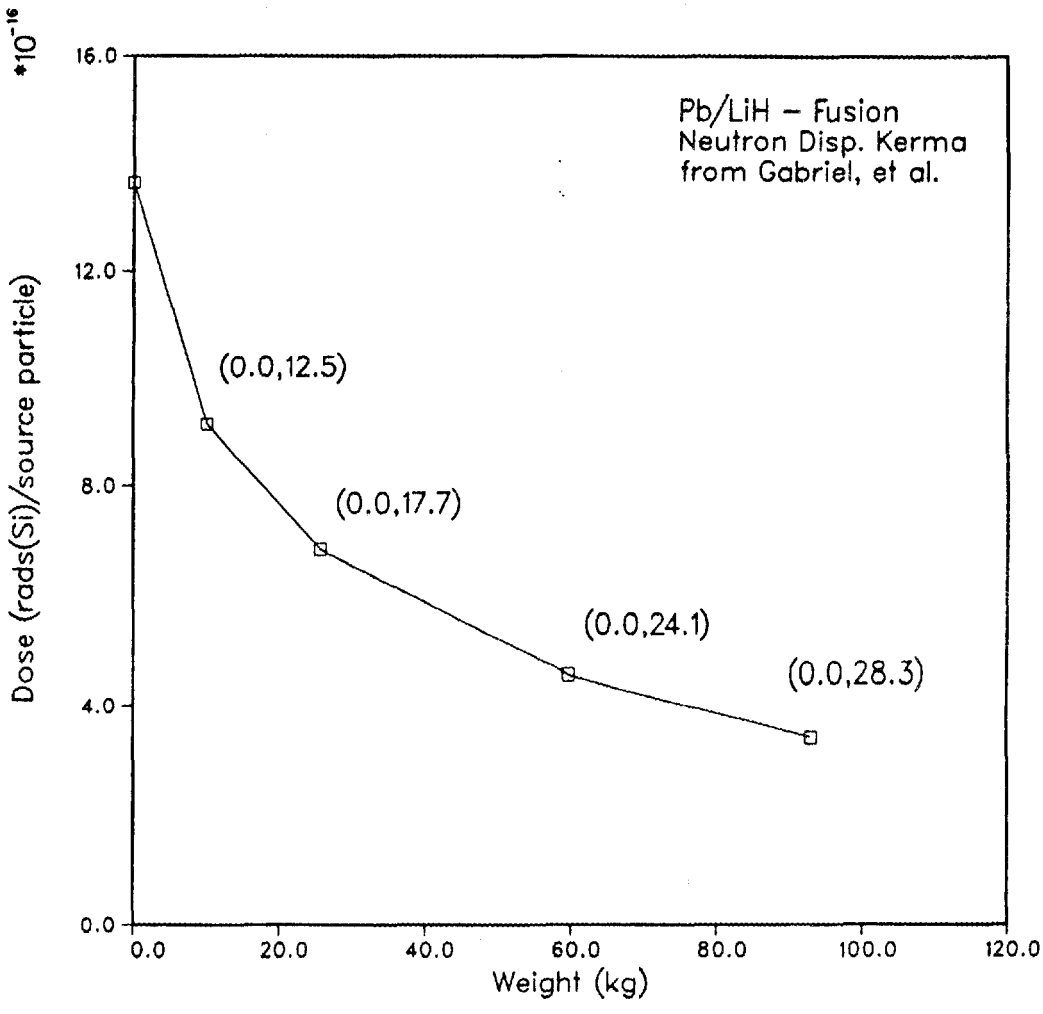

Figure 38. Dose vs. weight for a composite lead and lithium hydride radiation shield using the neutron displacement kerma from Gabriel and thermonuclear source. Numbers in parentheses represent shield thicknesses in cm for lead and lithium hydride, respectively.

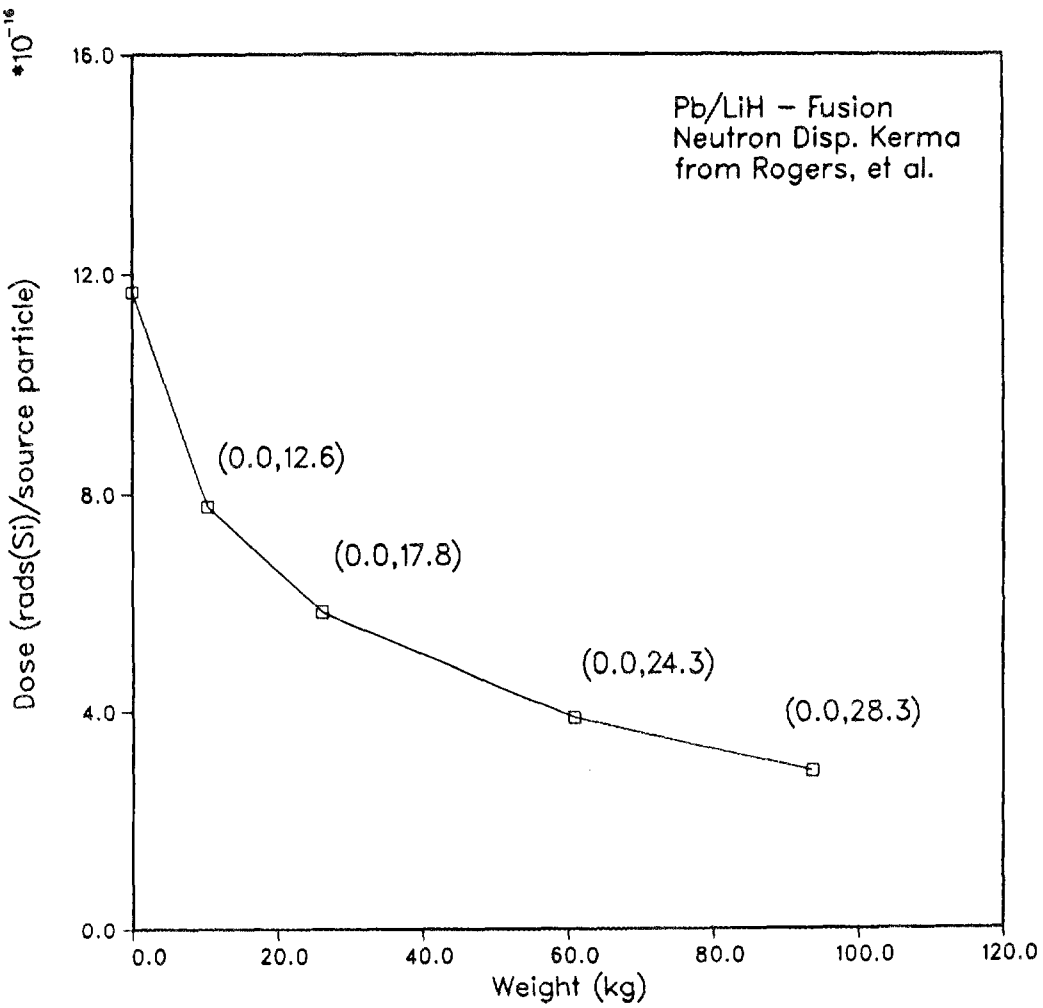

Figure 39. Dose vs. weight for a composite lead and lithium hydride radiation shield using a neutron displacement kerma from Rogers et al., and thermonuclear source. Numbers in parentheses represent shield thicknesses in cm for lead and lithium hydride, respectively.

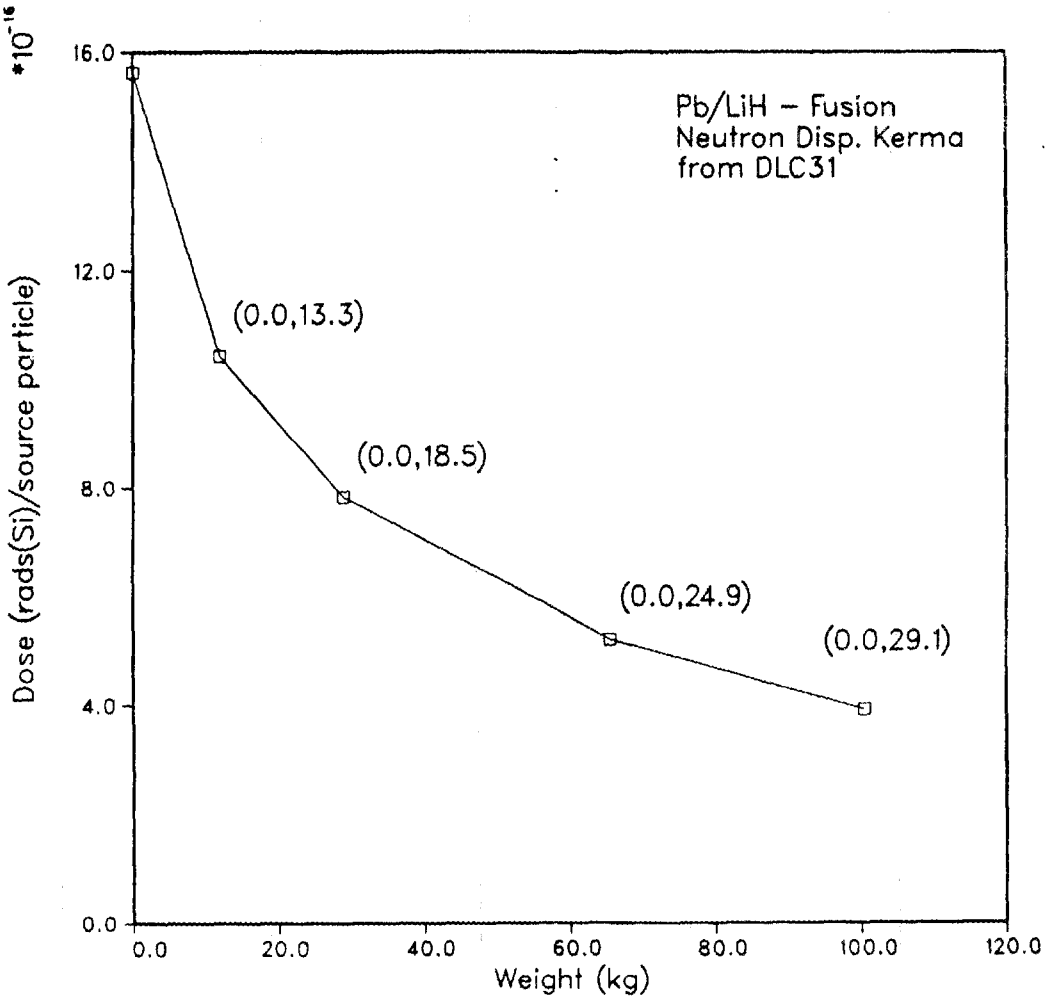

Figure 40. Dose vs. weight for a composite lead and lithium hydride radiation shield using a neutron displacement kerma from DLC31 and thermonuclear source. Numbers in parentheses represent shield thicknesses in cm for lead and lithium hydride, respectively.

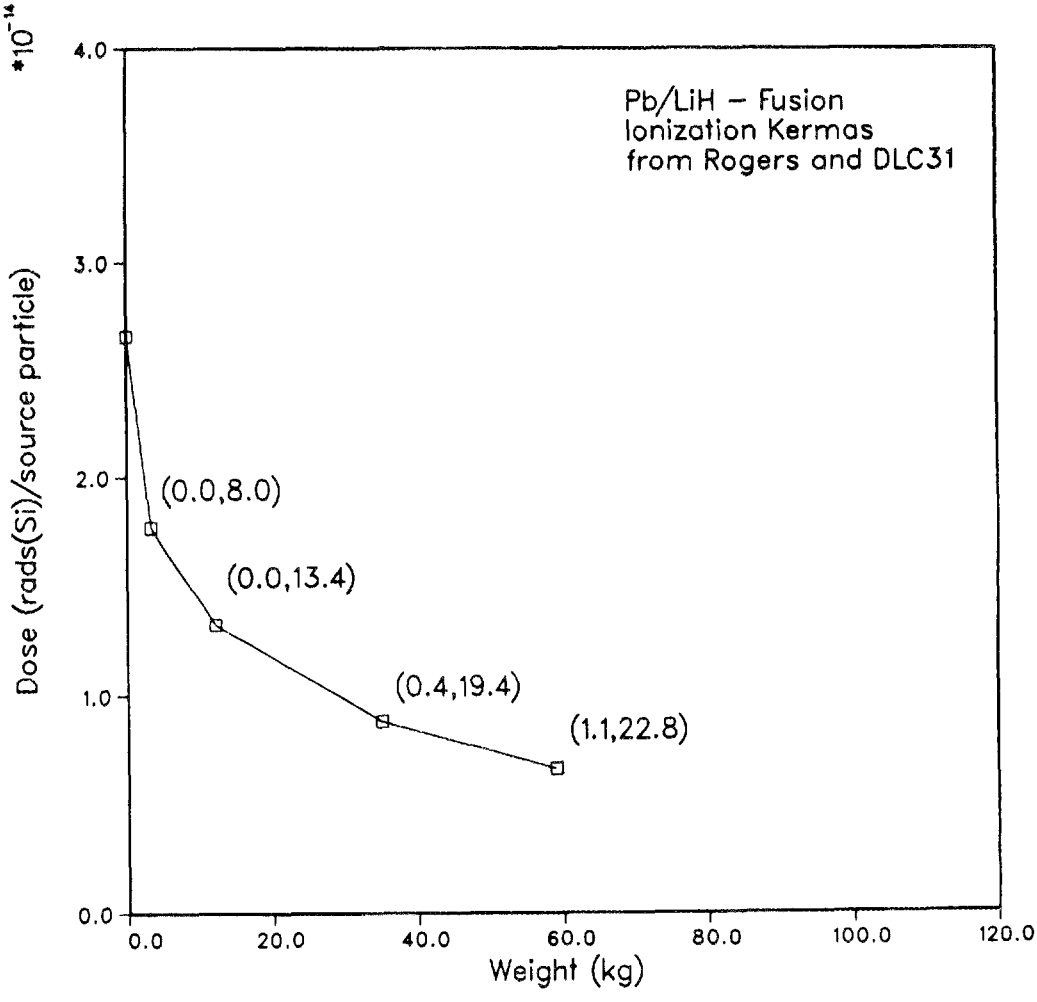

Figure 41. Dose vs. weight for a composite lead and lithium hydride radiation shield using Rogers and DLC31 ionization kermas and thermonuclear source. Numbers in parentheses represent shield thicknesses in cm for lead and lithium hydride, respectively.

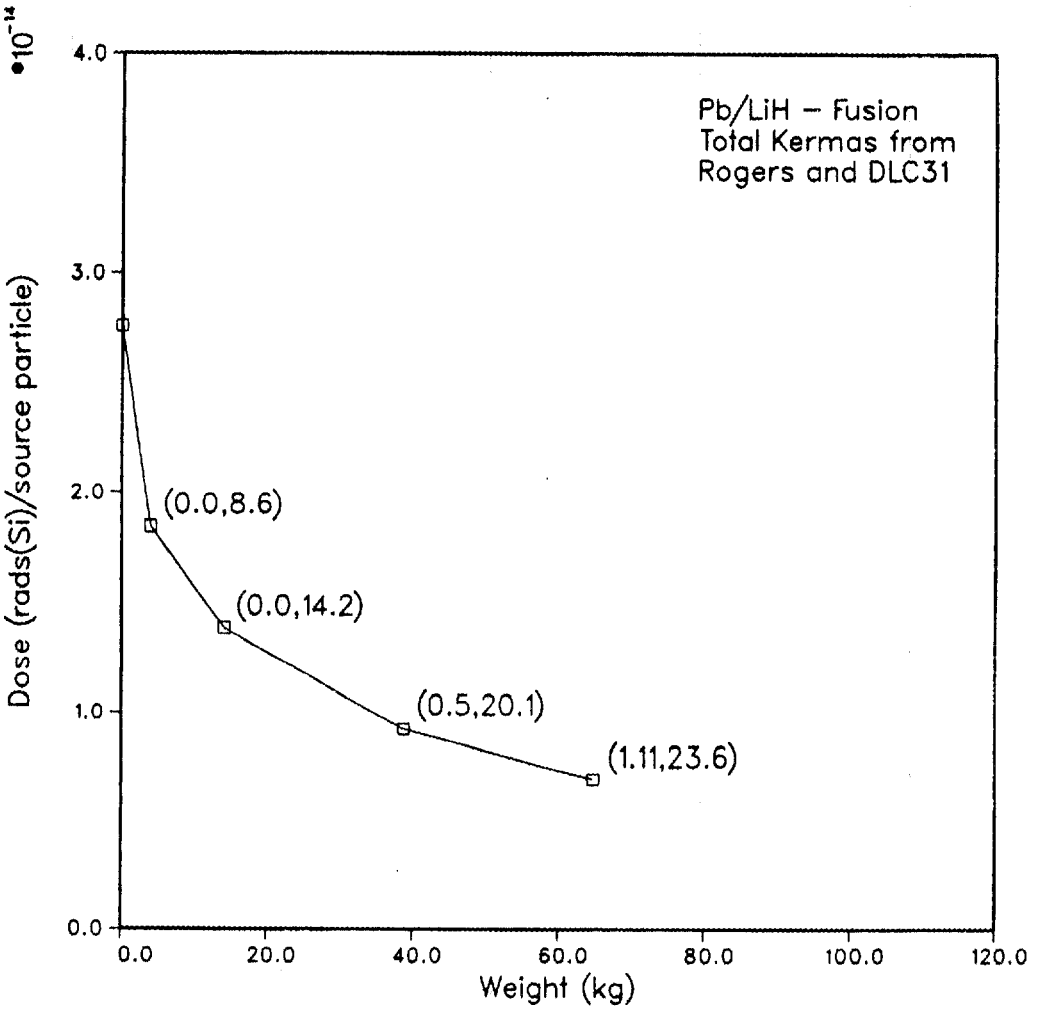

Figure 42. Dose vs. weight for a composite lead and lithium hydride radiation shield using the total neutron kerma from Rogers, total gamma kerma from DLC31, and thermonuclear source. Numbers in parentheses represent shield thicknesses in cm for lead and lithium hydride, respectively.

3.3.5. Shield Optimization d.

An updated cross section library[14] collapsed from Vitamin-E was incorporated into the shield optimization effort. This new library is essentially an ENDF/B-V update for the DLC31 cross section library. Flux-to-dose conversion factors (kermas) were carried over from the old library.

A comparative study was made to examine the differences between the old and new cross section data sets and utilizing total kermas from Rogers and DLC31. Four data sets were prepared, each specifying the thermonuclear source, Pb/LiH shield, and a target dose of 1.0×10^{-14} rads(S) per source particle. Results are presented in Table 39.

Table 39

Cross Section and Kerma Comparison Thermonuclear Source, Pb/LiH Shield

Kerma ID	X-Sec	Thickness[a]	Dose[b]	Weight(kg)
15/29[c]	DLC31	0.45/21.22	9.953−15[d]	44.66
44/49[e]	DLC31	0.34/18.85	1.003−14	32.06
15/29[c]	RWR[f]	0.79/22.09	1.003−14	52.18
44/49[e]	RWR	0.43/19.82	9.928−15	37.15

[a]cm of Pb/cm of LiH
[b]rads(Si)/source particle
[c]Total kerma from DLC31, neutron and gamma
[d]Read as 9.953×10^{-15}
[e]Employs Rogers Total Neutron kerma + DLC31 Gamma Kerma
[f]Updated cross section library, see references 14 and 15

There is a considerable variance in the shield configuration and weight depending on which kerma factor or cross section library is employed. On examination, it is seen that the use of Rogers neutron data reduces the shield weight, while the utilization of the new cross section data increases the weight. Coupling these two improvements results in a 17% decrease in shield weight as compared to the use of the pure DLC31 data.

3.3.6. Shield Optimization e.

To conclude this effort, dose attenuations of 33%, 50%, 67%, and 75% were calculated for a Pb/LiH shield and thermonuclear source, with the updated cross section library and neutron kerma factors from Rogers. Results are compiled in Table 40 and plotted in Figure 43. For this study, dose is tabulated in units of rads(Si)$\cdot$m^2/kT. The dose to the target can then be computed once the device

yield and distance is known. For example, a 100 kT device is detonated at distance of 1500 meters. Assuming a radiation shield with a 50% attenuation capability, the dose to the silicon target is $\approx$280 krads(Si).

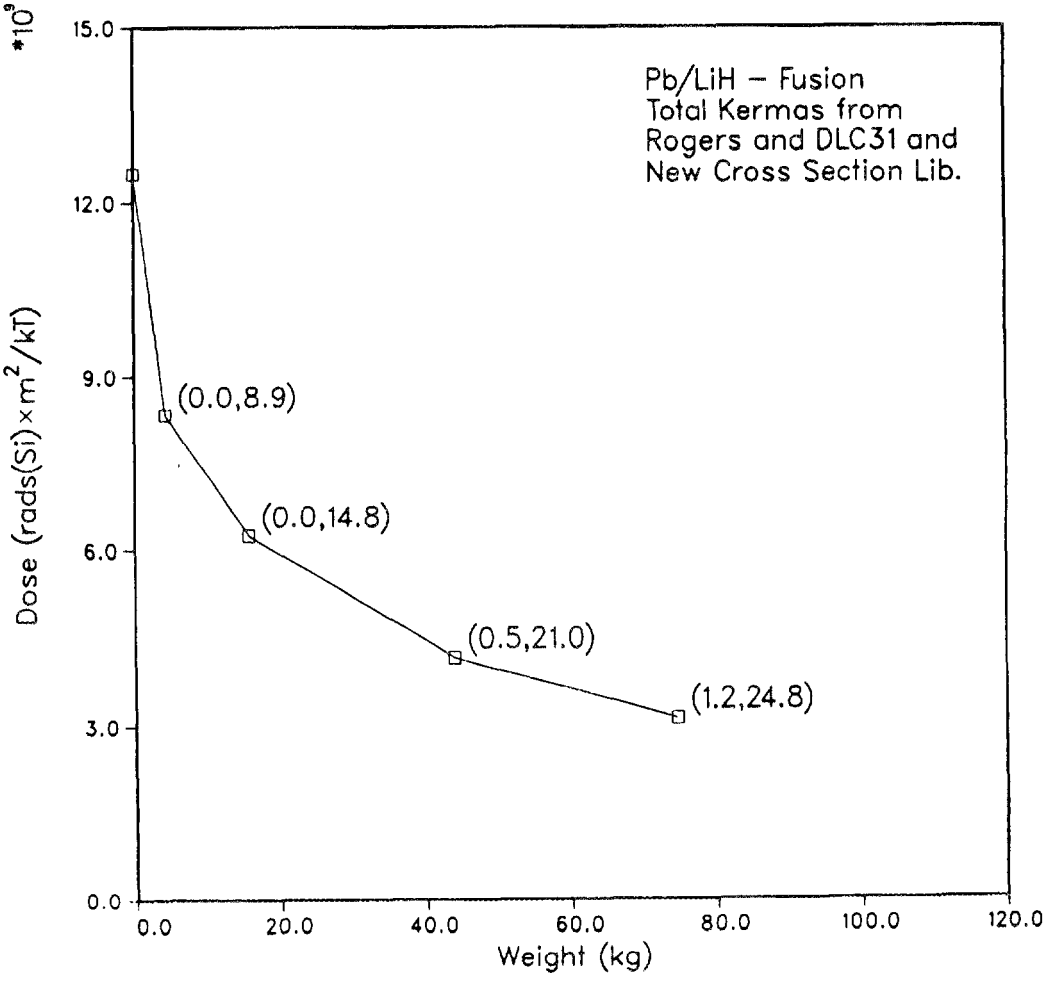

Figure 43. Dose vs. weight for a composite lead and lithium hydride radiation shield using the total neutron kerma from Rogers, total gamma kerma from DLC31, new cross section library, and thermonuclear source. Numbers in parentheses represent shield thicknesses in cm for lead and lithium hydride, respectively.

Table 40

Optimized Shield Weight and Composition as a Function of Dose for a Thermonuclear Source Utilizing New Cross Section Library

Attenuation	Material	Thickness[a]	Dose[b,c]	Weight(kg)
33%	Pb/LiH	0.00/8.88	8.327+9[d]	4.30
50%	Pb/LiH	0.00/14.76	6.244+9	15.74
67%	Pb/LiH	0.52/21.00	4.164+9	43.96
75%	Pb/LiH	1.15/24.85	3.123+9	74.55

[a] cm of Pb/cm of LiH

[b] rads(Si) $\cdot$ m^2/kT

[c] Updated cross section library, see text.
Employs Rogers Total Neutron Kerma + DLC31 Gamma Kerma

[d] Read as 8.327×10^9

4. SUMMARY

The calculations and results described in this report represent the efforts of an initial scoping study to assess the effects and magnitude of natural and man-made radiation modes on the performance of representative electronic components in an SDI satellite/weapon system surrounded by a thin shield. The shield is designed principally to provide protection of vital satellite components against low mass, high-velocity kinetic energy weapon projectiles.

The natural radiation environment of space does not pose a significant threat to the performance of the KEW shield or to the electronic components borne by the satellite provided they are located within the shield and generally away from the surface of the system. Table 41 summarizes the natural radiation yearly dose rates in the idealized representation of an electronic circuit/package, i.e., a silicon sphere having a radius of 2-cm (see Figure 1). The galactic and solar flare protons will not impact silicon based circuit performance even for long durations (10 years) in space. The accumulated dose from these radiation modes will be far below the threshold of damage for typical circuit components such as those described in Figures 8a and 8b.

Van Allen belt proton radiation gives rise to a substantially greater annual dose rate and is strongly dependent on both the altitude and orbital inclination at which the system is deployed. The Van Allen belt protons dose rate varies widely, but, in general, no appreciable damage will be sustained by those isolated by other on-board equipment. Single event upsets and circuit latch-ups may occur, but the magnitude and regularity are not expected to be overwhelming.

The large dose rate from Van Allen belt electron radiation is entirely a surface phenomena. That is, all of the energy of the radiation is deposited in the first few millimeters of the shield. The impact on shielded sensitive electronics is negligible, but damage may occur in other critical components such as antennae, mirrors, or sensors mounted on the satellite surface or through the outer shield. These components would also be severely damaged by the Van Allen belt protons since all of the energy attenuation would occur in the sensitive component rather than the shield.

Space detonated nuclear weapons and directed energy neutral particle beams represent the greatest threat to the satellite and the electronic equipment. The thin KEW shield does not have the capability to reduce the dose/dose rate from neutrons and gamma radiation for either a fission or fusion weapon to acceptable levels. Survivability of the satellite and electronic system depends on the distance at which the detonation occurs and the yield of the weapon (see Figure 20). The preponderate radiation from a nuclear weapon, however, is in the form of X-rays which impact on the surface of the shield in the form of an energetic hydrodynamic-like impulse

Table 41

Yearly Dose to the Silicon Due to
Natural Radiation Environments

Radiation Environment	Dose Rate (Rads/year)
Van Allen Belt Protons[a]	30 – 43,500
Galactic Protons[a]	0.5 – 1
Solar Flare Protons[a,b]	85 – 300
Van Allen Belt Electrons[c]	100 – 100,000

[a]KEW Shield and unattenuated primary protons only
[b]Assumes 5 flares per year
[c]Surface effect, dose in 0.035 cm of Si following 0.254 cm of Al shielding

and, depending on the black body temperature of the weapon, deliver large doses to on-board electronic equipment. Surface damage will generally predominate. The single event upset and latch-up rates in vital circuits from weapon radiation may cause mission failure for satellites that are near the limit of the keep-out distances suggested in Figure 20.

Directed energy weapon radiation will severely impact the performance and survivability of the satellite. However, it is not anticipated that weapons of this type will be of an immediate threat since this weapon development is still in the early stages.

An idealized satellite geometry was considered in this study and did not account in most of the calculations for the presence of additional shielding material present between the shield and the sensitive electronic component. Additional studies were completed to determine the effect of additional shielding surrounding the silicon sphere. One-dimensional radiation transport methods coupled to a shield optimization processor were used to establish the additional local minimum weight/damage reducing shielding requirements. These data obtained were used to establish local shielding material configurations and to provide some insight into the effects of these materials on the survivability of the satellite.

The results reported here are for one event weapon detonations and single neutral particle beam illumination. No consideration was given to multiple hits wherein the structural integrity of the shield is violated or the single event/latch-up rate is prohibitive.

Finally, it should be noted that all of the results reported here were obtained using available response functions for dose, damage, single-event upset, etc. Some of the damage responses data require re-evaluation and updating to reduce the uncertainties in the results which may be as large as a factor of two for the present data.

ACKNOWLEDGEMENTS

The authors wish to thank Mrs. Dawn C. Human for her significant efforts in typing this manuscript and for her assistance throughout this program.

REFERENCES

1. L. W. Ricketts, "Fundamentals of Nuclear Hardening of Electronic Equipment," Wiley-Nterscience, New York, NY, 1972.

2. T. A. Gabriel and B. L. Bishop, "Radiation Damage in Silicon Due to Albedo Neutrons Emitted From Hadronic Beam Dumps (Fe and U)," published in the *Proceedings of the Topical Meeting on Theory and Practices in Radiation Protection and Shielding*, Knoxville, Tennessee, April 1987.

3. T. A. Gabriel and W. Schmidt, *Nucl. Instrum. Methods* **134**, 271 (1976).

4. T. A. Gabriel, *Nucl. Instrum. Methods* **150**, 146 (1978).

5. T. A. Gabriel, "The High Energy Transport Code HETC," ORNL/TM-9727, Oak Ridge National Laboratory, (September, 1985).

6. H. W. Bertini, *Phys. Rev.* **188**, 1711 (1969).

7. R. L. Ford and W. R. Nelson, "The EGS Code System Computer Programs for the Monte Carlo Simulation of Electromagnetic Cascade Shower (Version 3)," SLAC-0210, Stanford Linear Accelerator Center, (1978).

8. T. A. Gabriel, "The Methods and Applications of Monte Carlo in Low Energy ($\leq$ 20 MeV) Neutron-Photon Transport (MORSE). Part I: Methods," in *Computer Techniques in Radiation Transport and Dosimetry*, Walter R. Nelson and Theodore M. Jenkins, eds., Plenum Press, New York, 1979.

9. N. M. Greene et al., "AMPX: A Modular Code System for Generating Coupled Multigroup Neutron-Gamma Libraries From ENDF/B," ORNL/TM-3706, Oak Ridge National Laboratory, (1973).

10. J. O. Johnson and T. A. Gabriel, "Development and Evaluation of a Monte Carlo Code System for Analysis of Ionization Chamber Responses," ORNL/TM-10196, Oak Ridge National Laboratory (July 1987).

11. W. W. Engle, Jr., "A Users Manual for ANISN," K-1693, Oak Ridge National Laboratory (March 1967).

12. W. W. Engle, Jr., "A Users Manual for ASOP-ANISN Shield Optimization Program," CTC-INF-941, Oak Ridge National Laboratory (September 1969).

13. D. E. Bartine et al., "Production and Testing of the DNA Few-Group Coupled Neutron—Gamma Cross-Section Library," ORNL/TM-4840, Oak Ridge National Laboratory, (March 1977). (This library is often referred to as DLC31.)

14. R. W. Roussin, Private communication, "DNA Broad-Group ANISN Libraries Based on VITAMIN-E," August 28, 1985.

15. "VITAMIN-E, A Coupled 174-Neutron, 38-Gamma-Ray Multigroup Cross-Section Library for Deriving Application-Dependent Working Libraries for Radiation Transport Calculations," DLC-113, Radiation Shielding Information Center, Oak Ridge National Laboratory (1985).

16. V. C. Rogers et al., "Silicon Ionization and Displacement Kerma for Neutrons From Thermal to 20 MeV," *IEEE Transactions on Nuclear Science*, Vol. NS-22, No. 6, December 1975.

17. T. A. Gabriel et al., "Radiation Damage Calculations: Primary Knock-On Atom Spectra Displacement Rates, and Gas Production Rates," NS+E **61**, 21-32 (1976); also, T. A. Gabriel and B. L. Bishop, "Radiation Damage in Silicon Due to Albedo Neutrons Emitted From Hadronic Beam Dumps (Fe and U)," *Proceedings From the Topical Meeting on Theory and Practices in Radiation Protection and Shielding*, Knoxville, Tennessee (April 1987).

18. F. B. McLean, "Interactions of Hazardous Environments With Electronic Devices," Tutorial Short Course, IEEE 1987 Nuclear and Space Radiation Effects Conference, Snowmass, Colorado (July 27, 1987).

19. J. Lindhard et al., *Mat. Fys. Medd. Selsk* **33** (1963), 1.

20. O. S. Oen, "Cross Sections for Atomic Displacements in Solids by Fast Electrons," ORNL-4897, Oak Ridge National Laboratory (1970).

21. J. H. Cahn, "Irradiation Damage in Germanium and Silicon Due to Electrons and Gamma Rays," *J. Appl. Phys.* **30**, 1310 (1959).

22. J. E. Gover and J. R. Srour, "Basic Radiation Effects in Nuclear Power Electronics Technology," SAND85-0776.

23. W. A. Rhoades, "Development of a Code System for Determining Radiation Protection of Armored Vehicles (The VCS Code)," ORNL/TM-4664 (October 1974).

24. Andre Gsponer and Sumer Sahin, "Protection Factors of Modern Armored Tanks Against Enhanced-Radiation and Fission Nuclear Weapons," ISRI-83-05 (February 1984, preliminary).

25. P. J. Dolan et al., "Characteristics of the Nuclear Radiation Environment Produced by Several Types of Disasters," SRI Project ESU-1915 (May 1982).

26. T. A. Gabriel, unpublished data.

27. MAJ R. Leong, 1LT D. Lahti, 1LT K. Murphy, 1LT S. Rieco, 1LTR. Zacharko, "AFWL Exoatmospheric Nuclear Radiation Environment Prediction and Shielding Codes Applicable to the Strategic Defense Initiative (SDI)," Draft Report, Air Force Weapons Laboratory, Kirtland Air Force Base, New Mexico, May 1986.

28. R. Siegel and John R. Howell, *Thermal Radiation Heat Transfer*, McGraw-Hill, Inc., 1972.

29. C. E. McIlwain, "Coordinates for Mapping the Distribution of Magnetically Trapped Particles," *J. Geophys. Res.* **66**, 3681 (1961).

30. "Data Users' Note: TRECO, An Orbital Integration Computer Program for Trapped Radiation," National Space Science Data Center, Goddard Space Flight Center, NASA Document NSSDC-68-02, 1968.

31. J. L. Modisette et al., "Model Solar Proton Environments for Manned Space Design," Technical Note, NASA-TN-D-2746, 1965.

32. F. B. McDonald, "IQSY Observations of Low-Energy Galactic and Solar Cosmic Rays," in *Annals of the IQSY* **4**, A. C. Strickland, ed., M.I.T. Press, Cambridge (1969), 187.

33. N. Durgaprasad, C. E. Fichtel, and D. E. Guss, "Solar Modulation of Cosmic Rays and Its Relationship to Proton and Helium Fluxes, Interstellar Travel, and Interstellar Secondary Production," *J. Geophys. Res.* **72**, 2765 (1967).

34. W. N. Hess, *The Radiation Belt and Magnetosphere*, Blaisdell Publishing Co., Waltham, Massachusetts, Toronto, London, 1968.

35. F. B. McDonald, "Direct Determination of Primary Cosmic Ray Alpha Particle Energy Spectrum by New Method," *Phys. Rev.* **104**, 1723 (1956).

36. P. S. Frier, E. P. Ney, and C. J. Waddington, "Flux and Energy Spectrum of Cosmic-Ray α Particles During Solar Maximum," *Phys. Rev.* **114**, 365 (1959).

37. C. Y. Fan, G. Glockler, and J. A. Simpson, "Cosmic Radiation Helium Spectrum Below 90 MeV Per Nucleon Measured on Imp I Satellite," *J. Geophys. Res.* **20**, 3515 (1965).

38. R. G. Alsmiller, Jr., R. T. Santoro, J. Barish, and H. C. Claiborne, "Shielding of Manned Space Vehicles Against Protons and Alpha Particles," Oak Ridge National Laboratory Report ORNL-RSIC-35 (1972). [The authors wish to thank R. G. Alsmiller, Jr., for allowing us to draw freely from their work.]

39. F. W. Walker, D. G. Miller, and F. Feiner, "Chart of the Nuclides," 13 ed., Knolls Atomic Power Laboratory, July 1983.

INTERNAL DISTRIBUTION

1. R. G. Alsmiller, Jr.
2. B. R. Appleton
3. D. E. Bartine
4. J. M. Barnes
5. B. L. Bishop
6. E. D. Brewer
7. T. J. Burns
8. D. G. Cacuci
9. J. D. Drischler
10–19. T. A. Gabriel
20. C. M. Haaland
21. E. B. Harris
22. W. R. Hendrich
23. R. L. Huddleston
24. D. T. Ingersoll
25. J. K. Ingersoll
26. J. O. Johnson
27. H. E. Knee
28. R. A. Lillie
29. F. C. Maienschein
30. R. W. Peelle
31. A. S. Quist
32. R. W. Roussin
33–42. R. T. Santoro
43. J. E. Smith
44. M. S. Smith
45. D. G. Thomas
46. H. E. Trammell
47. R. C. Ward
48. C. R. Weisbin
49. A. Zucker
50. J. J. Dorning (Consultant)
51. G. H. Golub (Consultant)
52. R. M. Haralick (Consultant)
53. D. Steiner (Consultant)
54. EPMD Reports Office
55–56. Laboratory Records Department
57. Laboratory Records, ORNL-RC
58. Document Reference Section
59. Central Research Library
60. ORNL Patent Office

EXTERNAL DISTRIBUTION

61. Dr. Charles Aeby, AFWL/NTC, Air Force Weapons Laboratory, Kirtland Air Force Base, New Mexico 87117-6008
62. Dr. M. Alme, Computer Sciences Corporation, 2100 Air Park Road SE, Albuquerque, New Mexico 87106
63. Lt Dale Atkinson, AFWL/NTCOA, Air Force Weapons Laboratory, Kirtland Air Force Base, New Mexico 87117-6008
64. Mr. L. Bariess, Martin Marietta Denver Aerospace, P.O. Box 179, Denver, Colorado 80201
65. Mr. B. Belason, AVCO Specialty Materials, 2 Industrial Way, Lowell, Massachusetts 01851
66. Dr. C. Bersch, Institute for Defense Analysis, 1801 N. Beauregard Street, Alexandria, Virginia 22311
67. Dr. B. Cour-Palais, NASA Johnson Space Center, Houston, Texas 77058
68. Lt Richard Engstrom, AFWL/NTCOA, Air Force Weapons Laboratory, Kirtland Air Force Base, Albuquerque, New Mexico 87117

69. Dr. F. Felber, JAYCOR, P.O. Box 85154, San Diego, California 92138
70. Mr. Alan Holt, National Aeronautics and Space Administration, NASA/SSU, Washington, D.C. 20546
71. Dr. W. Isbell, General Research Corporation, P.O. Box 30400, Santa Barbara, California 93105
72. Lt Col M. Kemp, SDIO/T/SL, Pentagon, Washington, D.C. 20301-7100
73. Lt Col C. Lee, SD/CNIV, P.O. Box 92960, Los Angeles Air Force Base, Los Angeles, California 90009-2960
74. Dr. J. E. Lowder, SPARTA, Inc., 21 Worthen Road, Lexington, Massachusetts 02173
75. Dr. W. G. Nichols, Computer Sciences Corporation, 2100 Air Park Road SE, Albuquerque, New Mexico 87106
76. Dr. J. J. O'Sullivan, ANSER Corporation, 1215 Jefferson Davis Hwy, Suite 800, Arlington, Virginia 22202
77. Glenn Ormbrek, AFWAL/MLPJ, Air Force Wright Aeronautical Laboratory, Wright-Patterson Air Force Base, Ohio, 45433-6533
78. Dr. D. Schmidt, Carbon Fiber Composites, 1092 Lipton Lane, Dayton, Ohio 45430
79. Dr. P. Seckler, SD/CNWK, P.O. Box 92960, Los Angeles Air Force Base, Los Angeles, California 90009-2960
80. Dr. S. Stone, Mission Research Corporation, 3505 Cadillac Avenue, Building H, Costa Mesa, California 92626
81. Dr. P. Trester, GA Technologies, P.O. Box 85608, San Diego, California 92138
82. Office of Assistant Manager for Energy Research and Development, Department of Energy, Oak Ridge Operations Office, P.O. Box E, Oak Ridge, Tennessee 37831

83–92. Office of Scientific and Technical Information, P.O. Box 62, Oak Ridge, Tennessee 37830